STUDY OF THE SURFACE REACTIVITY OF Ni-RICH POSITIVE ELECTRODE
MATERIALS FOR Li-ION CELLS

by

Ines Hamam

Submitted in partial fulfilment of the requirements for

the degree of Master of Science

at

Dalhousie University

Halifax, Nova Scotia

August 2020

إِلَى جَدَّتَايَ اللَّتَيْنِ تُشجِّعُنِي الفَرْحَةُ الَتِي تَغْمُرُ قَلْبَيْهِمَا كُلَّمَا رَأَتَا تَقَدُّمِي فِي الدِّرَاسَةِ

TABLE OF CONTENTS

LIST OF TABLES

LIST OF FIGURES

ABSTRACT

The growth of surface impurities on positive electrode materials used in Li-ion cells is detrimental to the electrode manufacturing process and the electrochemical performance of the cells. Ni-rich layered lithium metal oxides are promising materials for the production of high capacity Li-ion batteries but suffer from poor air stability and high sensitivity to surface impurity growth. For this reason, it is common in industry to wash these materials before introducing them in Li-ion cells. However, very little mechanistic understanding of the reaction between the materials and the aqueous solution used for washing is known. In this work, the effects of exposing Ni-rich positive electrode materials to aqueous solutions were studied. By combining results from the analysis of both the washing solutions and the materials after washing, two pH-dependent mechanisms were proposed. These reactions were then validated by inductively coupled plasma optical emission spectrometry (ICP-OES) analysis, thermogravimetric analysis coupled with mass spectrometry (TGA-MS), and X-ray powder diffraction (XRD) analysis. Additionally, core-shell materials containing a gradient-concentration of Ni were tested for the possibility to increase the air stability of Ni-rich positive electrode materials with minimal compromise to electrochemical properties. By improving both the washing process for Ni-rich materials and increasing the air stability of these materials, Ni-rich positive electrodes could reach high performance levels which are currently, commercially unattained.

LIST OF ABBREVIATIONS AND SYMBOL

BET	Brunauer-Emmett-Teller
CCD	Charged couple device
CS	Core-shell
CSTR	Continuous stirred-tank reactor
DRC	Democratic Republic of Congo
e	Elementary charge
EDS	Energy-dispersive X-ray Spectroscopy
EIS	Electrochemical impedance spectroscopy
EV	Electric vehicle
ICP	Inductively coupled plasma
IPCC	Intergovernmental Panel on Climate Change
LDL	Lower detection limit
LFP	$LiFePO_4$
LMO	$LiMn_2O_4$
LNO	$LiNiO_2$
LTMO	Lithium transition metal oxide
MS	Mass spectrometry
NCA	$LiNi_{1-x-y}Co_xAl_yO_2$
NMC	$LiNi_{1-x-y}Mn_xCo_yO_2$
OES	Optical emission spectrometry
PC	Polycrystal

pH	Power of hydrogen
pOH	Power of hydroxide
R_{cell}	Cell's internal resistance
RH	Relative humidity
RSD	Regular standard deviation
SC	Single crystal
SEI	Solid electrolyte interphase
SEM	Scanning Electron Microscopy
TGA	Thermogravimetric analysis
TM	Transition metals
UN	United Nations
μ	Electrochemical potentials
V_{OC}	Open-circuit voltage
WMO	World Meteorological Organization
XRD	X-ray diffraction

ACKNOWLEDGMENTS

CHAPTER 1. Introduction

1.1. Motivation and general objectives

In his statement published in the World Meteorological Organization (WMO) report on the state of global climate in 2019, the United Nations (UN) Secretary-General António Guterres says,[1]

> "Climate change is the defining challenge of our time. Time is fast running out for us to avert the worst impacts of climate disruption and protect our societies from the inevitable impacts to come."

In this same report, the WMO data confirms that the global mean temperature has increased by 1.1 ± 0.1 °C compared to pre-industrial temperature levels.[1] Temperatures recorded in 2019 mark a record high in global temperature exceeding the previous record set only in 2016. The year 2019 was marked with intense climatic phenomena such as heatwaves and long periods of droughts leading to above-average fires across the world. Notably, in Australia where wildfires have destroyed millions of hectares, but also in California, Siberia and regions of the Arctic where fires had previously been almost unheard of.[1] The Paris Agreement targets a limitation of the global temperature rise to 1.5 °C, however the Intergovernmental Panel on Climate Change (IPCC) reports inevitable consequences even from a 1.5 °C increase in temperature levels.[2]

To reach the target set by the Paris Agreement, the UN urges the reduction of greenhouse gas emission by 45% from our 2010 levels by 2030; the objective is to reach a zero-net emission by 2050.[1] Meanwhile, the global energy demand continues to increase and energy

efficiency is increasingly becoming a necessity in order to meet the future demand of an ever-growing world population. Part of the solution that would allow a global decrease of greenhouse gases while satisfying the increasing demand for energy, is the transition towards renewable energy sources and the efficient electrification of transport—both changes that call for the development of high performance electrical energy storage technologies.[3, 4] The decarbonization of transport and electrical power generation is an effective short-term and long-term solution to limit the 1.5 °C temperature overshoot.[4] The auto industry has recently expressed its commitment to the electrification of transport with Toyota planning to release more than ten electric vehicle (EV) models between 2020-2025, Volkswagen plans to release 80 EV models by 2025, and Mercedes targets 50 EV models by 2025.[4] Other manufacturers such as Volvo and Tesla are also developing electric trucks and semi-trucks.[4] Furthermore, the Beijing Automotive Industry Company aims to reduce the sale of combustion engine vehicles to zero by 2025.[4]

Li-ion batteries are today the most appealing energy storage technology for automotive applications due to their high power and high energy density.[5–7] Li is the element with the lowest reduction potential (-3.04 V) which enables high voltage Li-ion cells.[8] Additionally, Li is the lightest metal, the third lightest element, and Li^+ cation has one of the smallest ionic radii.[8] This allows for Li-ion cells to have high gravimetric and volumetric energy density. Advances in electrode material and electrolyte research have enabled high performance and high-mileage all electric cars. The 100 kWh Li-ion battery packs found in the Tesla Model S and Model X vehicles offer a driving range of 508 km per charge[9] and are expected to last 240,000 km.[10] Recent Li-ion cell testing results published by

Harlow *et al.* have shown that modern Li-ion cells can power an electric car for 1.6 million km thus setting the benchmark for battery technology.[11]

Despite the high performance and long service life of present Li-ion batteries, further research and development is needed to lower the barrier to adoption of EVs. These barriers can be lowered by increasing energy density, increasing power density, increasing safety and reducing cost. Many promising Li-ion cell chemistries exist but many challenges such as limited electrolyte conductivity, parasitic reactions at the electrode-electrolyte interfaces and dissolution and degradation of the electrode materials remain to be overcome.[7]

The research work presented in this thesis aims to contribute to the academic effort to understand and decouple the complex mechanisms at work in Li-ion cells. Advancement in this field of research would enable the commercialization of higher performance Li-ion batteries—a technology whose role will be crucial to fulfill the ever-growing energy demand while reducing the emission of greenhouse gases and while decelerating climate change.

1.1. Specific objectives and scope of thesis

This thesis focuses on the study of positive electrode materials for Li-ion cells, particularly, positive electrode materials rich in Ni. As will be further discussed in Section 2.2, the adoption of Ni rich materials provides many advantages in terms of specific capacity and cost. However, these materials suffer from poor surface stability and have a propensity for

degradation and surface impurity growth when exposed to ambient atmosphere. When introduced in the Li-ion cell, these contaminations on the positive electrode have considerable detrimental effects on the functioning of the cell. To resolve this contamination problem, both manufacturers of electrode materials and manufacturers of Li-ion cells wash their Ni-rich materials after storage. The washing of Ni-rich positive electrode materials rids them of surface impurities but is also likely to further degrade them. As little is understood about the surface reactions of Ni-rich positive electrode materials when washed, this work aims to study the fundamental mechanisms responsible for consequent changes in these materials. This understanding can serve to design better coatings for Ni-rich positive electrodes as well and specify better storage and handling procedures in industry.

In this thesis, two different groups of Ni-rich materials are studied in different controlled conditions to study impurity growth and the effect of washing. The first group of materials consists of Ni-rich materials with compositionally uniform particles, and the second group consists of core-shell materials where the core region of the particle and the shell region of the particle differ in chemical composition.

1.2. Description of remaining chapters

The remaining chapters in this thesis describe the work that was done to achieve the specific objectives mentioned above. Chapter 2 provides necessary background information about the Li-ion cell system and its components. It summarizes the work previously done and

published pertaining to Li-ion battery research focusing on the research aspects most relevant to this work. Chapter 3 details the experimental methodology and the material characterization methods used in this work including the synthesis of the materials, testing protocols and testing conditions. Chapter 4 presents the results obtained from the first group of materials (Ni-rich materials with compositionally uniform particles) tested under different conditions. It is concluded with a summary of the findings of this first set of experiments. Chapter 5 presents the results obtained from the second group of materials tested (core-shell materials). These results aim to compare the resilience to surface degradation of these materials to the first group of materials tested in Chapter 4. Finally, Chapter 6 summarizes the overall findings of this work and suggests future research opportunities to further understand and mitigate the degradation of Ni-rich positive electrodes in Li-ion cells.

CHAPTER 2. Li-ion Batteries

Unlike primary cells (used in common alkaline batteries), which cannot be recharged after use as the chemical reaction which occurs in them is not easily reversible, Li-ion cells are a type of secondary cell which can efficiently undergo many charge-discharge cycles. During charge, a Li-ion cell converts electrical energy to chemical energy, during discharge the reverse occurs. An electrochemical cell refers to the simplest independent unit of a chemical energy storage system consisting mainly of a positive electrode, a negative electrode, an electrolyte and a separator. A battery is a module of multiple electrochemical cells assembled to increase voltage and/or capacity, and it also consists of a casing and electrical connections for practical use. Higher in complexity, a battery pack is a module of a large number of assembled electrochemical cells that also contains a carefully engineered casing, a cooling and heating system, and a battery management system. An EV is powered by a battery pack, but at the research and development level, experiments are carried at the electrochemical cell level and or at the level of the individual internal components of the cell.

2.1. Electrochemistry of a Li-ion cell

Rechargeable lithium batteries had been discovered as early as the 1970s, but it is in the 1980s that the layered oxide intercalation compounds, commonly used today, were discovered. By the early 1990s, the commercialization of Li-ion batteries began.[12, 13] Figure 2.1 A shows a schematic of a common intercalation type lithium ion cell. The cell contains

a positive electrode bound to an aluminium current collector. The positive electrode contains an electrochemically active material which is typically a lithium metal oxide or lithium metal phosphate. While the active material serves as the intercalation host for the Li ions and makes up the bulk of the electrode, the electrode also contains a conductive additive such as carbon black to ensure electronic connection between the active material particles and a binder for adhesion.[13] The current collector serves to collect the free moving electrons which result from the electrochemical reaction that occurs in the active material. During discharge, the Li in the positive electrode is extracted from the material and transported as ions through the electrolyte. The electrolyte is an ionic conductor typically consisting of a solution of a lithium salt in an organic solvent. Separating the positive and negative electrode of the cell is a microporous separator whose role is to mechanically separate the two electrodes thus forcing the electron current through the external circuit to produce usable electric power. The separator must allow Li ions to be easily transported from one electrode to the other while preventing electronic conduction between the electrodes which would result in an internal short circuit. It is a microporous film of polyethylene or polypropylene and ranges between 15 and 32 μm in thickness.[14]
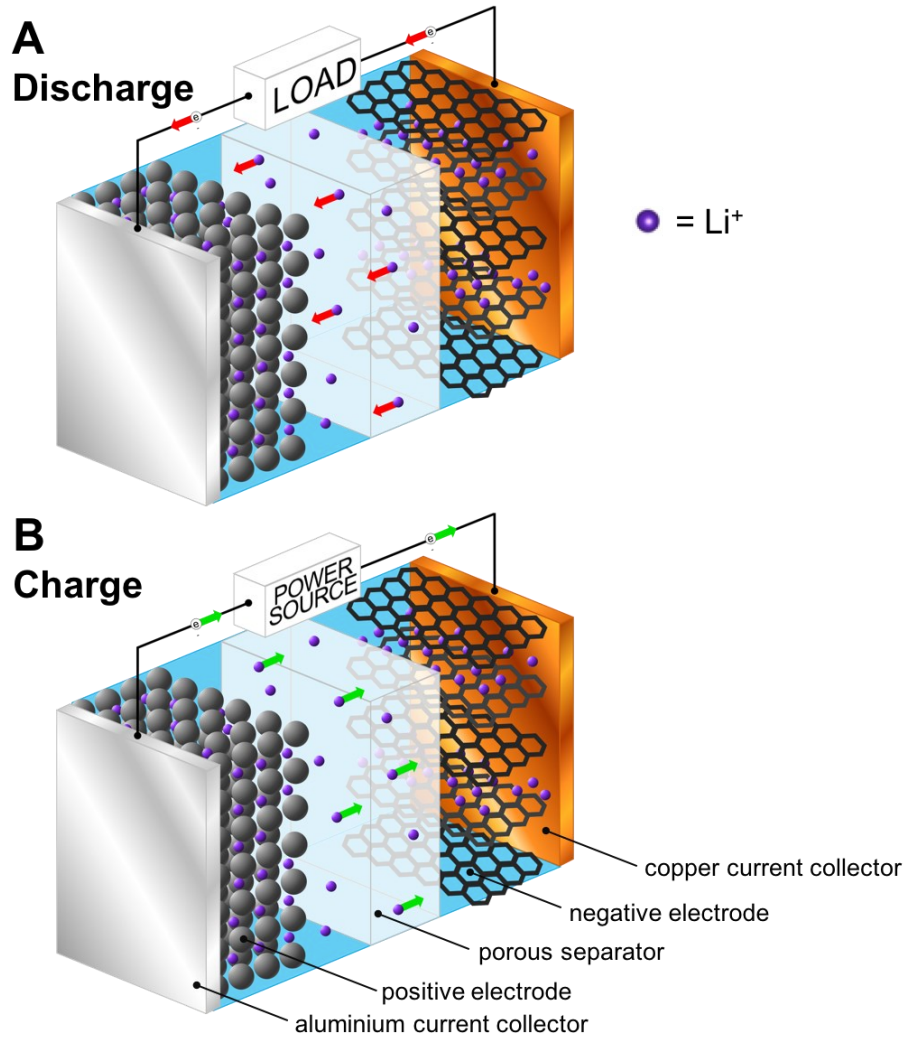
Figure 2.1. Schematic of a Li-ion cell with an intercalation compound as the positive electrode and graphite as the negative electrode

Once across the separator, the lithium ions intercalate in the negative electrode material. Graphite is frequently used as the active material in the negative electrode which is coated on a copper current collector. The different choices of current collector metals used at the cathode and the anode are due to the difference in stability of these metals at their respective potentials. When the positive electrode active material is fully delithiated, the cell is fully

charged. During discharge the reverse occurs, and lithium is extracted from the graphite in the negative electrode to intercalate in the positive electrode as shown in Figure 2.1 B.

During discharge the delithiated positive electrode active material (denoted as a lithium metal oxide $LiMO_2$ for the sake of example) is reduced becoming the cathode. During charging, the positive electrode becomes the anode as the lithium metal oxide is oxidized as per Equation [2.1].[13]

$$LiMO_2 \quad \overset{\leftarrow discharge}{\underset{charge \rightarrow}{}} \quad Li_{1-x}MO_2 + xLi^+ + xe^- \qquad [2.1]$$
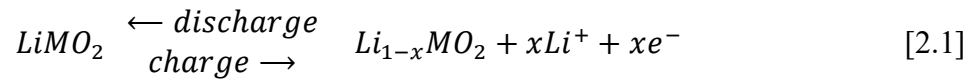
Complementarily, during discharge, the lithiated graphite (C) is oxidized and the negative electrode becomes the anode of the cell. When the cell is being charged, the negative electrode becomes the cathode as the graphite is reduced as per Equation [2.2].[13]

$$C + yLi^+ + ye^- \quad \overset{\leftarrow discharge}{\underset{charge \rightarrow}{}} \quad Li_yC \qquad [2.2]$$
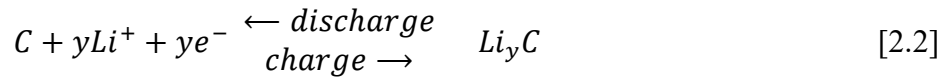
The overall redox reactions in the cell, presented in Equation [2.3], describes the back-and-forth movement of Li from one electrode to the other.[13]

$$LiMO_2 + \frac{x}{y}C \quad \overset{\leftarrow discharge}{\underset{charge \rightarrow}{}} \quad Li_{1-x}MO_2 + \frac{x}{y}Li_yC \qquad [2.3]$$
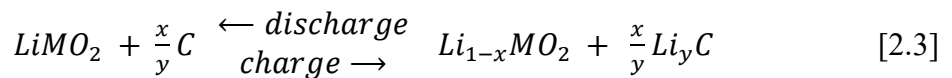
The electrons circulating from one electrode to the other in the same direction as the Li^+ are powered by the electromotive force created by the potential difference between the positive and negative electrode. This difference of potential is determined from the difference between the electrochemical potentials (μ) of the active materials in the positive and negative electrodes. It is known as the open-circuit voltage (V_{OC}) and is defined by Equation [2.4] where e is the elementary charge.[15]

$$V_{OC} = (\mu_{neg} - \mu_{pos})/e \qquad [2.4]$$

The open-circuit voltage, as the name suggests, is the voltage of the cell when it is an open circuit (connected to a load of infinite resistance) and the current is zero. This voltage differs from the voltage of the cell when it is discharging as the cell's internal resistance (R_{cell}) causes a drop in the output voltage in the presence of a discharge current. The voltage during discharge is expressed by Equation [2.5].[15]

$$V_{dis} = V_{OC} - I_{dis}R_{cell} \qquad [2.5]$$

The V_{OC} is an informative and easily observable parameter that indicates both the cell's power output and its internal resistance. During the cell's operation, the resistive properties of the cell components and capacitive properties of the interfaces between these components form the cell's overall internal impedance.

Impedance

The resistances of the current collectors, the electrodes, the electrolyte and the separator form the total internal resistance of the cell. This resistance value is not significantly affected by the change of state of charge in the cell during a charge-discharge cycle. However, it changes with the aging of a cell as the electrolyte is gradually depleted, gas evolution occurs, current collectors become corroded and microcracks or structural changes occur on the electrode particles over the course of many cycles.[16] Another contribution to internal resistance that becomes increasingly important with aging is the resistivity of films that grow on the electrodes' surfaces at the interface with the electrolyte. This film growth is most important at the negative electrode interface where a solid electrolyte interphase (SEI) will form due to the decomposition of the electrolyte.

The charge-transfer resistance is the resistance associated with the kinetics of the electrochemical reaction as lithium intercalates/deintercalates in the electrodes. This resistance is temperature-dependent and depends on the electrodes' particle size and surface area.[16] Finally, the cell's impedance is further complicated due to double layer capacitance that emerges at the interfaces of the cell's components. Analysis tools such as electrochemical impedance spectroscopy (EIS) easily and unobtrusively provide information about the cell's internal impedance which, in turn, provides diagnostics concerning the cell's state of health.[16]

There are many performance parameters by which Li-ion cells are assessed; impedance is only one, but others include specific capacity (mAh/g), power density (W/kg or W/L),

energy density (Wh/kg or Wh/L), safety and cost. The engineering design of the battery pack must also be considered when calculating practical values of performance parameters.[17] The challenge in battery design is to optimize as many of these parameters and not on one at the expense of another.

2.2. Electrodes

The positive and negative electrodes contain the only electrochemically active materials in a Li-ion cell. The properties of the electrode active materials determine many of the performance parameters of the cell. Research efforts in this field are crucial to the advancement of Li-ion battery design.

2.2.1. Positive electrode

The first commercial Li-ion battery manufactured by Sony in 1991 contained a positive electrode made of $LiCoO_2$, known as LCO.[12, 13] This lithium transition metal oxide (LTMO) of layered crystal structure remains a common choice of positive electrode material in commercial cells, but many other materials have also been successfully integrated in commercial cells today. The criteria that must be satisfied by the chosen positive electrode material are as follows:

1. The material must be capable of acting as both a reducing agent and an oxidizing agent in order to donate electrons during charge and accept electrons during discharge. For this reason, positive electrode materials will often contain transition metals (TM) as these elements can have multiple oxidation states.[12]

2. The material must be a good electronic conductor. In order for the transport of electrons to occur during the electrochemical process of the cell, the positive electrode must be a good conductor of electrons. Conductive additives, typically carbon black, are added to the positive electrode active material during electrode making. However, the more conductive the active material is, the lesser the need for the addition of electrochemically non-active materials that weigh down the cell.[12]

3. The material must be stable and must maintain structural integrity through the charging and discharging process. Additionally, thermally stable materials make for safer cells and air stability eliminates the need for costly handling and storing conditions.[12]

Other considerations, beyond these fundamental criteria, are made when choosing a positive electrode material aimed for high performance. The material should have a high capacity for storing lithium atoms and a high potential difference against the negative electrode. When designing Li-ions cell for eventual commercialization, one must also choose materials that are inexpensive, abundant, and non-toxic.[12]

Crystallographic structures

Research and commercialization efforts pertaining to positive electrode materials have been focused mainly on two different types of materials—materials of layered structure and materials of tunneled structure.[12, 13] The layered materials of most interest to positive electrode fabrication are the layered transition metal oxides (LTMO). Figure 2.2 A shows

the structure of a LTMO, exemplified by $LiNiO_2$ (LNO), which consists of a lattice of cubic close-packed oxygen atoms where the transition metal, in this case Ni, is found in octahedral sites formed by the oxygen atoms.[18] The Li atoms are intercalated in octahedral sites between the layers of oxygen and Ni atoms. In these layered materials there is one Li atom for every transition metal oxide resulting in a material of high specific capacity. A major advantage of layered materials is their high rate of Li diffusion as this crystal structure provides a 2-dimensional interstitial space for the free movement of Li.[18] In contrast, materials of tunneled structure, such as the spinel crystal structure and the olivine crystal structure shown in Figure 2.2, have 3-dimensional tunnels along which Li is free to move.
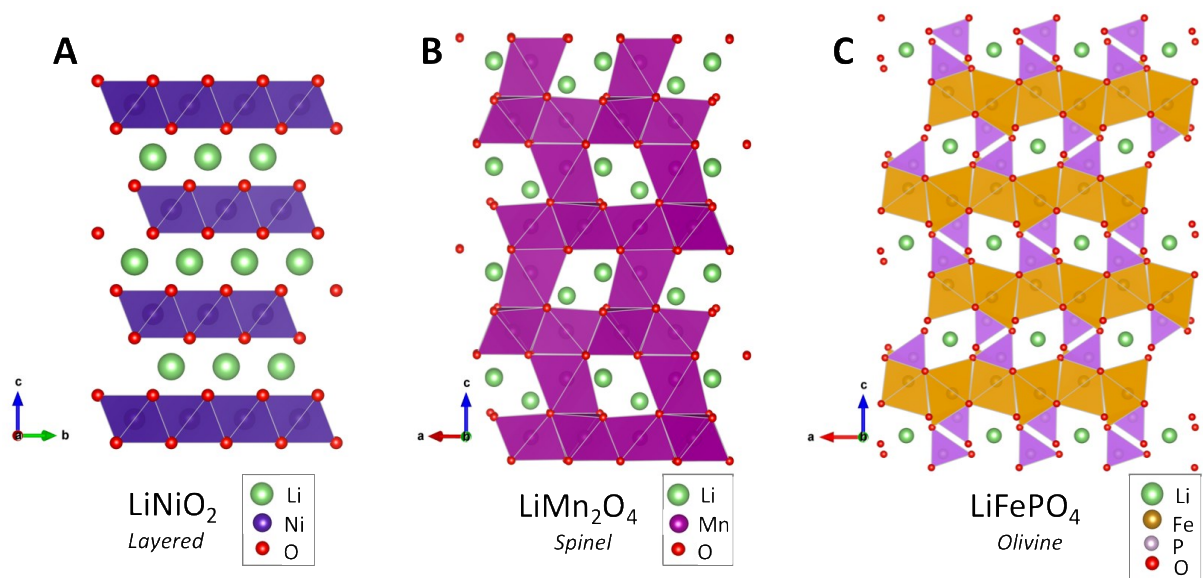
Figure 2.2. Schematics of the crystal structures exemplified by three commonly studied positive electrode active materials. Layered structure of $LiNiO_2$ (A) spinel structure of $LiMn_2O_4$ (B) olivine structure of $LiFePO_4$ (C).

The most common example of a spinel-type positive electrode material for Li-ion cells is $LiMn_2O_4$ (LMO). Figure 2.2 B shows the crystallographic structure of LMO where Mn

atoms are found in octahedral sites while the Li reside in tetrahedral sites. Unlike the layered structure, the spinel material does not consist of pure layers of lithium but rather of a multidirectional network of linked tunnels along which Li can diffuse during the intercalation and deintercalation process. The advantage of LMO is that its tunneled structure provides high Li conductivity, however, its specific capacity is low as a less Li can be stored per gram of the material relative to layered materials. Figure 2.2 C shows $LiFePO_4$ (LFP) as a prime example of an olivine-type positive electrode material structure. In the LPF crystal lattice, the P atoms occupy a tetrahedral site while the Fe and Li atoms occupy two different octahedral sites differing in size. Li atoms diffuse along 1-dimensional tunnels, but the presence of crystal defects can block these tunnels and lower Li diffusion rates in the material.[13] LFP is advantageous due to its high stability against electrolytes used in Li-ion cells but its low voltage and low tap density mean that LFP cells have lower overall energy densities.

Morphology

Positive electrode active materials are used in powder form in the fabrication of electrodes. Material powders come in different morphologies which influence the behavior of the material and affect the performance of the electrode. Active material for positive electrodes in Li-ion batteries are commonly synthesized in single crystal (SC) particles, spherical polycrystalline (PC) particles, or as nanomaterials.[13] Single crystal materials are made of 3 to 5 μm diameter particles whose exterior surface is smooth due to the lack of aggregates and grain boundaries. Ideally these single crystal grains would have an unbroken crystal lattice throughout the particle. Spherical polycrystalline particles are a spherical

agglomerate (known as the secondary particle) of thousands of small single crystals (known as the primary particles). Polycrystalline particles are characterized by rough surfaces due to grain boundaries between the primary particles. The secondary particles can range from 3 to 20 µm in diameter. Lastly, nanomaterials, such as LFP, are composed of agglomerates of nanosized primary particles. LFP can be synthesized in shapeless secondary particles, averaging 2 µm in size, composed of polydispersed monocrystalline primary particles, averaging 100-200 nm in size.[19] The morphology of the material, its tap density (the density of the powder after being mechanically tapped in a vessel) and the size of the particles, are tuned by controlling the conditions under which the precipitation process occurs during the production of the material's precursor.[13]

Transition metals in layered materials: The Co to Ni transition

As mentioned, layered $LiCoO_2$ was the active material used in the first commercial Li-ion battery and it remains to this day one of the most common choices of positive electrode materials. In a molecule with heteronuclear bonds such as $LiCoO_2$, it is useful to use the oxidation state of the present atoms to estimate their charge. Unlike ionic bonds, where there is a more distinct loss and gain of electrons from one atom to another, in covalent bonds where electrons are shared, oxidation states provide an ionic approximation of the atoms' charge based on their electron affinity. In $LiCoO_2$, Li has an oxidation state of 1+ and each O atom has an oxidation state of 2- leaving the Co with an oxidation state of 3+ to reach neutrality. As the cell charges and $Li_{(1-x)}CoO_2$ becomes increasingly delithiated (x increases from 0 to 1), the oxidation state of Co transitions from 3+ to 4+. Figure 2.3 shows the lower-lying energy band of $Co^{3+/4+}$ overlapping with the top of the O^{2-} 2p band in the

crystal lattice.[20] The Co 3d band's very low-lying energy relative to graphite's higher-lying energy band is responsible for the high OCV of 3.9 V of LCO/graphite cells.[20]
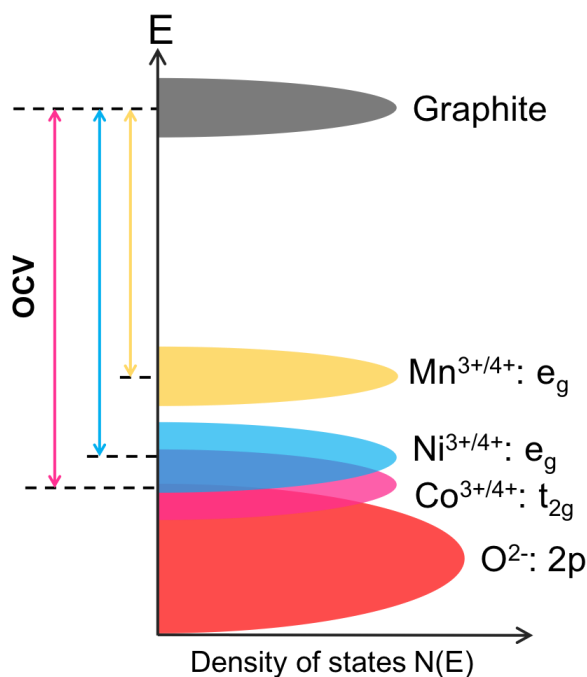
Figure 2.3. Energy diagram of the relative redox energies of redox couples corresponding to common positive electrode active materials relative to the oxygen 2p band and relative to the energy of graphite

LCO allows for the production of high voltage cells, but Co is a costly metal plagued by an unsustainable market. As of June 26, 2020, the price of cobalt was 12.93 USD/lb as opposed to the mere 5.76 USD/lb cost of nickel.[21] The cobalt mining industry has a long history of human rights violations and child-labour.[22, 23] The Democratic Republic of Congo (DRC) is where 60% of the world's supply of cobalt is mined. The cobalt market has increased in synchronization with the boom in the battery market. In fact, 50% of the extracted cobalt is used in batteries found in mobile phones, computers and electric vehicles. Additionally, the corrupt political economy governing the DRC and metal mining

companies have caused great instability in the cobalt market and has resulted in devastating environmental, social and health concerns in the region.[22, 23] The high cost of cobalt, both monetary and moral, has great weight on the overall cost of the Li-ion cell. The positive electrode material can account for more than 40% of the cost of the raw materials used in a Li-ion battery and about 24% of the overall cost of the battery pack.[24, 25] As high cost is a major barrier of entry for electric vehicles, and in addition to the limited capacities of Co-based electrodes, there has been great interest to develop alternative materials to LCO.

Figure 2.3 shows the lower-lying energy of $Ni^{3+/4+}$ to be marginally higher than that of $Co^{3+/4+}$. This will cause LNO to have a lower voltage against graphite as opposed to LCO. LNO and LCO have almost identical theoretical specific capacities as they are isostructural and both Ni and Co share similar masses. However, LNO has yet to be used in commercial cells; despite its high voltage and high accessible capacity, other complications and failure mechanisms occur in the positive electrode as its Ni content increases. As more capacity is accessed from the Ni-rich electrode, less capacity retention is observed over cycling.[26, 27] The capacity fade is a major disadvantage of Ni-rich electrodes and it has been attributed to parasitic reactions at the surface of the secondary particles and to the volume change of the crystal lattice during charge and discharge.

Drawbacks of high Ni-content materials

First, it is difficult to control LNO's stoichiometry during synthesis. Ideally, in stoichiometric LNO, all the Ni atoms would be in the 3b octahedral sites (on the Ni layer) and would have an oxidation number of 3+. This is difficult to achieve during synthesis

due to the instability of Ni^{3+} and its inclination to be reduced to Ni^{2+}. The ionic radii of Ni^{2+} ($r_{Ni^{2+}} = 0.69$ Å) is more comparable to the radii of Li^+ ($r_{Li^+} = 0.76$ Å) in comparison to Ni^{3+} ($r_{Ni^{3+}} = 0.56$ Å),[28] and the reduction from Ni^{3+} to Ni^{2+} favours the migration of Ni from the 3b sites (in the Ni layer) to the 3a sites (in the Li layer) resulting in $Li_{1-x}Ni_{1+x}O_2$. The presence of Ni in the Li layer is known as cation mixing and it hinders Li diffusion in the material.[29]

Furthermore, Ni-rich electrodes suffer from anisotropic volume changes associated with the delithiation and lithiation of the material during charge and discharge. The lattice constants of the layered crystal, namely *a*, the length of the unit cell parallel to the layers, and *c*, the height of the unit cell perpendicular to the layers, change during the electrode's operation. During charge, the Ni-rich material is delithiated and Ni^{3+} is oxidized to Ni^{4+}. As the radius of Ni^{4+} is smaller than Ni^{3+}, the crystal structure will decrease in the direction of *a*.[30] The increasing absence of Li between the NiO_2 slabs will increase the repulsion of the slabs and expand the crystal in the *c* direction. At a critical state of delithiation, the crystal interlayers collapse and a dramatic decrease in *c* is observed.[30, 31] These changes in the lattice parameters and crystal unit cell volume create strains between the primary particles that result in microcracks in the polycrystalline material. Cracks between the primary particles decrease the electrical contact within the electrode and increase the electrode-electrolyte interface area making the material more prone to parasitic reactions with the electrolyte.

The presence of Ni^{4+}, which increases with delithiation, also contributes to the rise of impedance and to thermal instability of Ni-rich materials. Ni^{4+} is highly unstable against the electrolyte and will have a propensity to reduce to a lower valency to form a spinel-like phase which then transitions to a NiO-like rocksalt phase at the surface of the material.[32] The electrochemically inactive rocksalt phase will significantly increase the electrode's resistance and contribute to the capacity fade of the cell.[33,34] This phase transformation is accompanied by a release of oxygen gas which will in turn react with the organic electrolyte and lead to cell failure.[35] This failure mechanism is accelerated by heat and delithiated LNO has proven to be less thermally stable than delithiated LCO.[36]

In addition to thermal instability, Ni-rich material are also instable in air. This complicates the handling and storage procedure for these materials. The degradation mechanism of Ni-rich materials and its impact on the material's performance are central to this thesis and will be elaborated in the following section (Section 2.2.2.).

Metal substituents

Due to the many drawbacks discussed above, safe and durable LNO electrodes have yet to be commercialized. However, batteries containing positive electrode materials where 80% of the transition metal layer is composed of Ni have shown great performance and have been successfully commercialized.[30] The partial substitution of Ni by other metals has allowed to resolve, to a certain extent, the issues presented by high Ni-content materials. Co is an obvious choice of substituent in a Ni-rich crystal since LCO has been extensively studied and Co and Ni share close atomic sizes. LCO does not suffer of cation mixing and

the synthesis of stoichiometric, well-layered Co-rich materials is more easily attainable than with Ni-rich materials. Although, the substitution of Co in the LNO crystal lattice can supress cation mixing, this is only possible at a substitution fraction of 20% or more.[37] Due to its cost, the use of large fractions of Co is not ideal and Co-substitution alone has not been able to thermally and structurally stabilize Ni-rich crystal materials. Co substitution has also failed to increase the capacity retention thus suggesting that Co-free high performance electrodes can be developed with other dopants and/or coatings.[38]

The substitution of Mn in a Ni-rich material has shown to increase the material's thermal stability. The presence of Mn stabilizes the crystal structure and hinders transitions to the rocksalt-like phase of the delithiated material. Mn-doping also increases the temperature at which oxygen evolution occurs when the delithiated material is subjected to heat hence delaying thermal runaway and increasing the material's inherent safety.[34, 39] Nevertheless, the synthesis of a layered Mn-doped material is complex and an excessive amount of Mn will deteriorate the performance of the material. When Mn in substituted in LNO, only Ni is electrochemically active and the capacity of the material sees a consequent reduction.[12]

Al is also a redox-inactive substituent that will inevitably decrease the material's theoretical capacity but offers advantages in terms of stability. [34] Al stabilizes the layered crystal structure and prevents detrimental phase-transitions which consequently, prevent microcracking and decrease capacity fade.[30] Al-doping improves the material's thermal stability and safety by increasing the onset temperature of thermal runaway even at high

21

delithiation states.[40] Despite decreasing the theoretical capacity of the material, Al-doping allows for a safer access to more practical capacity and high average voltage.[30, 40]

Since not one known metal substituent can resolve the drawbacks of Ni-rich materials, they are often combined to optimize the overall performance of the material. Hence the successful commercialization and high performance of $LiNi_{1-x-y}Mn_xCo_yO_2$ (NMC) and $LiNi_{1-x-y}Co_xAl_yO_2$ (NCA). In this thesis, the effect of water washing on four different Ni-rich positive electrode active materials will be presented.

The list of materials along with information on how they were acquired, their median diameter size, their metal composition as well as their average specific surface area measured from Brunauer-Emmett-Teller (BET) surface area analysis (discussed in Chapter 3) are provided in Table 2.1. This list of materials was chosen in order to assess the difference in surface reactivity among Ni-rich materials of different Ni-content and of different morphologies.

Table 2.1. List of positive electrode materials studied.

	Supplier	D50 (µm)	Composition of the transition metal layer	Average Specific Surface Area (m²/g) ± SD
LNO	Synthesized as per Section 3.1	15	100% Ni	0.25 ± 0.10
NCA	Umicore (Korea)	10	83% Ni 15% Co 2% Al	0.18 ± 0.07
NMC532 Polycrystalline (PC)	Guizhou Zhenhua E-chem Inc. (Shenzhen, China)	10	50% Ni 30% Mn 30% Co	0.18 ± 0.07
NMC532 Single crystal (SC)	Guizhou Zhenhua E-chem Inc. (Shenzhen, China)	3-5	50% Ni 30% Mn 30% Co	0.44 ± 0.20

2.2.2. Impurity growth on electrode surface

As was briefly mentioned, a major drawback of Ni-rich positive electrode materials is their instability in air. Ni-rich materials are advantageous to Co-rich materials in terms of raw material cost, but the necessary handling and storing of these materials under controlled conditions is an additional cost and is an inconvenience in industry. Resolving the problem of Ni-rich material degradation in ambient atmosphere will be greatly beneficial to the commercialization of higher Ni-content materials.

The degradation of lithium metal oxides occurs when Li near the surface of the particles deintercalates to react with water, oxygen and/or carbon dioxide in air. These reactions

form lithium oxide (Li_2O), hydroxide (LiOH), lithium carbonate (Li_2CO_3) and lithium bicarbonate ($LiHCO_3$) impurity species on the surface of the material. The air stability of lithium metal oxides is closely related to the voltage of the material. Voltage is a measure of the binding energy of the lithium in the crystal lattice; the higher the voltage of the material, the more bound the Li atoms are and the less prone they will be to deintercalate at the surface to form impurities.[41] For instance, LCO has an OCV near 3.9 V vs. Li/Li^+ [42] while LNO's OCV is near 3.5 V vs Li/Li^+ [43]. For this reason, LCO has higher air stability and will maintain a more pristine surface when exposed to air relative to LNO.

The presence of impurity species on the electrode particles' surface have damaging effects on the cell's cyclability, its energy density and even its safety. Most evidently, the trapping of electrochemically viable Li in the impurity compounds will result in reduced capacity. Matsumoto *et al.* showed that Ni-rich lithium metal oxide (containing 81% Ni) exposed to 55% relative humidity (RH) at room temperature would lose 8% of its active lithium to impurity growth; at elevated temperatures, the Li lost to the formation of impurity can reach 70%.[44] In fact, a sensitive and practical way to monitor the impurity growth on a material is to simply monitor its OCV since this voltage would increase with increased deliathiation.[45] Transition metal reduction has been frequently reported with the growth of lithium impurity; it is thought to be another causational factor of surface air instability.[32, 46–49] It is believed that the reduction of the metal leaves readily reactive oxygen species which in turn reacts with H_2O and CO_2 in air. These reactions produce carbonates, bicarbonates and hydroxide compounds that then react with loosely bound Li atoms at the surface of the material to form Li_2CO_3, $LiHCO_3$, and LiOH impurities. For instance,

$LiMn_2O_4$ owes its superior air stability to its content of stable Mn in addition to its high voltage (around 4.0 V against Li^+/Li).

An increase in cation disorder has been particularly observed in Ni-rich materials following exposure to air. This means more trivalent Ni is being reduced to divalent Ni leading to the structural transition of the material's surface to the spinel-like phase and to the rocksalt-like phase.[32] This phase transition leaves active oxygen sites which are thought to further promote the reactivity of the material's surface.[50] The spinel-like phase and the electrochemically inactive rocksalt phase formed at the delithiated surface and subsurface region of the material particle reduce the electronic and ionic conductivity of the electrode. In addition to this transformed phase of low conductivity, it has been shown through impedance analysis that the layer of adsorbed impurities itself also increases the resistance of the electrode and impedes the intercalation and deintercalation kinetics.[51] An increase in resistance due to impurities could lead to higher heat dissipation in the cell which is far from ideal considering the poor thermal stability of Ni-rich materials.

Another detrimental effect of the presence of carbonate impurities on the electrode materials is the evolution of gas associated with the decomposition of the impurity species. It has been suggested that carbonate impurities on the surface of the electrode are oxidized during the cell's first cycle. Renfrew et al. have shown that the oxidation of Li_2CO_3 adsorbed to the surface of Ni-rich electrode materials is responsible for CO_2 and CO evolution in the cell during charging starting at around 3.5 V and up to 4.8 V.[52, 53] The evolution of O_2 has also been found to be correlated with the presence of Li_2CO_3; this

indicates that impurities are related to the release of oxygen from the electrode active material and compromise the cell's safety.[49, 52] Residual lithium compounds on the surface of the electrode material, even at the impurity level, have harmful effects on the electrode's stability, impedance and safety. Surface impurities on electrode materials also cause practical challenges to electrode fabrication in industry. During electrode slurry preparation, the lithium compounds on the surface of the active material cause an increase in pH due to the basicity of the impurity compounds. This increase in pH results in the gelation of the slurry and hinders the fabrication of quality electrodes.[54]

Removal of electrode surface impurities

The detriments of impurity species on positive electrode active materials are many; the removal of these species before electrode fabrication is crucial particularly for Ni-rich materials which have a propensity for impurity growth. Reheating the material is an effective way of purifying the surface; LiOH and Li_2CO_3 decompose at 410 °C and 710 °C respectively.[45] However reheating at high temperatures is not ideal and must be carefully done to avoid Li diffusion towards the surface of the particles and cation mixing.[55] What is most commonly done in industry to remove surface impurities is a water washing of the materials followed by a drying step at low temperature.[56, 57] The water solubility of Li_2CO_3 is 1.3 g/100 mL and LiOH is 12.4 g/100 mL at room temperature.[58] This makes these impurities conveniently and reliably removable by water rinsing. It is, however, concerning to be exposing these humidity-sensitive materials to water; indeed there are undesirable side-effects that are suspected to accompany this washing process that would cause the deterioration of the electrochemical properties of the material.[30] It has been

suggested that when exposed to water, Ni-rich materials especially, will undergo a Li^+/H^+ ion exchange which will delithiate the surface and subsurface region of the particles and fill the vacant Li sites with H^+ from the aqueous solution to maintain electrical neutrality.[59, 60] The temperature at which the following drying step is done is also a dominant factor in the resulting surface structure of the material;[56] preferable, this temperature should be between 120 °C and 250 °C to avoid undesirable changes in the structure.[57]

Other alternatives to using water to wash Ni-rich materials have been tested. Non-aqueous solvents such as alcohol have been studied for their effectiveness to remove surface impurities. These alternative are not as practical in industry and are likely to add cost and complication at scale.[61] Whether to investigate alternatives to the conventional washing process or to improve the utilized process itself, a fundamental understanding of the reaction between positive electrode materials and water is needed.

2.2.2. Core-shell materials

Ni-rich materials provide high capacity and energy density but suffer from poor surface stability. To benefit from the high performance corresponding to high Ni-content while stabilizing the material, different techniques such as doping and coating have been tested. The design of core-shell (CS) particles integrates these two approaches to minimize the compromise between energy and stability.[62] A core shell material is a material whose particles have an interior bulk region (the core) and an exterior layer (the shell) each differing in elemental composition as shown in Figure 2.4.
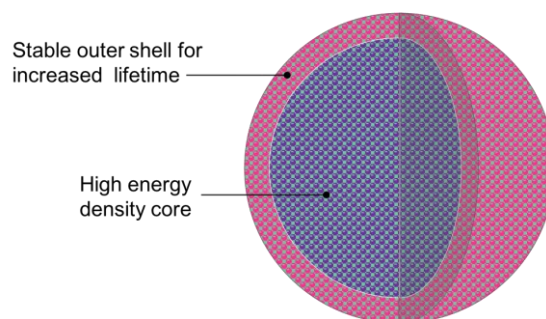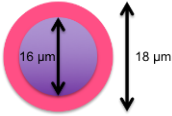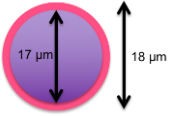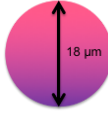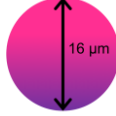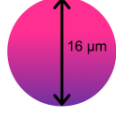
Figure 2.4. Schematics of a core-shell material particle cut to show the different composition of the core and shell regions.

To avoid the disadvantages of a structural mismatch between the core and shell, the change in composition in a core-shell particle occurs gradually.[63] For instance, a particle designed with a Ni-rich core for high energy and capacity and a Mn-rich shell for higher surface stability will contain a concentration of Mn that will gradually decrease from the surface of the particle to its interior. Core-shell particle designs have proven to be effective ways to improve the thermal stability of positive electrode materials. The problematic oxygen evolution which occurs due to the layered phase to spinel phase transformation has an onset temperature around 200°C in Ni-rich materials. In a core-shell material with a Ni-rich core and a Mn-rich shell, this exothermic onset temperature has been increased up to 235°C and even to 280°C depending on the thickness of the shell.[64] The thickness of the shell can vary from the nanometer to the micrometer scale; the tuning of the shell's thickness and composition allows for the design of positive electrode material with targeted performances. In this thesis, the reaction of Ni-rich positive electrode materials to water is tested and compared in both conventional particles of uniform composition as well as core-shell materials. Table 2.2. Table of core-shell materials tested and comparative materials. lists the core-shell materials studied as well as some uniform materials used for comparison analysis.

Table 2.2. Table of core-shell materials tested and comparative materials.

Labels	CS LNO:Ni80Mn20 16:2	CS LNO:Ni80Mn20 17:1	LNO	NMC811	Ni80Mn20
Supplier	Synthesized as per Section 3.1	Synthesized as per Section 3.1	Synthesized as per Section 3.1	Umicore (Korea)	Umicore (Korea)
D50 (µm)	18	18	18	16	16
Average Specific Surface Area (m^2/g) $\pm$ SD	1.46 $\pm$ 0.02	1.07 $\pm$ 0.06	0.93 $\pm$ 0.10	0.22 $\pm$ 0.01	0.21 $\pm$ 0.02
Core	16 µm radius Composition: LiNiO$_2$ (100% Ni)	17 µm radius Composition: LiNiO$_2$ (100% Ni)	Uniform composition of LiNiO$_2$	Uniform composition of LiNi$_{0.8}$Mn$_{0.1}$Co$_{0.1}$O$_2$	Uniform composition of LiNi$_{0.8}$Mn$_{0.2}$O$_2$
Shell	1 µm thickness Composition*: LiNi$_{0.8}$Mn$_{0.2}$O$_2$ (80% Ni, 20% Mn)	0.5 µm thickness Composition*: LiNi$_{0.8}$Mn$_{0.2}$O$_2$ (80% Ni, 20% Mn)			
Overall composi-tion of the transition metal layer	Ni 93.5%, Mn 6.5%	Ni 97.23%, Mn 2.77%	Ni 100%	Ni 80%, Mn 10%, Co 10%	Ni 80%, Mn 20%
Schematics					

* N.B. The listed shell compositions are target compositions, variations to the shell compositions can occur after heat treatment

The shell thickness and composition presented in Table 2.2 represent the target parameters of the material. Diffusion of the transition metals during the lithiation process, especially when done at very high temperatures, can form thicker shells of different compositions when compared to the gradient-composition of the precursor materials. The Energy-dispersive X-ray spectroscopy (EDS) results shown in Figure 2.5 show the actual concentration of Ni and Mn across the particles. EDS analysis has served to confirm that the materials have maintained their core-shell structure and have relatively maintained their intended shell thicknesses.
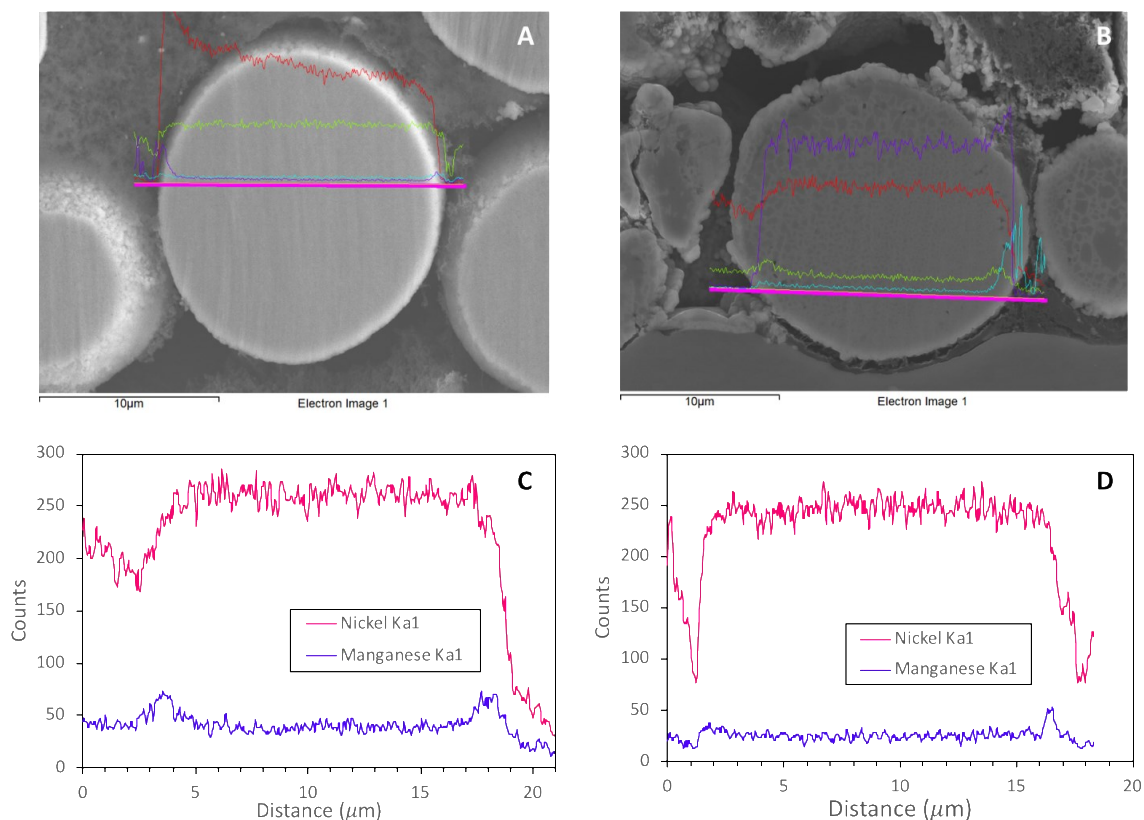
Figure 2.5. Cross sectional SEM image of the CS LNO:Ni80Mn20 16:2 (A) and CS LNO:Ni80Mn20 17:1 (B) The magenta lines shown across the imaged particle define where the linescans were measured. EDS linescans of CS LNO:Ni80Mn20 16:2 (C) and CS LNO:Ni80Mn20 17:1 (D).

2.2.5. Negative electrode

Opposite to the positive electrode, the negative electrode of the Li-ion cell is also a layered material capable of intercalating and deintercalating Li ions. While the first commercialized Li-ion cell contained a positive electrode made of $LiCoO_2$, its negative electrode was made of coke. Eventually, as higher quality graphite became available, negative electrode materials have become, and remain today, mostly graphite-based.[13] Graphite is an excellent active material for the negative electrode; it is inexpensive and abundant, and it has a low voltage against commonly used positive electrodes.[65] Graphite undergoes minimal strains and structural changes when inserting and removing Li, allowing it to provide excellent reversibility. As shown in Figure 2.6, Li resides in interstitial sites of the host graphite material. However, every 6 atoms of carbon can only intercalate 1 Li ion. The limited number of intercalation sites for Li result in poor specific capacity for graphite electrodes. For this reason, there has been great interest in testing alloyed negative electrodes composed of Si, Ge or Sn. In these materials, Li is not intercalated in the host structure, but rather, it breaks the bonds in the host material and forms a Li-alloy.[66] This type of alloying allows negative electrodes to reach high capacities; for instance, Li-Si alloys can reach an equilibrium phase with Li contents as high as $Li_{22}Si_5$, or 27 times as much Li stored per host atom than in graphite. Si is a promising and abundant material, but the drawback of Si alloys is the dramatic change of volume and structure that these materials undergo.[67] More work is expected in the near future in the development of alloy negative electrodes.[66]
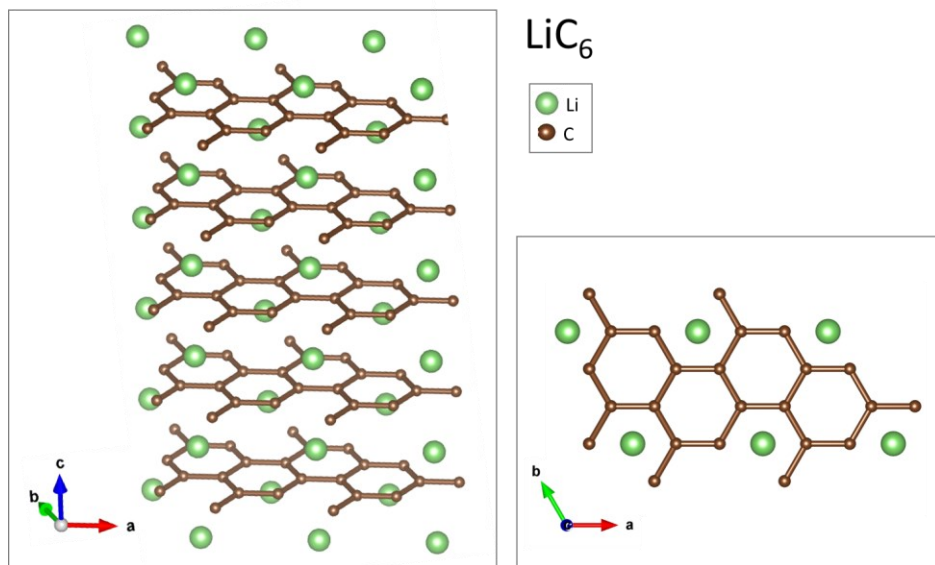
Figure 2.6. Schematics of the structure of the common negative electrode material graphite. This schematic shows the graphite fully lithiated (LiC_6).

2.3. Electrolyte

The electrolyte in a Li-ion cell is the medium by which Li-ions are transported from one electrode to the other. It is typically a liquid solution, but there has been great interest in solid electrolytes for their advantage in cell safety. A dominant majority of liquid electrolytes are electrolytic solutions consisting mainly of a solvent and a Li-based salt. Ideally, the electrolyte should play a passive role in the functioning of the cell and should not undergo any net chemical transformations; all Faradaic reactions should occur exclusively in the electrodes. Therefore, the electrolyte solvent is required to be inert against both electrodes and against other components of the cell (cell separator, current collectors, cell packing, etc.). This means it must have a wide electrochemical window to allow a high potential difference between the electrode without electrolyte degradation.

Additionally, since the electrolyte must be an ionic conductor and an electronic insulator, the solvent must have a sufficiently high dielectric constant to allow the dissolution of a high concentration of salt which will result in high ionic conductivity. Other properties such as thermal stability, viscosity, and flash point must be considered when choosing electrolyte solvents.[68] These many, and often contradictory, requirements make it impossible to develop a single high-performing solvent substance. The solvent used in Li-ion cells is typically a blend of carbonates such as ethylene carbonate (EC), dimethyl carbonate (DMC), ethyl methyl carbonate (EMC) or diethyl carbonate (DEC).[68] Esters such as methyl acetate (MA) have also been used in solvent blends to improve rate capabilities.[69, 70]

As opposed to the large selection of solvents, the choices for the solute are limited. The lithium salt must completely dissolve in the solvent, and the Li cation must have high mobility while the anion must remain inert in the cell.[68] $LiPF_6$ is the most commonly used salt in commercial applications due to its ionic high conductivity and safety. However, $LiPF_6$ reacts with water to produce hydrofluoric acid or HF, rendering the handling of this salt difficult. This also means that any residual water that finds its way in a Li-ion cell containing $LiPF_6$ could produce corrosive HF as per Equation [2.6].[71, 72] There has also been evidence of the reaction of $LiPF_6$ and Li_2CO_3 impurities to produce CO_2 gas and LiF as per Equation [2.7].[73] These parasitic reactions are both detrimental to the performance of the positive electrode (electrode dissolution) and to the cyclability of the cell.

$$LiPF_6 + H_2O_{(trace)} \leftrightarrow LiF + 2HF + POF_3 \qquad [\,2.6\,]$$

$$LiPF_6 + Li_2CO_3 \rightarrow POF_3 + CO_2 + 3LiF \qquad [\,2.7\,]$$
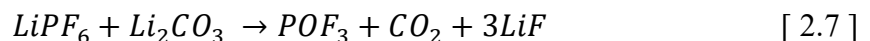
2.3.1. Positive electrode dissolution

Acid species in the electrolyte can attack the positive electrode and cause transition metal dissolution. The lithium salt ($LiPF_6$) can introduce HF species in the cell and the electrolyte solvent can also introduce trace amounts of water or alcohol that will produce acidic species. For this reason, the control of impurities and the control of the atmosphere in which materials are handled and cells are fabricated is of great importance.[74] Furthermore, at high voltages, the electrolyte solvent will begin to decompose due to its thermodynamic instability. This decomposition reaction can also yield acids such as HF which can cause metal dissolution at the positive electrode.[75] The degradation of the electrolyte is a particularly prominent challenge with Ni-rich materials. The presence of Ni^{4+} following delithiation of the material and the reactivity of Ni^{4+} towards the electrolyte solvent promote solvent oxidization. The oxidized species form a thin interphase at the surface of the electrode that simultaneously promotes the reduction of Ni^{4+} to its soluble divalent state Ni^{2+}.[76] Thus, it appears that the parasitic degradation of the electrolyte and the transition metal dissolution of the positive electrode material are intertwined mechanisms that must be addressed together. Metal dissolution is an issue that affects not only the electrolyte and the positive electrode, but also the negative electrode as the dissolved metals can travel through the separator and deposit on the negative electrode resulting in reduction in cell lifetime.

CHAPTER 3. Experimental Methods

The experimental method used in this study aimed to shed light on the reaction mechanism between Ni-rich positive electrode materials and water. The motivation behind these experiments was to better understand the effect on material washing as it is done in industry and to validate any proposed reaction mechanisms. This chapter will describe the synthesis of the materials as well as the washing conditions and humid air conditions to which the materials were subjected. Following these tests, both the resultant materials and the resultant washing solutions were analysed accordingly.

3.1. Materials synthesis

The LiNiO$_2$ polycrystalline powder used in this study was obtained from a solid-state synthesis using an Ni(OH)$_2$ precursor and LiOH by the reaction shown in Equation [3.1].

$$Ni(OH)_2 + Li(OH)_2 \cdot H_2O \; \rightarrow LiNiO_2 + 3H_2O \qquad\qquad [\,3.1\,]$$

The Ni(OH)$_2$ precursor purchased from Guizhou Zoomwe Zhengyuan Advanced Material Co., Ltd (China) has a polycrystalline morphology with secondary particles of 15 μm (D50) diameter. The precursor is then mixed with LiOH·H$_2$O (purity > 99.8%) obtained from FMC Corporation, and both powders were hand milled with a mortar and pestle. The mass of each reactant was calculated to ensure a 1.02 Li:Ni ratio; excess Li is used in order to synthesize stoichiometric and well-layered LNO with little Ni in the Li layer. The mixture

was then heated in a tube furnace under O_2 flow at a heating rate of 10°C/min to a temperature of 480°C. An isothermal step of 3 h occurs at 480° to ensure uniform melting and mixing of the LiOH. The mixture was then taken out of the cooled tube furnace and hand milled again before being returned to the furnace and heated to 700°C for 20 h under O_2 flow. These conditions are known for being the optimum ones under which the highest performance LNO is synthesized.[77]

The two core-shell materials also studied were synthesized very similarly to LNO. The precursors used for the synthesis of core-shell $LiNi_{0.935}Mn_{0.065}O_2$ and core-shell $LiNi_{0.9723}Mn_{0.0277}O_2$ were $Ni_{0.935}Mn_{0.065}(OH)_2$ and $Ni_{0.9723}Mn_{0.0277}(OH)_2$ respectively. In other terms, these precursors, also obtained from Zoomwe Zhengyuan Advanced Material Co., Ltd (China), are themselves in core-shell form. The synthesis process aims to lithiate the core-shell precursors while maintaining the gradient composition of the transition metals. Overheating the core-shell materials would cause the transition metals to diffuse uniformly throughout the material particle, while underheating the materials will not result in full crystallization. The target composition of the shells in both CS materials synthesized is 80% Ni and 20% Mn, while the cores contain only Ni. The first CS material, $LiNi_{0.935}Mn_{0.065}O_2$, which has a 16 µm diameter core and a 1 µm thick shell, is best synthesized at 750°C. While $LiNi_{0.9723}Mn_{0.0277}O_2$, which has a 17 µm diameter core and a thinner 0.5 µm shell, is best synthesized at 700°C. To the exception of the precursor choice and the final heating temperature, the same steps employed to synthesize LNO were followed to synthesize core-shell $LiNi_{0.935}Mn_{0.065}O_2$ and $LiNi_{0.9723}Mn_{0.0277}O_2$.

3.2. Positive electrode material washing method

The washing tests consisted of adding 0.5 g of material to 100 mL of deaerated distilled water in a closed glass vial. Deaerated water was used so the effect of water could be tested without the interference of any dissolved gases; the glass vial was also sealed with parafilm to ensure little to no CO_2 leakage. A magnetic stirring bar was added to the solution to prevent the powder from settling and to promote uniform water exposure to all material particles. The stirring periods were either 15 min, 30 min, 1 h, 4 h, 6 h, 24 h or 48 h, and these times were measured from the second the material came in contact with the water until the powder was separated from the mixture. The second step involved centrifuging the powder-water mixture. This step is crucial for easy filtering and easy material recovery. The mixture was transferred to a centrifuge tube and subjected to a g-force of 900 g. The duration of centrifugation did not exceed 10 min. For samples that were washed for only 15 min and 30 min, 3 and 5 min of centrifugation, respectively, were sufficient. Lastly, once centrifuged, the mixture was vacuum filtered through a Whatman grade 5 filter (particle retention size of 2.5 µm). A fine-pore filter was used to retain any degraded small particle pieces that may have been produced during the washing step. Figure 3.1 shows the three-step washing process.

After the washing test, the filtrate was kept in a closed glass vial, while the recovered material was dried for 1 to 2 h at low heat (70^oC). Low heat was used to avoid any structural changes to the material. The studied materials listed in Table 2.1 were consistently subjected to the above washing procedure. Additionally, an acid washing test was similarly conducted. The same steps were repeated with a dilute solution of 0.05 M HCl instead of

deaerated distilled water. The objective of the acid washing test was to observe the Li^+/H^+ exchange process when the material was exposed to a high concentration of H^+. However, the acid concentration had to be carefully chosen; these LTMOs will fully dissolve in strong acidic solutions of high concentrations. Therefore, a 0.05 M concentration of HCl was chosen as no visible material dissolution was observed at that concentration. The acid solution was prepared with stock concentrated HCl and was diluted with deaerated distilled water. The core-shell materials and their comparative uniform materials, listed in Table 2.3, were tested under the same washing conditions to the exception of washing 0.25 g of material with 100 mL. The ratio of the mass of the material to the volume of the washing solution is an important factor in the consequent reaction. This ratio must be maintained when comparing the reactivity of different materials.
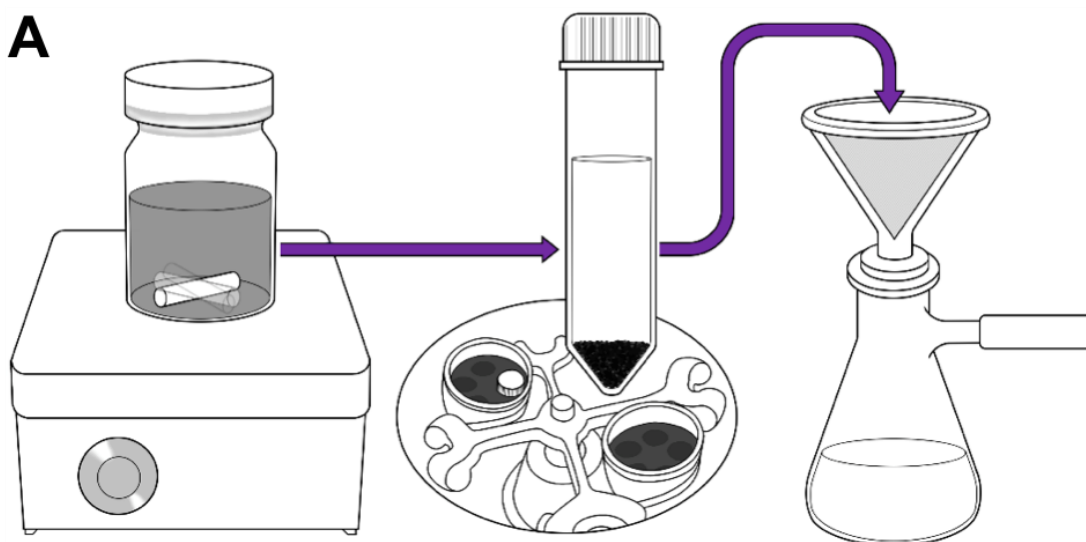
Figure 3.1. The three-step washing method consisting of stirring the material with the washing solution (deaerated distilled water or dilute HCl), centrifuging, and vacuum filtering.

Throughout the washing process the pH of the solution increases. There was interest in testing the effect of washing the positive electrode materials at constant pH. A continuous stirred-tank reactor (CSTR) Brunswick Scientific/Eppendorf BioFlo 310 was used for its pH control function to achieve this condition. This allowed for the stirring mixture to maintain a constant pH by adding drops of acid to the mixture to compensate for the rise in pH. A pH probe was inserted in the glass vial where the powder-solution mixture was stirring. When the probe reading exceeded the set pH, a peristaltic pump would begin adding acid solution drops to the mixture until the set pH was attained again, at which point, the pump would stop. This controlled feedback system was maintained for the duration of the washing test—24 h. Washing tests at constant pH values of 2, 7 and 10 were conducted. A 0.01 M HCl solution was prepared for the test at a constant pH value of 2. As this low pH required a large quantity of acid to be maintained, an HCl solution of 0.1 M was used as the "drop-solution". The test at pH 7 simply required deaearated distilled water, and a solution of NaOH dissolved in deaerated distilled water was prepared for the pH 10 test. To maintain pH values of 7 and 10, less acid was required than in the case of the test at constant pH 2, therefore a weaker 0.05 M solution of HCl was used as the "drop-solution". The concentration of the drop solution had to be high enough to minimize changes in the material to washing solution volume ratio, but also needed to be low enough to provide smooth constant pH and minimize acid shock and pH spikes during the washing period. Figure 3.2 illustrates the modified setup for the constant pH stirring step, this step was then followed by the same centrifugation and filtration steps described above.
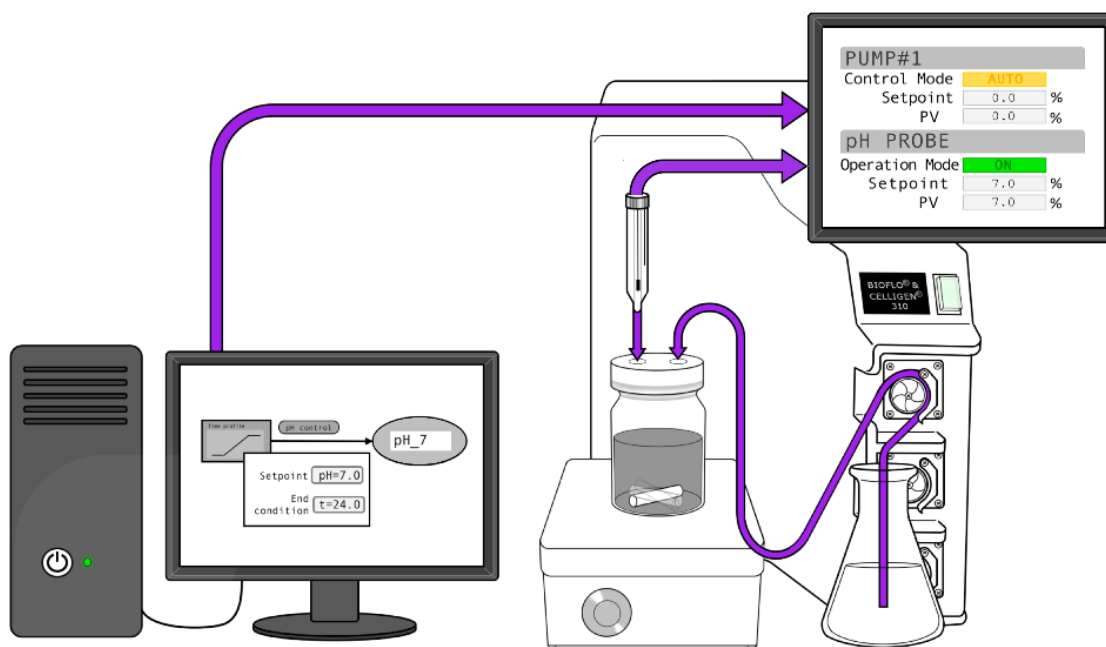
Figure 3.2. Schematics of the modified stirring first step to achieve constant pH washing.

3.3. Positive electrode material exposure to humid air

Core-shell materials and their comparative materials listed in Table 2.3 were also exposed to humid air. A humidity chamber was created by using a desiccator and by replacing the desiccant with water. The desiccator lid was then sealed with vacuum grease as shown in Figure 3.3. This created an isolated environment with a relative humidity (RH) of 99%. Temperature and humidity sensors were kept inside the desiccator to monitor constant 99% RH and stable ambient temperature (around 22°C). The tested samples consisted of 0.5 g of each material on small weighing boats and were left in the humidity chamber for durations of 15 min, 30 min, 1 h, 2 h, 4 h, 1 day, 4 days, 8 days, or 16 days. The effects of humid air exposure were less severe than those of water or acid exposure and required

longer testing times to clearly observe any transformations. At the end of each test duration, the samples were removed from the humidity chamber to be characterized or to be stored under vacuum.
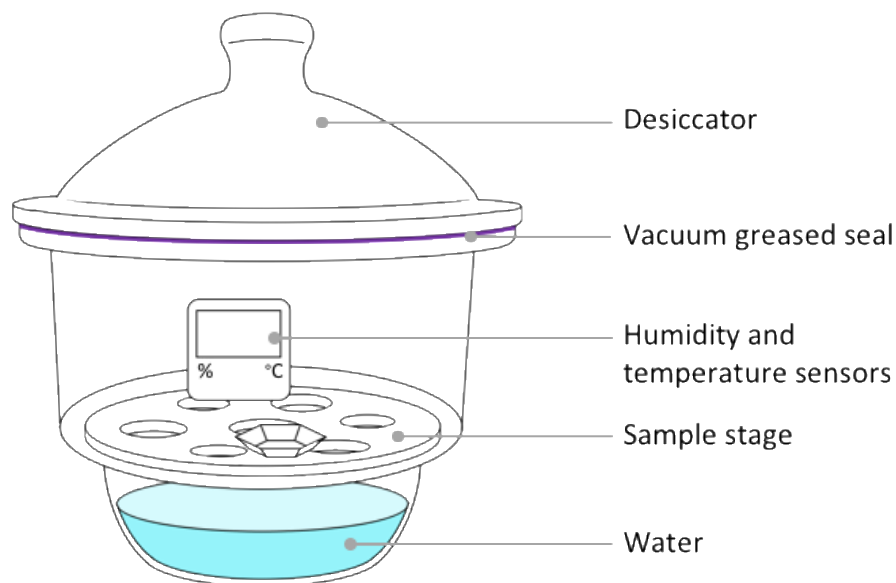
Figure 3.3. Desiccator used for creating a humidity chamber for air exposure tests.

3.4. Material characterization

3.4.1. Brunauer-Emmett-Teller (BET) surface analysis

Brunauer-Emmett-Teller (BET) surface analysis is a technique to measure the specific surface area (m^2/g) of a material. This technique relies on the concept of adsorption and desorption of an adsorbate (typically a gas) on the adsorbent (the material whose specific surface area is of interest). Adsorption is a surface phenomenon in where an adsorbate adheres to the surface of an adsorbent to form a thin layer. The Micromeritics FlowSorb II 2300 BET analyzer used to obtain the specific surface area measurements in this study uses

a gas mixture of N_2 and He where N_2 is the adsorbate. The material sample, or the adsorbent, is first dried from any adsorbed moisture then placed in a cooling bath of liquid N_2 before being exposed to a known concentration of the gaseous mixture. The adsorption of N_2 on the sample reduces the N_2 concentration which is then replaced by He gas. Consequently, due to the higher thermal conduction of He gas, the thermal conductivity of the gaseous mixture increase. When the cooling bath is removed, desorption occurs, and thermal conductivity decreases. The change in the thermal conductivity signal is indicative of the amount of N_2 adsorbed on the surface which is in turn indicative of the surface area of the sample. When comparing surface reactivity of different materials, as is done in this study, it is critical to consider surface area.

3.4.2. Scanning electron microscopy (SEM)

Scanning electron microscopy (SEM) is an analysis technique which allows for the imaging of materials to observe their morphology and the topology of their particle surfaces. The image is produced by scanning the sample with a beam of focused electrons. An electron gun generates a beam of electrons which are then accelerated by a voltage applied to an anode. The beam then travels through a system of apertures and electromagnetic lenses which aims to focus the electron beam to provide high resolution images.

The interaction between the electrons and the samples produce different signals that provide different information about the sample. Scanning electron microscopes are typically equipped with a secondary electron detector; secondary electrons provide topographic information about the sample and allow for the imaging of the morphology

and surface of the material particles. A backscattered electron detector however, collects signals from backscattered electrons, which increase with increasing atomic number, to provide compositional information about the sample. Figure 3.4 shows the working principle of a scanning electron microscope. The SEM images in this thesis were obtained from a Hitachi S-4700 equipped with a secondary electron detector. The samples were mounted on stubs coated in carbon paint to ensure good adhesion when the sample was placed under vacuum. The accelerating voltage used for imaging was of 3 kV and the emission current was 20 nA.
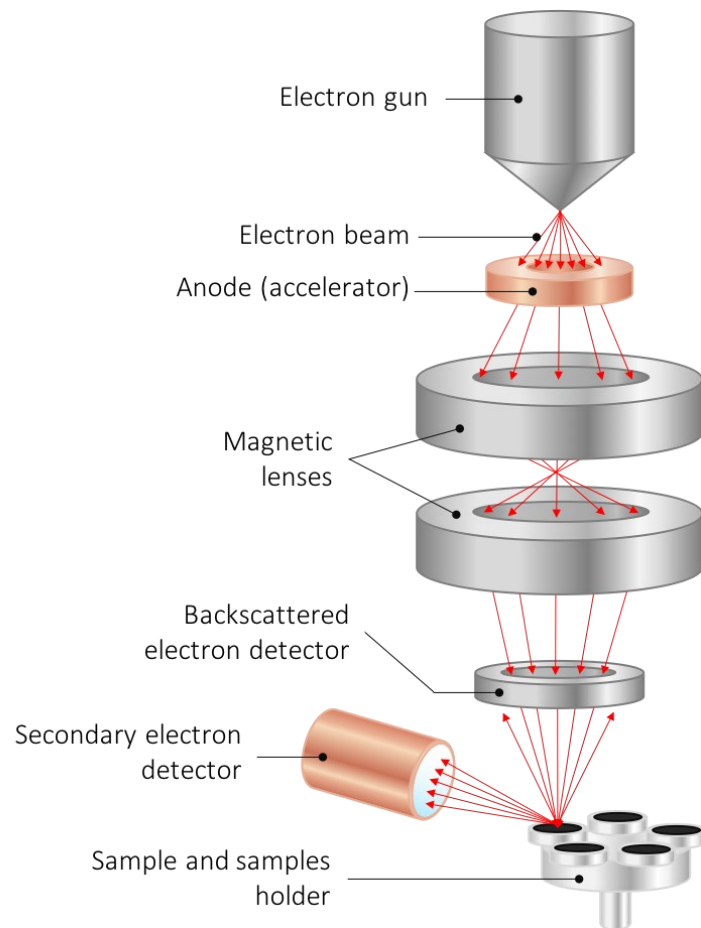
Figure 3.4. Schematic of the working principle and main parts of a scanning electron microscope.

3.4.3. X-ray diffraction (XRD)

X-ray diffraction analysis provides useful information about the crystalline phases and the lattice constants of a material. An X-ray diffractometer uses a cathode ray tube and an optics system to produce a collimated beam of X-rays. A monochromator is also used either at the X-ray source or at the detector level to provide a monochromatic beam. The X-ray beam is incident on the sample at a specific angle and the crystal lattice of the sample acts as a 3-dimensional diffraction grating which diffracts the incident beam towards the detector as shown in Figure 3.5. Constructive interference of the diffracted electromagnetic waves occurs only at angles that satisfy Bragg's Law.

$$n\lambda = 2dsin\theta \qquad\qquad [\,3.2\,]$$

Braggs's Law, Equation [3.2], where n is an integer, expresses the relation between the wavelength of the incident X-rays, λ, the diffraction angle, θ and the crystal lattice spacing, d. The X-ray source and the detector move in synchronization in an orbit around the sample in order to scan the sample across a wide range of 2θ angles. This should cover all possible diffraction directions of the lattice, since the powder sample contains a large number of crystalline particles in random orientation. As a result, an XRD profile is obtained where the diffracted rays seen by the detector are measured, and Bragg peaks are observed at specific 2θ angles over the processed range. XRD profiles can be used to identify materials and to extract valuable information about their crystallographic properties.
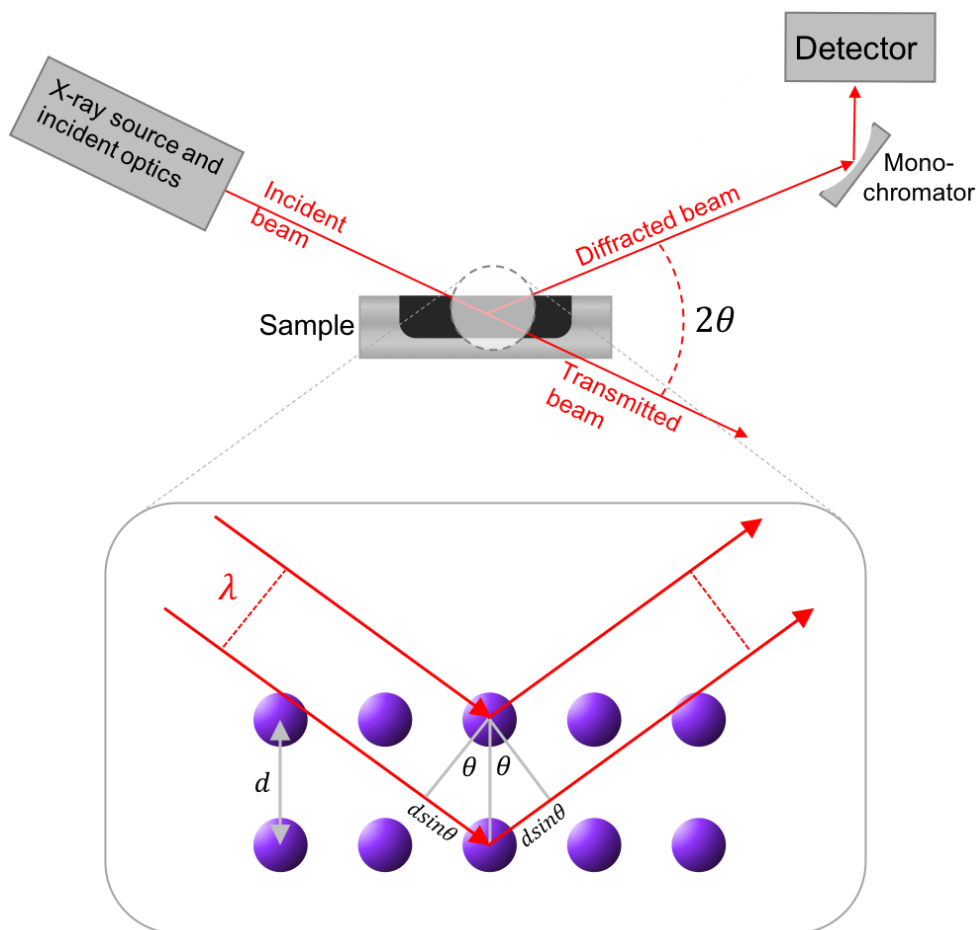
Figure 3.5. Schematic of the working principle of an X-ray diffractometer.

The XRD analysis presented in this thesis was conducted on a Bruker D8 diffractometer equipped with a Cu target X-ray tube and a diffracted beam monochromator. Data was collected over a 2θ angle ranging from 10° to 90° in 0.05° steps and counts were detected for 3 seconds per step. When the amount of sample was limited, a zero-background silicon sample holder (510 cut, available from the Gem Dugout, State College, Pa., USA) was used. This type pf sample holder allows for XRD analysis to be made on a small amount of sample spread thinly on a surface designed to produce no interference peaks to allow clean data of the sample to be collected.

The obtained XRD data was processed using a least squares refinement software which minimized the differences between measured and calculated Bragg peak positions. This type of analysis only requires the input of the Bragg peaks' corresponding crystal orientation (Miller indices) and their position on the 2θ axis. From this information the lattice constants of the material can be calculated.

3.4.4. Thermogravimetric analysis-mass spectrometry (TGA-MS)

Thermogravimetric analysis coupled with mass spectrometry, is a method to study the thermal decomposition of a material. A thermogravimetric analyzer is equipped with a precision balance and a programmable furnace. As the sample is heated over a specified range of temperatures, precise measurements of the mass are collected. When TGA is conducted under an inert gas flow, mass is typically lost due to gas evolution which occurs during the thermal decomposition of many materials. These evolved gases can then be ionized and separated according to their mass-to-charge ratio by a mass spectrometer for identification. Therefore, TGA-MS provides information about the temperatures at which gas evolution occurs in a material and identifies the elemental composition of these gases.

Thermal decomposition data in this thesis were obtained using a TA Instruments SDT Q600 coupled to a Discovery MS. The analysis was made under argon gas flow of 100 mL/min and always began with an argon purging period of 20 min. The samples were heated at a rate of 10ºC/min from room temperature to final temperatures of either 600ºC or 900ºC.

3.5. Solution characterization

3.5.1. Acid-base titration

Acid-base titration is a quantitative method to measure the concentration of an acid or a base by neutralizing it with a base or acid, respectively, of known concentration. According to the Arrhenius definitions, an acid is a substance that ionizes in water to produce H^+ and can therefore be characterized by its "power of hydrogen" (pH). For instance, HCl fully ionizes to produce H^+ and Cl^- in aqueous solution, therefore it is a strong acid. The relation between the concentration of H^+ and the pH of a solution is given by Equation [3.3]. It is worth mentioning that relating acidity to $[H^+]$ is convenient, but it is not accurate as free protons cannot exist in water. H^+ in aqueous solution will inevitably bond to water molecules and form hydronium ions (H_3O^+).

$$pH = -log_{10}([H^+]) \qquad [3.3]$$

A base is a substance that produces OH^- when ionized in water and can be characterized by its "power of hydroxide" (pOH). The relation between the concentration of OH^- and the pOH of a solution is given by Equation [3.4].

$$pOH = -log_{10}([OH^-]) \qquad [3.4]$$

A neutral solution is one where the concentrations of H^+ and OH^- are equal. For example, when pure water autoionizes, it can only form equal amounts of H^+ and OH^- ions. This is defined by a pH value of 7 and, simultaneously, a pOH value of 7 as well. For any aqueous solution at 25 ºC, the relationship between pH and pOH is always defined by Equation [3.5].

$$pH + pOH = 14 \qquad\qquad [\,3.5\,]$$

The Brønsted-Lowry theory further develops Arrhenius's definition by describing an acid as a proton donor and a base as a proton acceptor. By this theory, a base does not need to contain hydroxide; it can be a substance which generates hydroxide during hydrolysis. For example, Li_2CO_3 is a base because carbonate is the conjugate base of a weak acid, which means it will strongly attract protons and leave hydroxides during hydrolysis (see Equation [3.6]).

$$Li_2CO_{3(s)} + H_2O_{(aq)} \rightarrow 2Li^+{}_{(aq)} + OH^-{}_{(aq)} + HCO_3^-{}_{(aq)} \qquad [\,3.6\,]$$
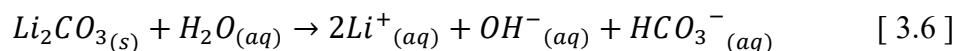
In acid-base titration, the concentration of a basic solution, for instance, is measured by slowly adding an acid of known concentration (the titrant) while monitoring the pH. When only a small amount of titrant has been added, little change in the pH will occur as the solution will act as a buffer solution. When the titrant exceeds the buffer capacity, a sharp drop in pH will be observed. The mid-point of this dramatic drop in pH coincides with the equivalence point as shown in Figure 3.6. The equivalence point is the point at which the moles of OH^- equal the moles of H^+ added. This point does not necessarily occur at a pH value of 7 since during the neutralizing of the base a conjugate acid will be formed. Knowing the volume of titrant needed to reach the equivalence point allows one to calculate the concentration of the base in the initial solution. Titration curves provide useful information about a solution. They indicate if an acid/base is monoprotic or polyprotic (donor/acceptor of one proton or many proton) by displaying one or multiple equivalence points. In the presence of a mixture of acids or bases, the titration curve will be a superposition of the individual curves of the present acid/base species.
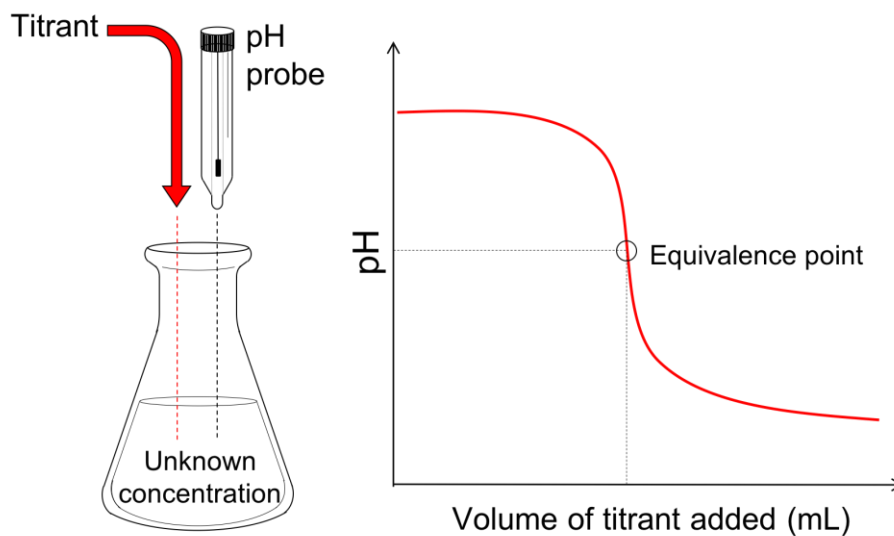
Figure 3.6. Acid-base titration procedure and titration curve example

In this thesis a Mettler Toledo G20 compact titrator was used. Solutions were always stirred for 1 min prior to titration and the solution remained under constant stirring throughout the titration process. Only basic solutions were analyzed by titration for this study, and the titrant used was a 0.05 M solution of HCl prepared with distilled deaerated water.

3.5.1. Inductively coupled plasma-optical emission spectrometry (ICP-OES)

Inductively coupled plasma coupled with optical emission spectrometry is a technique to identify the elemental composition of a solution or a material (which must be dissolved in solution) and the concentration of those elements at trace-levels. Figure 3.7 shows the main parts of an ICP-OES system and the pathway of the sample through the machine during analysis. First the sample is pumped through a nebulizer where it is transformed from liquid form to an aerosol and pushed into the aerosol chamber. Most of this aerosol is drained

while a small fraction is led into an argon plasma. The plasma is generated at the end of a quartz torch by a coil of high frequency alternating current; the resultant argon plasma reaches temperatures between 6000 and 7000 K. Under the conditions produced by the torch, the sample is atomized and ionized. When the excited atoms relax, their emission spectra are focused by a system of lenses and the component wavelengths are separated by diffraction. The signature emission spectra of the present elements are captured by a charged couple device (CCD) which allows for the identification of the elements, while the intensity of the emitted radiations indicate the corresponding concentrations of each element. However, to quantify these concentrations, calibration curves are required.
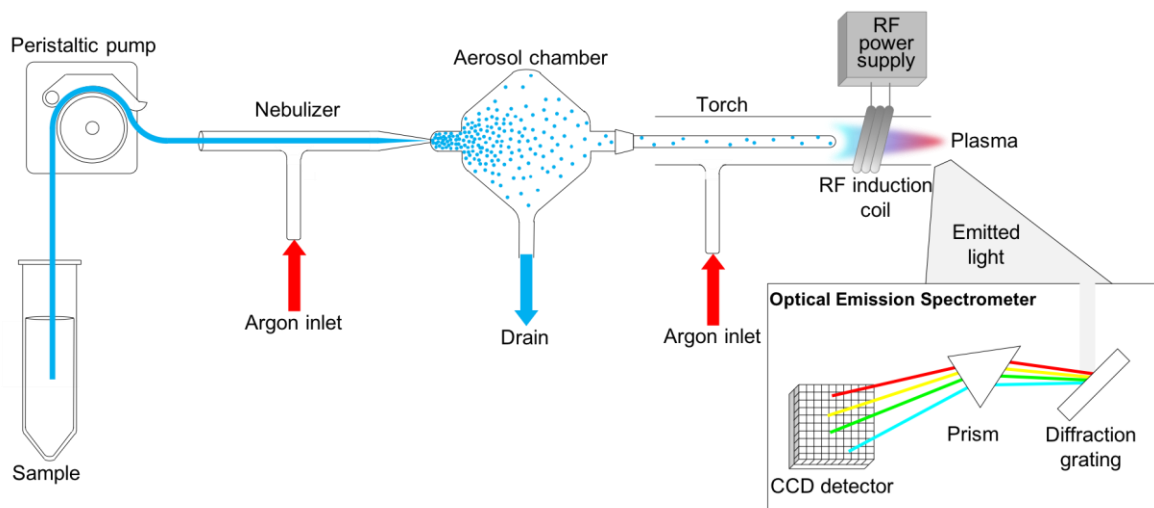
Figure 3.7. Schematic of the working principle of ICP-OES.

For this work a a Perkin Elmer Optima 8000 ICP-OES Spectrometer (Department of Dentistry, Dalhousie University) was used for analyzing wash solutions. Solutions for calibration were made by carefully diluting commercial standard solutions of the metals expected to be present in the samples. For instance, when washing NCA for instance, Li,

Ni, Co and Al are the only metals expected to be present in the wash solution. The calibration solutions used included a "blank", which consisted of a 2% HNO_3 solution in Nanopure water. The two other calibration solutions were made by diluting commercial standards with 2% HNO_3 solution made with Nanopure water as well. Table 3.1 shows the components of each calibration solution and their corresponding concentrations. The dilution of the samples should aim for concentrations within the calibration curves to ensure that the measured concentration is within the detection limit of the ICP-OES and to reduce the error on the collected data.

Table 3.1. Concentrations (in µg/mL) of each element in the three calibration solutions used for ICP-OES analysis.

Elements	Calibration solution 1 (Blank)	Calibration solution 2	Calibration solution 3
Li	0	0.5	1
Al	0	0.5	1
Ni	0	1	2
Mn	0	1	2
Co	0	1	2

CHAPTER 4. Effects of washing Ni-rich positive electrode materials

To improve or to find alternatives to the industrial process of washing Ni-rich positive electrode materials, a better understanding of the reaction between these materials and aqueous solutions is needed. The characterization of the washing solutions and the materials after washing have led to the proposition of two pH-dependent reaction mechanisms in occurrence when Ni-rich positive electrode materials are exposed to aqueous solutions. Further characterization was made to validate the proposed mechanisms.

4.1. Washing in distilled water

Acid-base titration has proven to be of utmost importance when studying the washing of Ni-rich materials as it allows one to identify and quantify the species that are removed from the material surface and found in solution. Water soluble $LiOH \cdot H_2O$ and Li_2CO_3 are the main surface impurities that are washed, and their presence explain the rise in pH observed in the washing solution. LiOH is a monoprotic base and displays one equivalence point when titrated with an acid. Li_2CO_3 is a diprotic base and can be distinguished from LiOH by its double equivalence points as shown in Figure 4.1.
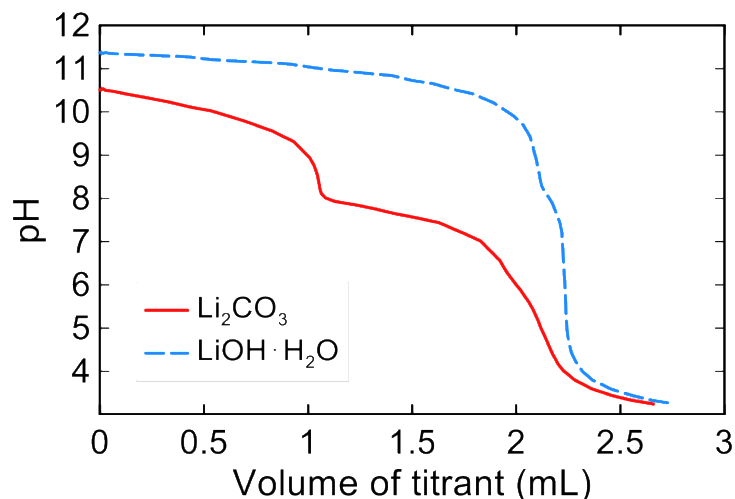
Figure 4.1. Titration curve for solutions of 1.0 x 10^{-4} moles of LiOH·H_2O and 5.0 x 10^{-5} moles of Li_2CO_3 dissolved in water with 0.05 M HCl as the titrant.

When a solution where both bases are present is titrated, the resulting titration curve is a superposition of the titration curves of the individual species. A more careful look at Figure 4.1 shows that the titration curve for LiOH·H_2O has two close equivalence points instead of the expected single equivalence point. This is due to the presence of a small amount of Li_2CO_3 in the LiOH·H_2O solution. LiOH reacts readily with CO_2 to form Li_2CO_3 as per Equation [4.1].

$$LiOH + CO_2 \rightarrow Li_2CO_3 + H_2O \qquad\qquad [\,4.1\,]$$

The conversion of LiOH to Li_2CO_3 emphasizes the importance of minimizing CO_2 exposure of the washing solution before and after the washing period. After stirring the four studied Ni-rich materials in water for periods ranging from 15 min to 48 h, the recovered aqueous solution was titrated, and the resultant titration curves are shown in Figure 4.2. These titration curves show that the amount of Li_2CO_3 in solution was minimal

and constant with increasing stirring durations which indicates efficient exclusion of CO_2 during the washing experiment. They also show that the solutions contain mostly LiOH and the LiOH concentration increased continually with stirring time which explains the continually rising pH values. The Li ions in solution originate from one of two main sources—residual lithium compounds formed on the particle's surface during synthesis or a Li which was deintercalated from the material's crystal lattice during water exposure. Figure 4.3 shows the change in pH value of the solution over a washing period of 24 h in deaerated distilled water. The rise in pH is steepest during the first minutes of water exposure. The pH continues to rise as more Li ions are deintercalated and more LiOH is produced but the reaction rate decreases over the washing period.

The loss of Li ions from the material infers the migration of a cation from the solution into the crystal material to maintain electrical neutrality. This is an indication that the Li^+/H^+ ion exchange mechanism that has been suggested by authors before,[59, 60] is likely to occur during water exposure. Further analysis will be done to validate this suggestion.

Figure 4.2 and Figure 4.3 show materials with higher Ni-content have higher rates of reaction with water. LNO, whose transition metal layer is fully occupied with Ni atoms, shows the highest rate of LiOH production when stirred in water. NCA, whose Ni-content is reduced to 83%, shows a significant improvement in resilience to Li deintercalation in water. NMC532 PC contains 50% Ni, and despite having equal specific surface area as NCA, shows less LiOH production; this indicates that Ni content is a more dominating factor in terms of water reactivity than surface area. Morphology also affects the rate of

reaction with water. NMC532 SC, which is in fact the material with the highest specific

surface area, shows the least amount of LiOH production when exposed to water.
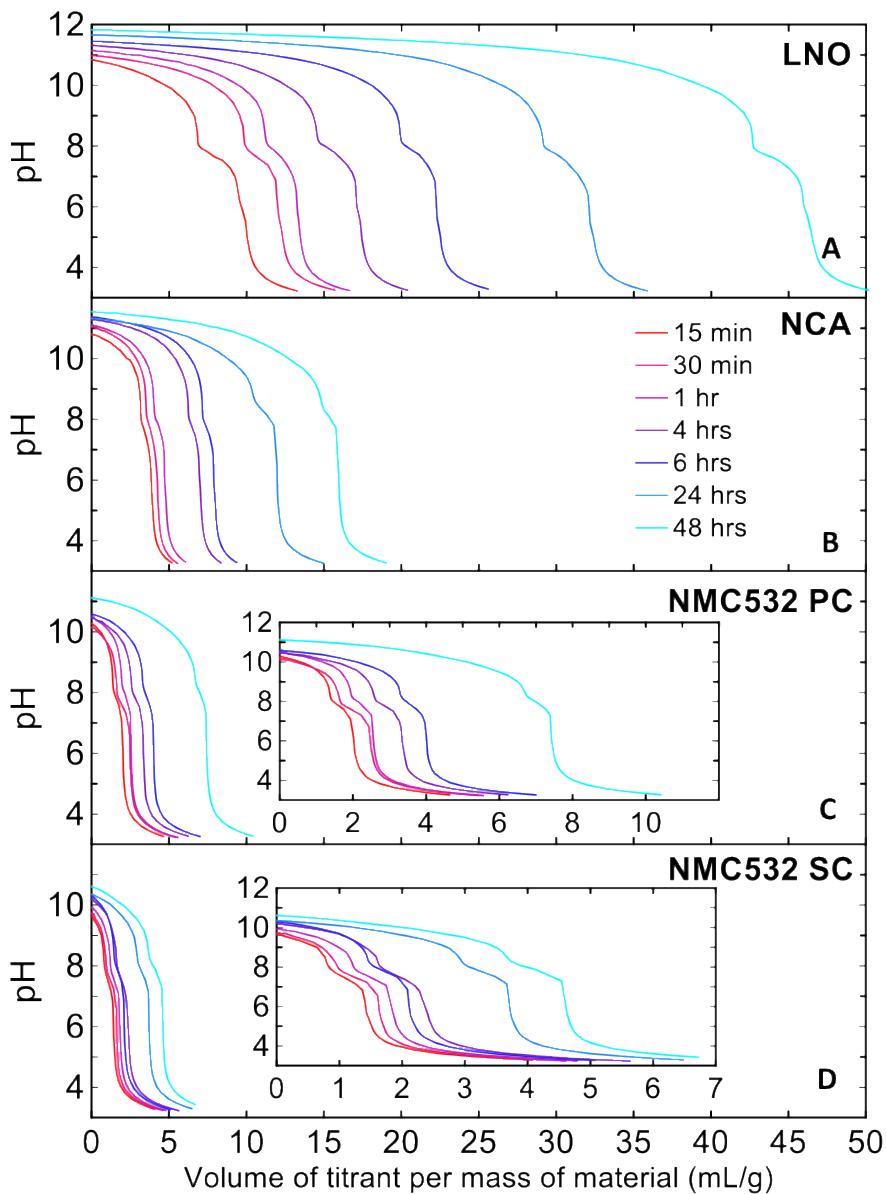
Figure 4.2. Titration curves for LNO (A), NCA (B), NMC532 PC (C), NMC532 SC (D) with 0.5 g of cathode material powder in 100 mL of deaerated distilled water using 0.05 M HCl as titrant.
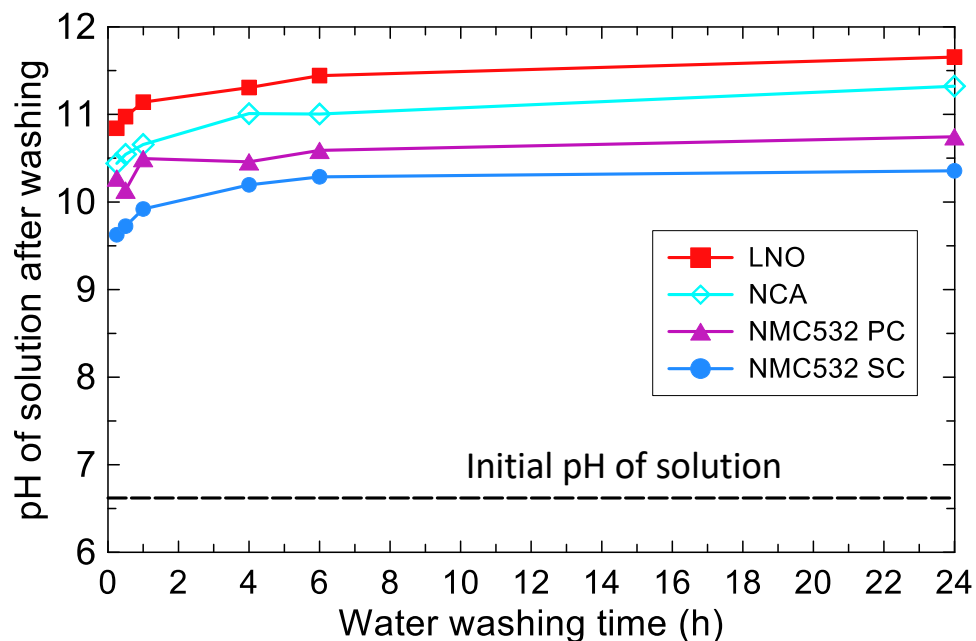
Figure 4.3. pH of the washing solution after stirring in deaerated distilled water compared to the measured initial pH of the wash solution.

4.2. Washing in acid

The same washing experiments were then made with an aqueous solution of dilute HCl instead of water. Washing the materials with acid was of interest to explore whether Li^+/H^+ ion exchange would be promoted with a higher concentration of H^+ in solution. A concentration of 0.05 M was chosen for the HCl solution because when used to wash the materials, no visible signs of significant material dissolution were observed. Figure 4.4 shows the pH of the wash solution after stirring NCA in acid over a period of 6 h. Different concentrations of acid and different volumes of solutions corresponding to different H^+ to Li^+ ratios in the stirred mixture were tested. As can be seen in Figure 4.4 A, when washing NCA with an HCl solution of 0.1 M, the solution becomes more and more visibly green with higher stirring duration. The green colour indicates the presence of Ni^{2+} in solution; a

56

solution of 1 M of Ni^{2+} is shown for reference. The objective of acid exposure experiments was to observe the effect of Li^+/H^+ ion exchange and not to dissolve the material. Therefore, a solution of 0.05 M of HCl was used for all subsequent acid washing tests.
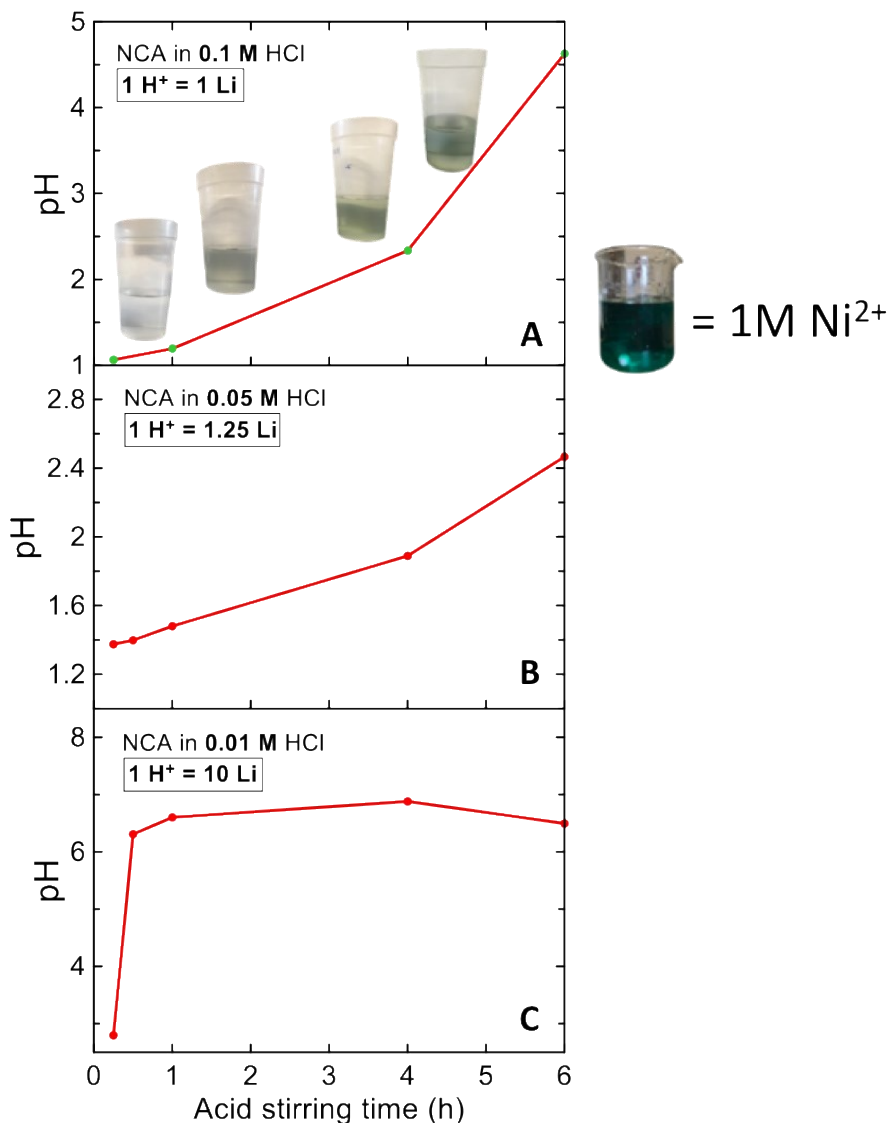
Figure 4.4. pH of washing solution after stirring NCA in a solution of HCl acid at concentrations (A) 0.1 M which corresponding to 1 mol H+ in solution to 1 mol of Li in the material, (B) 0.05 M, corresponding to 1 mol H+ in solution to 1.25 mol of Li in the material, and (C) 0.01 M, corresponding to 1 mol H+ in solution per 10 mol of Li in the material. Panel A shows the visible change in the solution overtime (1 M solution of Ni is shown for visual reference). Solutions represented in panels B and C remained clear.

Figure 4.5 shows the pH of the acidic wash solution after stirring the four materials in the solution for durations up to 6 h. As with the water exposure tests, a rise in pH was observed after washing. It is important to note that the pH scale is a logarithmic scale and that the change in pH after acid washing seen in Figure 4.5 indicates a higher rate of reaction than the water washing results seen in Figure 4.4.
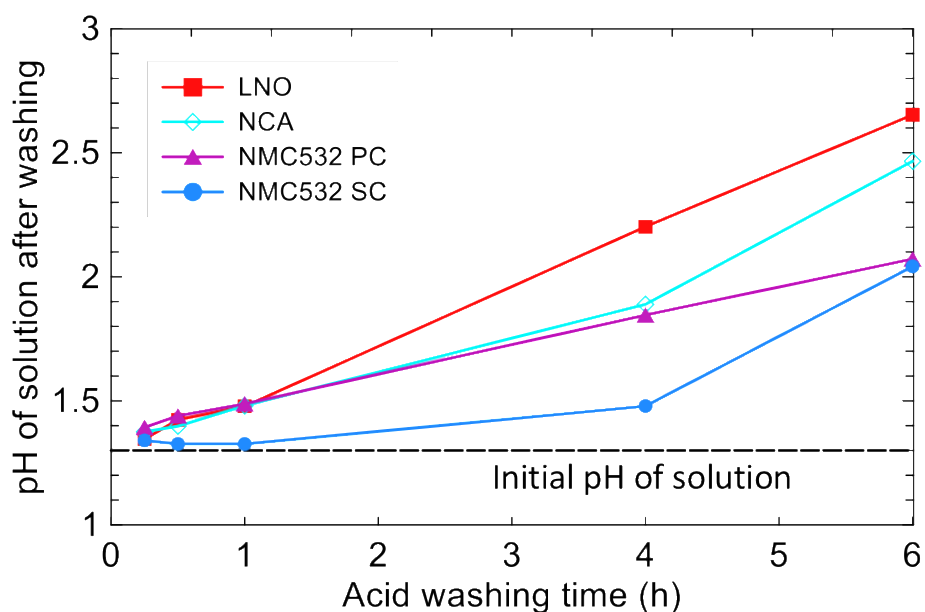
Figure 4.5. pH of the washing solution after stirring in a 0.05 M of HCl compared to the measured initial pH of the wash solution.

To further analyse the different changes to the materials after washing the materials in water or in acid, SEM images of each material were captured of the material in its pristine state, after 48 h of stirring in water and after 6 h of stirring in acid. This SEM images allow to observe any morphological changes to the material after washing. For materials washed with water, SEM images were captured after 48 h of stirring to clearly observe the effect

of water exposure. In the case of acid washing, SEM images were captured after only 6 h of washing since the effect of acid exposure is more aggressive and clear observations could be made after a shorter washing duration.

Figure 4.6 B shows that the surface of LNO secondary particles after stirring in water differs from the smooth and clean surface of a pristine LNO particle. However, the effect of water washing on the particles' surface is not as dramatic as that of acid washing; Figure 4.6 C shows the formation of gaps between the primary particles following acid exposure. The difference in the particle surfaces after water and acid washing points to the occurrence of two different reactions.
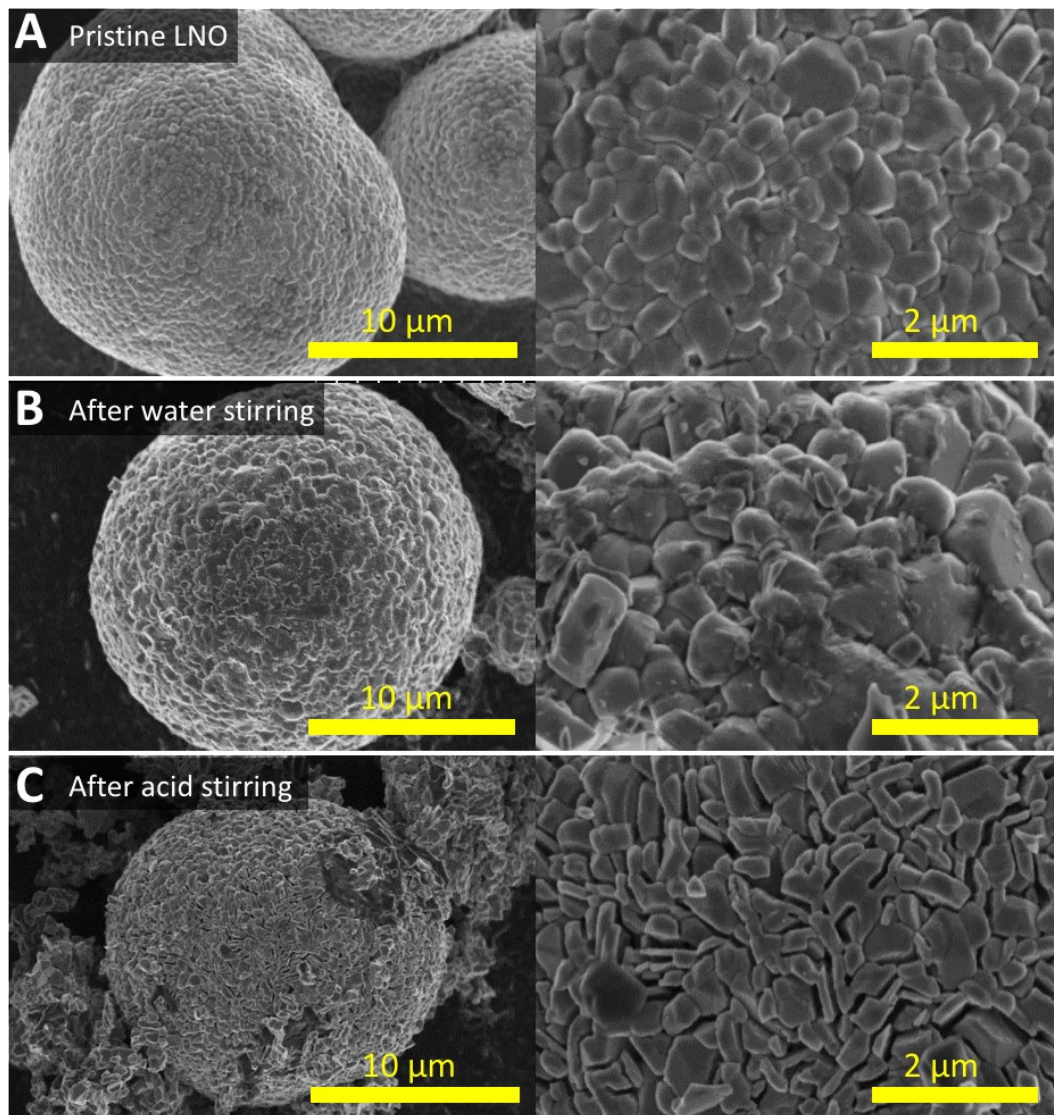
Figure 4.6. SEM images of secondary particles for pristine LNO (A), LNO after stirring in water for 48 h (B), and LNO after stirring in a 0.05 M HCl solution for 6 h (C) at different magnifications.

Figure 4.7 shows that NMC532 PC is similarly affected by water and acid washing as LNO.

Figure 4.7 B shows a more rugged surface of the secondary particles after stirring in water, and Figure 4.7 B also shows the formation of gaps between the primary particles of the material.
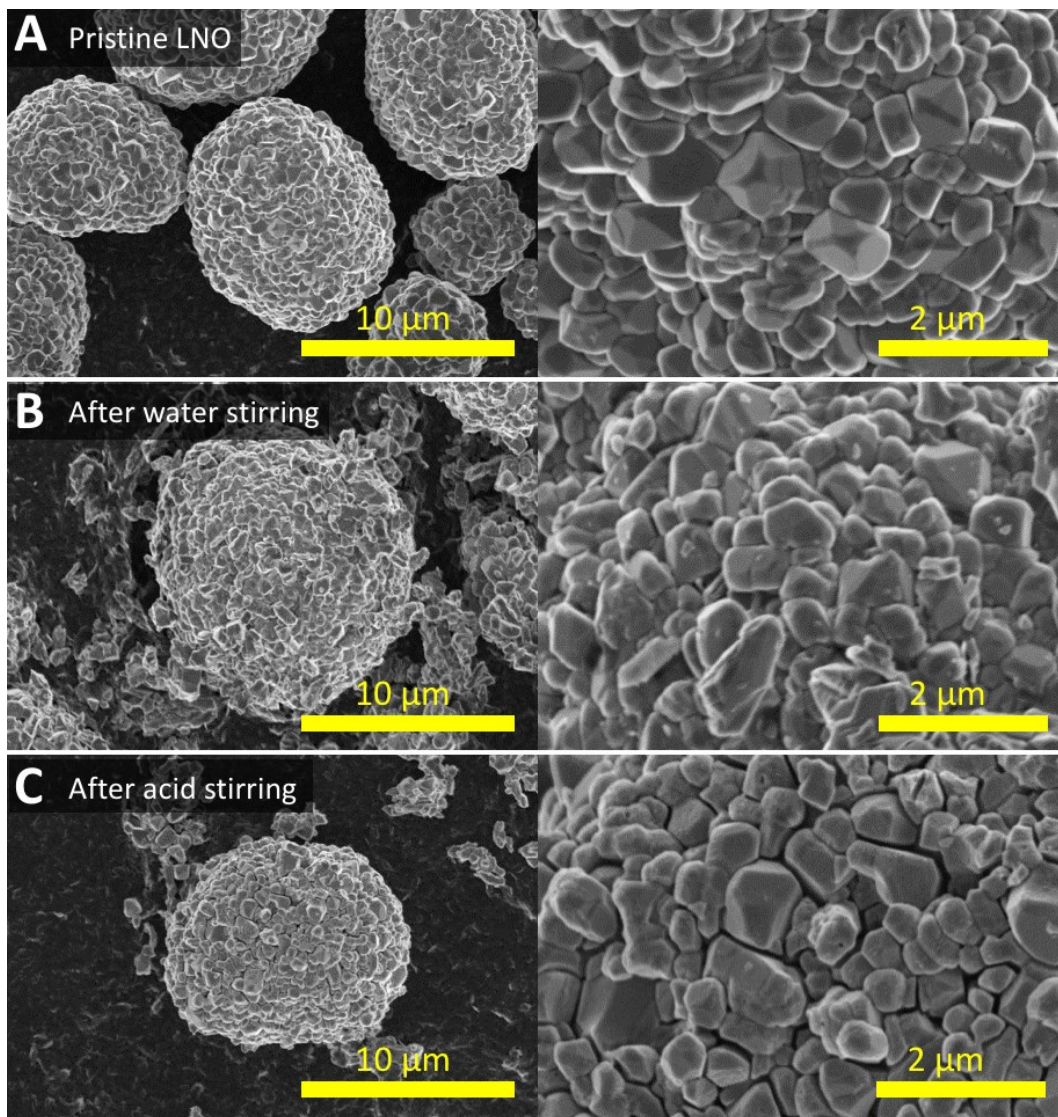
Figure 4.7. SEM images of secondary particles for pristine NMC532 PC (A), after stirring in water for 48 h (B), and after stirring in a 0.05 M HCl solution for 6 h (C) at different magnifications.

Figure 4.8 shows that a single crystalline material such as NMC532 SC is more resilient to structural changes during water and acid exposure. Figure 4.8 B shows only minor changes in the structure of NMC532 SC as opposed to its polycrystalline counterpart. In Figure 4.8 C some dissolution and breaking of the single crystals can be observed in the most severely

affected particles, but generally the single crystals appear to maintain structural integrity after acid exposure. These SEM images seen in Figures 4.6-4.8 are evidence that the materials react differently when exposed to water or to acid. However, they cannot provide details of the reaction mechanisms in occurrence; further characterization of the materials physical properties after washing will be necessary.
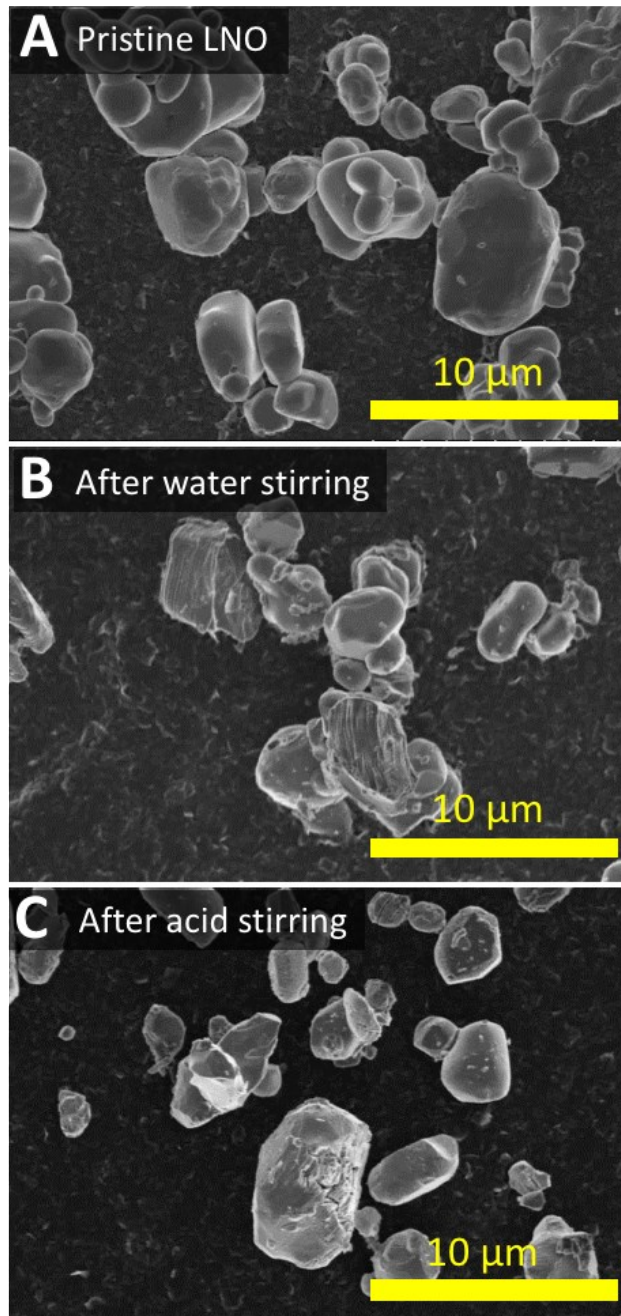
Figure 4.8. SEM images of secondary particles for pristine NMC532 SC (A), after stirring in water for 48 h (B), and after stirring in a 0.05 M HCl solution for 6 h (C) at a X5000 magnification.

4.3. Two pH-dependent regimes hypothesis

The data collected from titration and SEM imaging suggest that the reaction between the materials and the aqueous solution used for washing depend on the pH of the solution. Two pH-dependent regimes have been suggested to describe the reactions:

1. The Li^+/H^+ ion exchange regime

   This ion exchange mechanism seems to occur when materials are exposed to aqueous solutions of high pH value. It involves the delithiation of the material (Li ion migrate outwards) and a migration of H^+ inwards to fill the vacant Li^+ site and maintain electrical neutrality. Equation [4.2], where M represents any metal or combination of metals, describes the Li^+/H^+ ion exchange formula.

$$LiMO_{2\,(s)} + xH_2O_{(l)} \longrightarrow Li_{1-x}H_xMO_{2\,(s)} + xLiOH_{(aq)} \qquad [\,4.2\,]$$
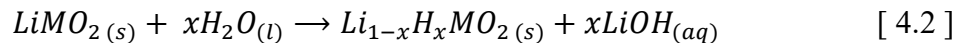
2. The delithiation-dissolution regime

   The delithiation-dissolution regime occurs during washing with aqueous solutions of lower pH value. In this regime, the material is delithiated but little or no H^+ is introduced in the crystal lattice. Instead, charge neutrality of the material is maintained by a partial dissolution of the material. Equation [4.3] describes the delithiation-dissolution reaction. This reaction shows that the delithiation rate is twice that of the metal dissolution rate giving this reaction a signature 2:1 mole ratio of Li removed from the material to metal dissolved. This mechanism was proposed in 1981 by Hunter[78] to

explain the acid treatment of spinel LiMn$_2$O$_4$, but it is suspected to be manifested in the washing of layered LTMOs with dilute acid as well.

$$(1 + x)LiMO_2 + 4xH^+ \rightarrow Li_{1-x}MO_2 + 2xLi^+ + xM^{2+} + 2xH_2O \qquad [\,4.3\,]$$
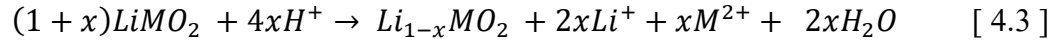
The removal of H$^+$ from solution and the consequent production of LiOH shown in Equation [4.2] is responsible for the rise in pH during Li$^+$/H$^+$ ion exchange regime. Equation [4.2] also describes the relation between the LiOH concentration after washing and the amount of Li removed from the material. Figure 4.9 A shows the percentage of Li removed from the material and found in solution; this percentage was calculated from the change in pH of the wash solution assuming a Li$^+$/H$^+$ ion exchange reaction. However, when the material was washed with a dilute solution of HCl, the same calculation method was no longer a sensible choice to quantify the Li loss (percentage above 100% would be obtained for long duration experiments). This shows that when washing with acid, the Li$^+$/H$^+$ ion exchange reaction cannot be assumed. Figure 4.9 B shows the percentage of Li lost from the material and found in solution calculated from the change in pH observed after stirring in dilute acid and assuming that the reaction is in accordance to Equation [4.3].
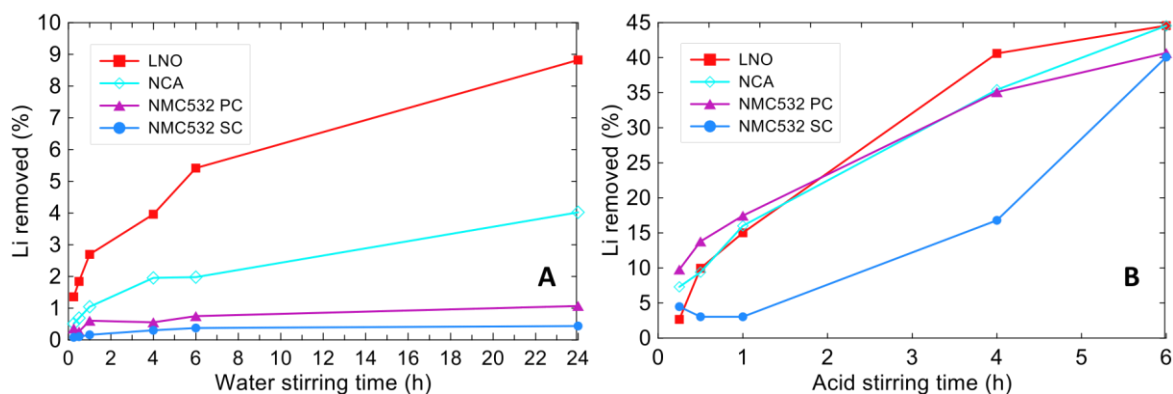
Figure 4.9. Percentage of the original Li content in the material that was found in solution after stirring in water calculated from the pH increase of the solution using the hypothesized Equation [4.2] (A) Percentage of the original Li content in the material that was found in solution after stirring in dilute acid calculated from the pH increase of the solution using the hypothesized Equation [4.3] (B)

Both proposed reactions explain the rise in pH observed after water and acid washing and imply that the resultant material will be delithiated in both cases. The acid-base titration data and SEM images collected support the hypothesis of the two pH-dependent regimes but are not conclusive evidence. Further characterization of the aqueous solutions and the recovered material was performed to validate this hypothesis.

ICP-OES analysis was used to analyse the elemental composition of the solutions after washing. This method can be used to verify that dissolution occurs in the delithiation-dissolution regime, while little to no dissolution occurs when in the Li^+/H^+ ion exchange regime as expected. Additionally, TGA-MS was conducted to verify that H^+ insertion in the material occurred in the Li^+/H^+ ion exchange regime, while no H^+ insertion occurs in the delithiation-dissolution regime. XRD analysis was also performed to validate the expected deliathiation of the material.

4.4. Validation of the two pH-dependent regimes

First, the solution collected after water washing was quantitatively analyzed to measure the amount of metals in solution. Figure 4.10 shows the percentage of Li removed from the material calculated from pH measurements compared to the percentage of transition metals removed from the material after stirring in water. ICP-OES was used to measure the transition metals as they were only present at trace-levels.
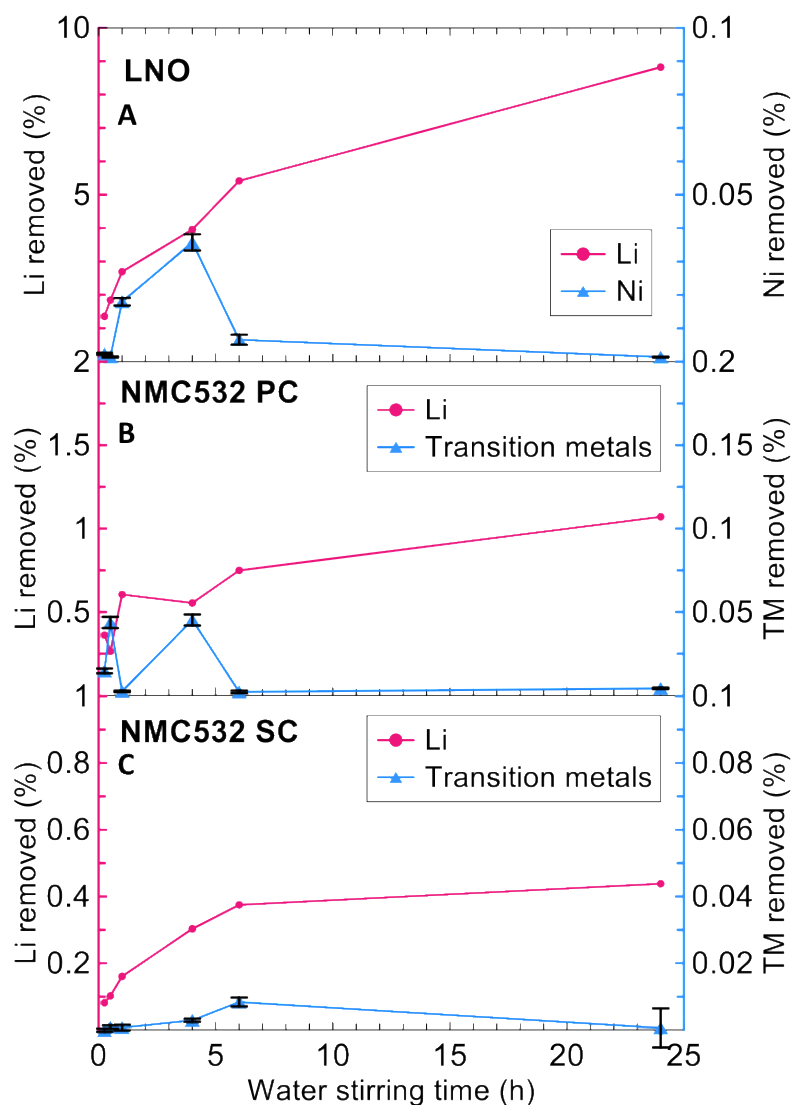
Figure 4.10. Percentage of Li and transition metals found in aqueous solution, obtained from pH measurements and ICP-OEM measurements respectively, after stirring LNO (A), NMC532 PC (B) and NMC532 SC (C) in water. N.B. The y-axes vary in scale.

Figure 4.10 A shows that when LNO is stirred in water, the percentage of Li removed from the material is more than two order of magnitude higher than the percentage of Ni dissolved. When stirring NMC532 PC and NMC532 SC show a similar disparity between the amounts of Li and the amount of transition metals found in solution. Figure 4.10 A and Figure 4.10 B show the difference between the percentage of Li lost from the material and the percentage of transition metals dissolved. The percentage of removed transition metals shown in Figure 4.10 were calculated from the sum of the amount of Co, Ni and Mn found in solution. The ICP-OES results indicate that very little dissolution of the material occurs when washing in water in contrast to the significant amount of delithiation; this is in accordance with the Li^+/H^+ exchange equation (Equation [4.2]).

The solution collected after acid washing were also quantitatively analyzed by ICP-OES. After stirring in acid, the concentrations of transition metals found in the solution were not at trace-levels. Figure 4.11 A1 shows the percentage of Li removed and the percentage of Ni dissolved from the material are within the same order of magnitude. Figure 4.11 A2 shows the specific mole ratio of Li to Ni found in solution. This ratio is higher than 2 for short washing periods but converges towards a value of 2 with increased stirring time. Figure 4.11 B1 and Figure 4.11 B2 show a similar phenomenon for NMC532 PC stirred in acid with a clear Li:Ni value of 2. The solutions used for washing NMC532 SC show a different progression curve for the percentage of Li and transition metals removed from the single crystals as opposed to the polycrystalline materials as shown in Figure 4.11 C1. Nevertheless, Figure 4.11 C2 shows the same Li:TM ratio of 2 in the case of NMC532 SC.

The rate of Li delithiation to the rate of metal dissolution observed after acid washing are in accordance to the proposed delithiation-dissolution regime (Equation [4.3]).
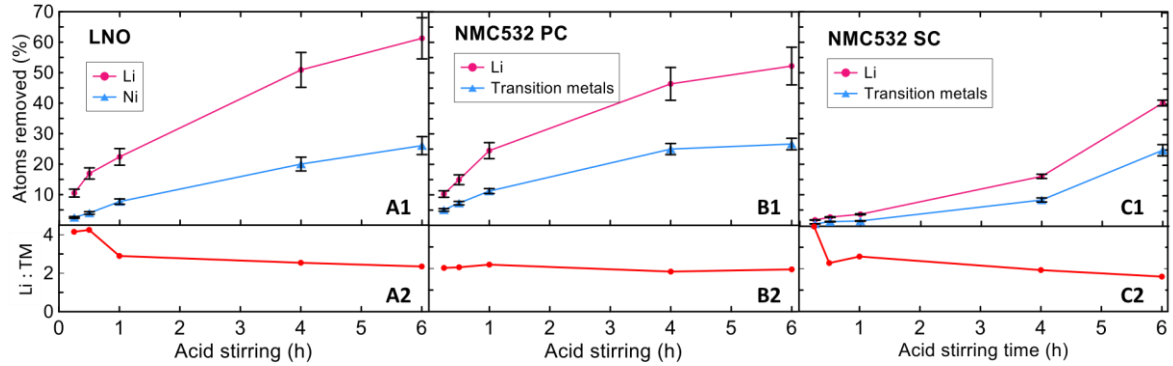
Figure 4.11. Percentage of Li and transition metals removed from the material and found in solution, obtained from ICP-OEM measurements, after stirring LNO (A1), NMC532 PC (B1) and NMC532 SC (C1) in a solution of 0.05 M HCl. The molar ratio of Li to transition metals measured in solution for LNO (A2), NMC532 PC (B2) and NMC532 SC (C2).

As was done in the case of water washing, the percentage of transition metals dissolved after acid washing shown in Figure 4.11 are the sum of all three metals found in the transition metal layer. Figure 4.12 shows the individual dissolution percentages of Co, Ni and Mn and shows that Mn has the least affinity to dissolve during acid exposure while Co has the highest dissolution rate.
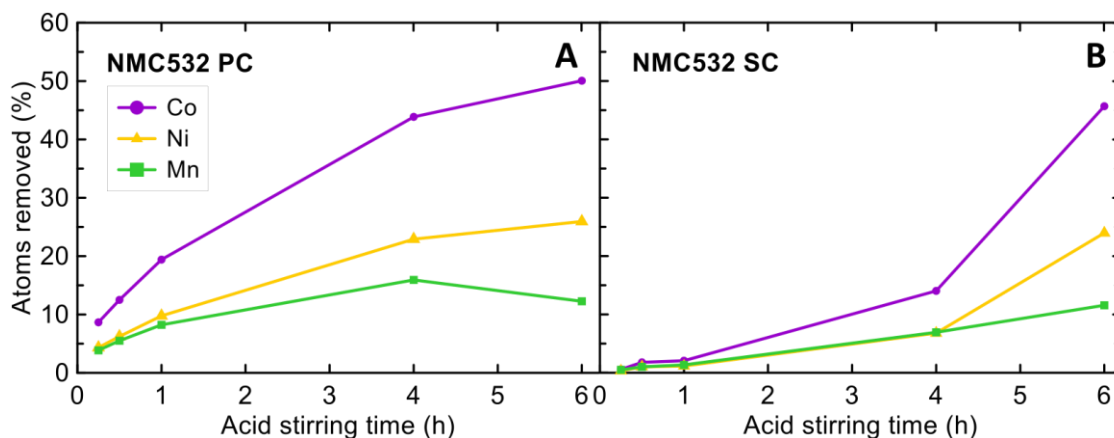
Figure 4.12. Percentage of transition metals dissolved individually from NMC532 PC (A) and NMC532 SC (B) after stirring in a 0.05 M of HCl.

The characterization of the aqueous solutions following the washing of the tested materials confirms the significant dissolution of the material at low pH and the lack of significant dissolution occurring at high pH. To further validate the proposed mechanisms, the insertion of H$^+$ in the material's crystal lattice should be observed at high pH and not at low pH washings. The recovered material after washing is expected to be delithiated and to contain H$^+$ ($Li_{1-x}H_xMO_2$). This resultant material should release water during thermal decomposition due to the presence of H$^+$ as per Equation [4.4].

$$Li_{1-x}H_xMO_{2\,(s)} \rightarrow Li_{1-x}MO_{2-x\,(s)} + \frac{x}{2}H_2O_{(g)} + \frac{x}{4}O_{2\,(g)} \qquad [\,4.4\,]$$
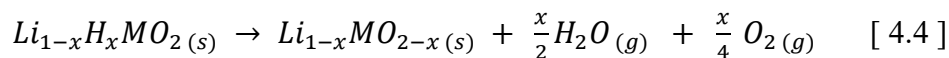
Figure 4.13 shows the data obtained from TGA-MS when heating the recovered materials to 600ºC after stirring in water for 24 h. Figure 4.13 A1 shows the mass loss of the LNO sample throughout its thermal decomposition. Figure 4.13 A2 shows that the decomposition of LNO occurs mainly in two distinct steps beginning around 200ºC and 250ºC. The MS data shown in Figure 4.13 A3, clearly indicates that the first mass loss step

is due to the release of H_2O while the second step corresponds to a smaller release of O_2. The evolution of H_2O seen in washed LNO is evidence of Li^+/H^+ ion exchange. Furthermore, LNO displays a largest amount of water release when compared to NMC532, which indicates that it has a higher propensity for Li^+/H^+ ion exchange. Figure 4.13 B1 and Figure 4.13 C1 show a smaller percentage of mass loss for NMC532 when compared to LNO. The first drop in mass was also seen around 200°C and was accompanied by the detection of water evolution as seen in Figure 4.13 B3 and Figure 4.13 C3.
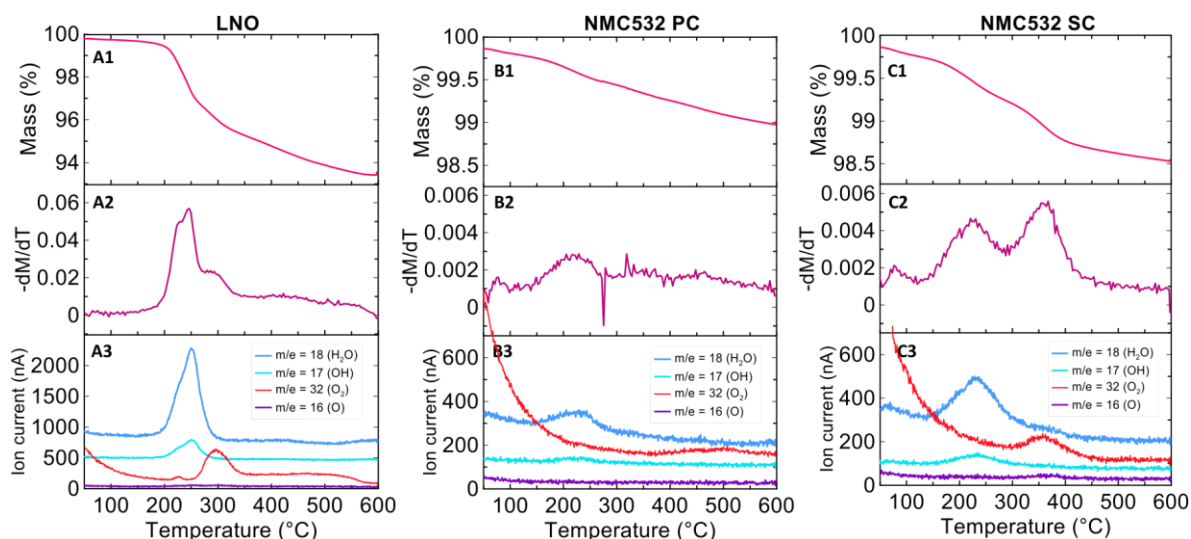
Figure 4.13. TGA-MS data for LNO (A), NMC532 PC (B) and NMC532 SC (C) after stirring in water for 24 h showing percent mass (M) versus temperature (T) (1), -dM/dT versus T (2) and the mass spectrometer ion current signal for 4 selected masses as indicated (3).

After washing the materials in acid, the recovered material, according to the delithiation dissolution regime proposed, is expected to be a delithiated material without any protons intercalated in the crystal lattice ($Li_{1-x}MO_2$). The thermal decomposition of such materials

do not involve any water evolution, only oxygen release should be observed as per Equation [4.5].[30]

$$Li_{1-x}MO_{2\ (s)} \quad \rightarrow \quad Li_{1-x}MO_{2-x\ (s)} \ + \frac{x}{2}O_{2\ (g)} \qquad\qquad [\ 4.5\ ]$$
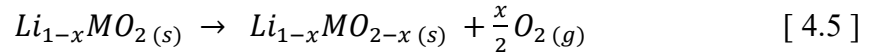
Figure 4.14 shows the results for the TGA-MS analysis of the materials washed in acid for 6 h. In the case of LNO, a sharp drop in mass is observed around 200°C due to the evolution of both water and oxygen as shown in Figure 4.14 A. The unexpected release of water from LNO could be caused by some Li^+/H^+ ion exchange occurring during the material's exposure to dilute acid since LNO has proven to be very prone to ion exchange. It is also possible that ion exchange could have occurred after the stirring period when the LNO samples were left to dry at low temperature (70°C). However, Figure 4.14 A1 shows that the mass was lost predominantly after 250°C due to oxygen evolution only. The thermal decomposition of LNO after acid washing also show a two-step decomposition process at 250°C and 400°C. NMC532 PC and NMC532 SC showed minimal mass loss ($\leq 1\%$) before reaching a temperature of 250°C. The majority of the mass loss occurred at temperatures above 400°C due to the evolution of oxygen. This affirms that during acid washing, the materials are delithiated while little to no Li^+/H^+ ion exchange occurs.
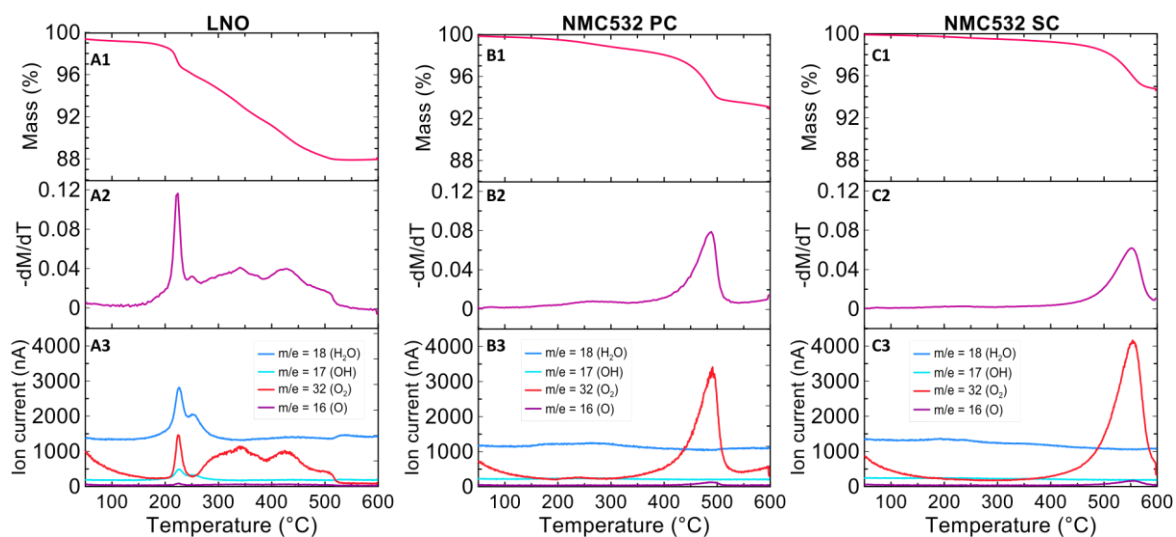
Figure 4.14. TGA-MS data for LNO (A), NMC532 PC (B) and NMC532 SC (C) after stirring in dilute acid for 6 h showing percent mass (M) versus temperature (T) (1), -dM/dT versus T (2) and the mass spectrometer ion current signal for 4 selected masses as indicated (3).

The delithiation of the materials whether it is due to acid or water washing would result in changes to the crystal lattices constants of the materials; these changes should be observed in the XRD profiles of the materials. Figure 4.15 shows the changes to the XRD profile of pristine LNO after the material has been washed in water for 24 h. Some peak-shifting and peak-splitting can be observed but no dramatic changes to the XRD profiles are seen. This is expected as the Li loss after 24 h of water washing has been calculated to be around 9% (see Figure 4.9 A).
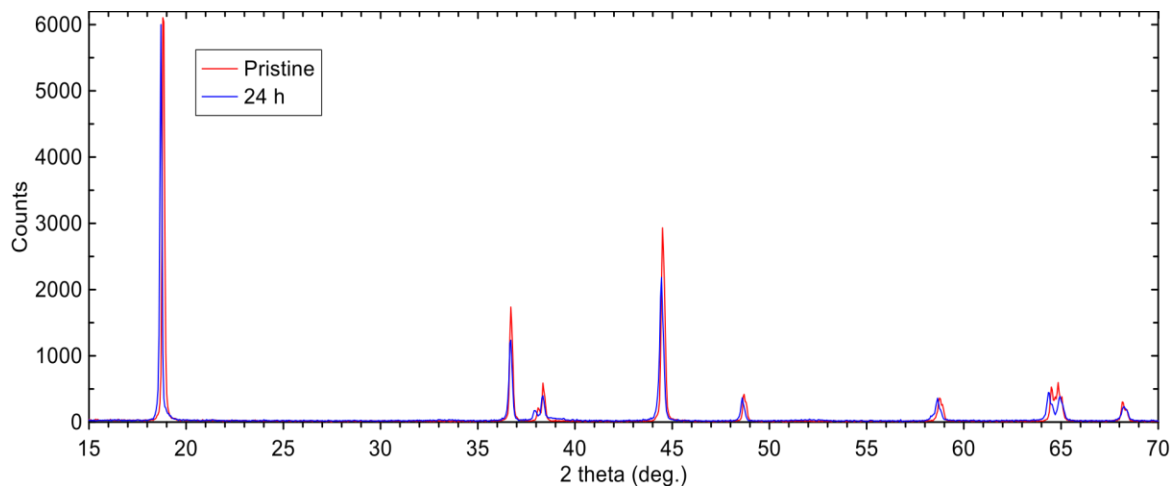
Figure 4.15. XRD profiles of LNO after stirring in water for 24 h compared to the XRD profile of pristine LNO.

Materials that were washed in acid, on the other hand, have been suggested to a significant amount of delithiation according to the large quantities of Li found in solution observed during titration analysis. The XRD profiles of the materials after different durations of acid washing shown in Figure 4.16 affirm a higher state of delithiation in these materials.
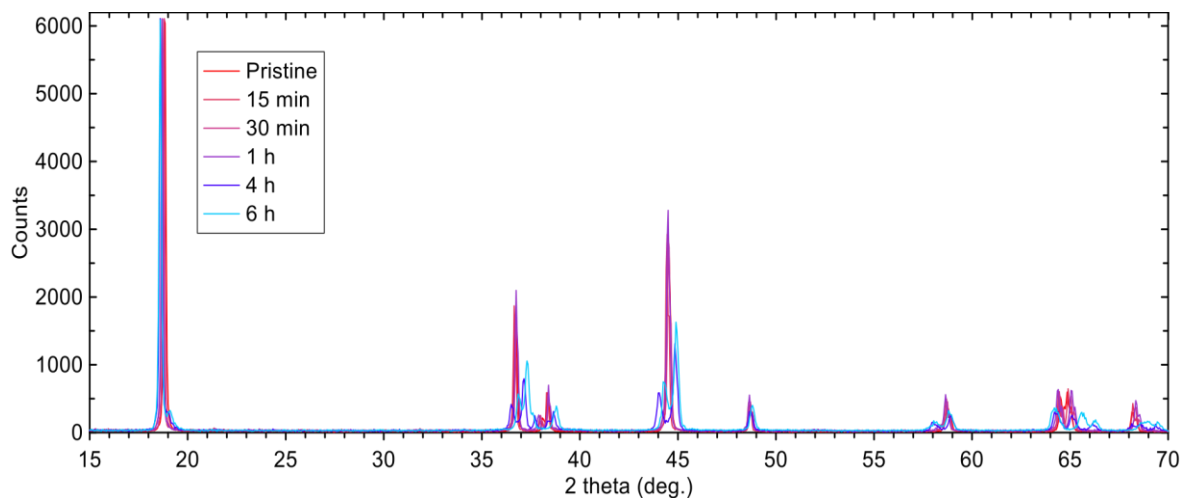
Figure 4.16. XRD profiles of LNO after stirring in a solution of 0.05 M of HCl for different time periods.

Important changes have been observed in the positions of Bragg peaks 101, 006, 012, 104, 018 and 110. Figure 4.17 focuses on these Bragg peaks and shows how they have shifted in comparison to the Bragg peaks positions for pristine materials. The 101 Bragg peaks (found in the scattering angle region 36º-39º) for LNO and NCA are shown in Figure 4.17 A and Figure 4.17 B respectively. There is a clear splitting of the 101 Bragg peak into 2 separate peaks for LNO and NCA. The 104 Bragg peaks (found in the scattering angle region 44º-45 º) for those two materials are also split in two. It is known that the lattice structure of LNO changes from a hexagonal phase to a monoclinic phase during charging of the material. This phase transition is aided by Li vacancies and begins at a delithiation state of around 20%.[79, 80] The splitting of the 101 and 104 Bragg peaks is a manifestation of the transition to the monoclinic phase. This splitting is seen in the case of LNO and NCA the state of delithiation of the materials must have been $\geq$ 20%. This is expected from these high Ni-containing materials as opposed to NMC532 which has lost less Li according to previously presented titration results (see Figure 4.9 B). Furthermore, monoclinic distortion is not a phenomenon that has been observed in NMC532 materials during charging.[38]

The Bragg peaks for both NMC532 PC and NMC532 SC, shown in Figure 4.17 C and Figure 4.17 D respectively, do not display clear splitting as with LNO and NCA, but they do show important peak shifting which signify a change in the materials' lattice parameters. It is worth noting that all XRD profiles have shown single phase materials. This means that the delithiation caused by water and acid washing affect the particle at the bulk level and not only at the surface and subsurface region.
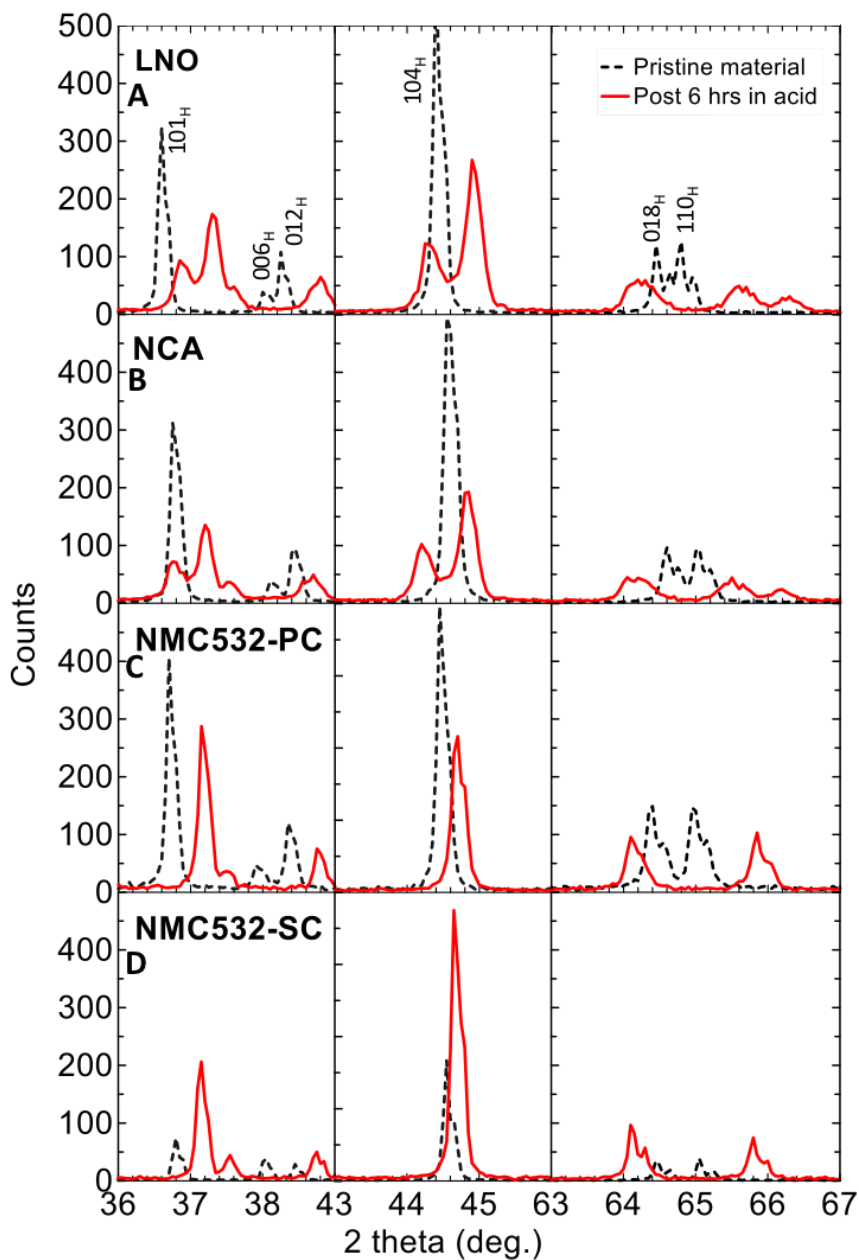
Figure 4.17. XRD results comparing LNO (A), NCA (B), NMC532-PC (C) and NMC532-SC (D) pristine samples and samples after stirring in 0.05 M HCl solution for 6 h.

Washing a positive electrode material results in delithiation is similarly (but not identical) to the delithiation which occurs in the positive electrode during the charging of a cell. The lattice parameters of the material's crystal structure should be the same at equal delithiation

states regardless of the delithiation process used. In-situ XRD analysis of a charging material provide information about the lattice parameters of the material at all delithiation states throughout the charging process. This charging data can then be compared to the lattice parameters obtained from XRD data of water and acid washed materials analyzed by least squares refinement. Validating the delithiation process that occurs at both regimes (the Li^+/H^+ ion exchange regime and the delithiation-dissolution regime) would further affirm the occurrence of the proposed mechanism.

In the Li^+/H^+ ion exchange regime, the amount of Li removed from the material and found in solution is the same amount of Li that is deintercalated from the material. However, in the delithiation-dissolution regime, the percentage of Li removed from the material and found in solution is the sum of the percentage of Li delithiated and the percentage of Li dissolved. Equation [4.6] expresses the relation between the fraction of delithiation of the remaining material, denoted as x, and the total fraction of Li found in solution, denoted as y.

$$x = \frac{y}{2-y} \qquad\qquad [\,4.6\,]$$

Equation [4.6] was used to calculate the expected state of delithiation of the materials so that their lattice parameters could be compared to those of charged materials. Figure 4.18 shows the agreement between the lattice parameters for LNO calculated after delithiation by charging, and the lattice parameters after delithiation by water exposure or by acid exposure. The delithiation values on the x-axis for the red (Δ) and blue (◊) series in Figure 4.18 were calculated from solution analysis and Equation [4.6]; the data points represent

from left to right the data corresponding to washing for 15 min, 30 min, 1 h, 4 h, 6 h and 24 h in that order. When compared to the lattice parameters from cell charging data[80] (gray series ○), the lattice parameters of the materials after water and acid washing show close values and similar trends. As discussed previously, LNO undergoes monoclinic distortion during delithiation. For this reason, the lattice parameters a and c associated to its hexagonal phase (Figure 4.18 A and Figure 4.18 B) are compared separately from the lattice parameters a, b and c corresponding to its monoclinic phase (Figure 4.18 C, Figure 4.18 D and Figure 4.18 E).
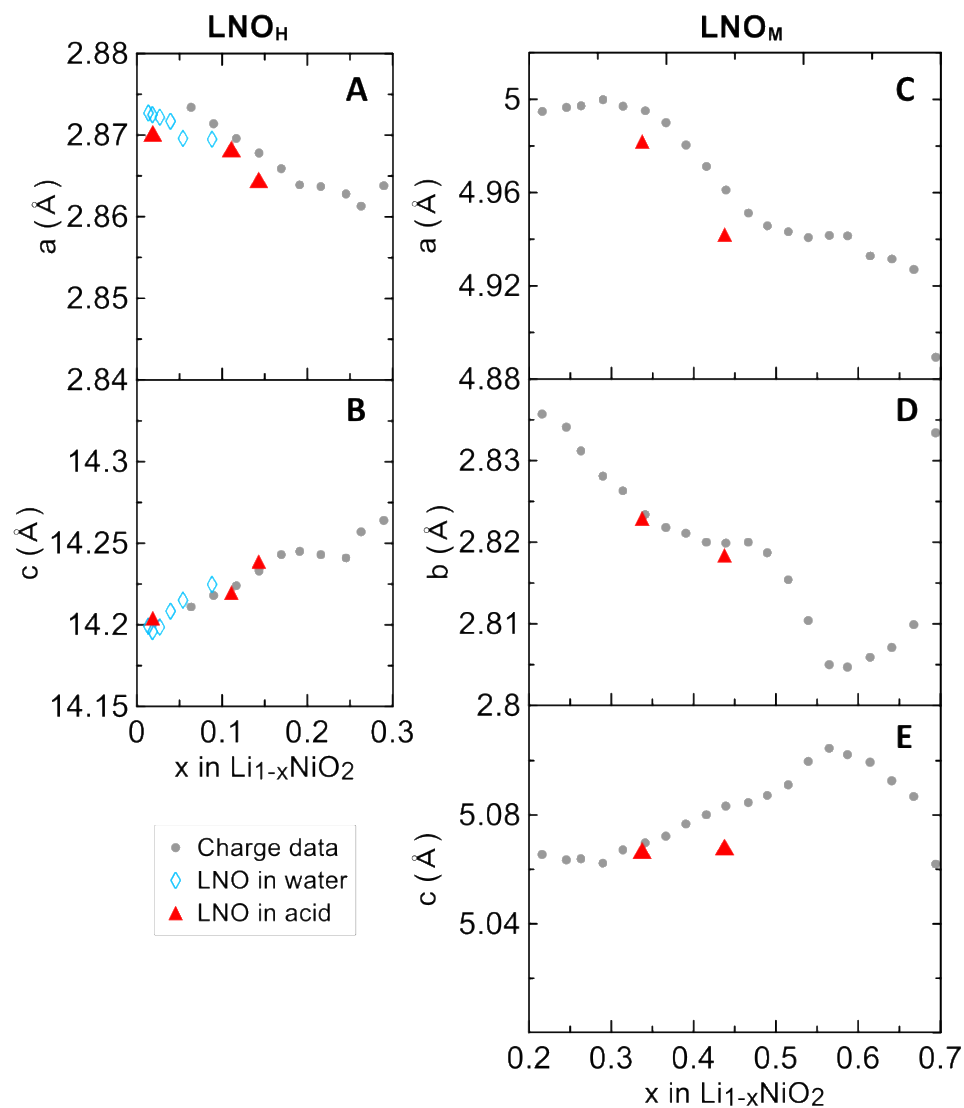
Figure 4.18. Comparison between the lattice parameters, a (A) and c (B) of $Li_{1-x}NiO_2$ in the hexagonal phase (LNO_H) during charge[80] and during water or acid stirring. Comparison between the lattice parameters, a (C), b (D) and c (E) of $Li_{1-x}NiO_2$ in the monoclinic phase (LNO_M) during charge and during acid stirring. The fraction of Li removed (x) used to plot the lattice parameters after water and acid exposure was determined from ICP data and Equation [4.6].

NMC532 remains in its hexagonal phase throughout delithiation, therefore, only hexagonal phase lattice parameters a and c were compared to charging data. Figure 4.19 shows that the delithiation of NMC532 during water washing (blue (◊) series) is minimal and difficult

to evaluate in terms of lattice parameters change. However, the changes in a and c values during acid exposure are considerable and follow the same approximate values and trends as the changes observed during charging.
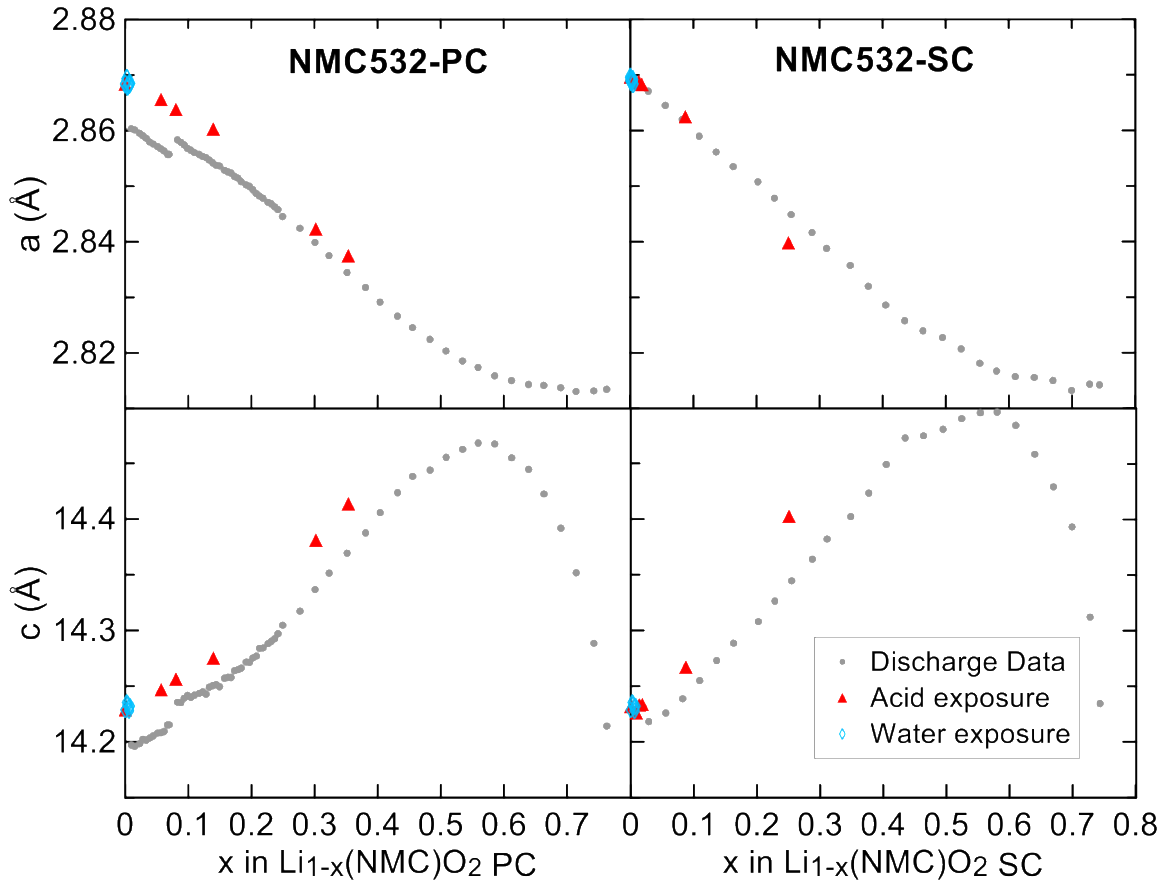
Figure 4.19. Comparison between the lattice parameters a (A) and c (B) in the hexagonal phase of polycrystalline NMC532 during charge[81] and during acid or water exposure. Comparison between the lattice parameters a (C) and c (D) in the hexagonal phase of single crystal NMC532 during charge[81] and during acid or water exposure. The fraction of Li removed (x) used to plot the lattice parameters after water and acid exposure was determined from ICP data and Equation [4.6].

4.5. Washing at constant pH

As was seen in Figure 4.3 and Figure 4.5, the pH of the solution changes continually during the stirring of the material in water and in acid. This makes it difficult to distinguish at which pH range the two regimes occur. To study the cross-over point between the Li^+/H^+ ion exchange regime and delithiation-dissolution regime, washing tests as constant pH value 2, 7 and 10 were carried out. Figure 4.20 A shows the percentage of Li removed after stirring the materials at constant pH for 24 h. Figure 4.20 B shows the percentage of transition metals dissolved and found in solution after the 24 h stirring period. Figure 4.20 B shows a significant dissolution of transition metals at pH 7 especially for LNO. This is not observed when washing with water because the pH of the solution is at 7 for a very brief period of time; the solution's pH jumps to basic levels shortly after coming in contact with the material. Transition metal dissolution, which is a characteristic of the delithiation-dissolution regime, appears to begin at a significant level at a pH value around 8.5. However, Figure 4.20 also shows that the pH at which the delithiation-dissolution regime begins depends on the Ni-content of the material and its morphology.
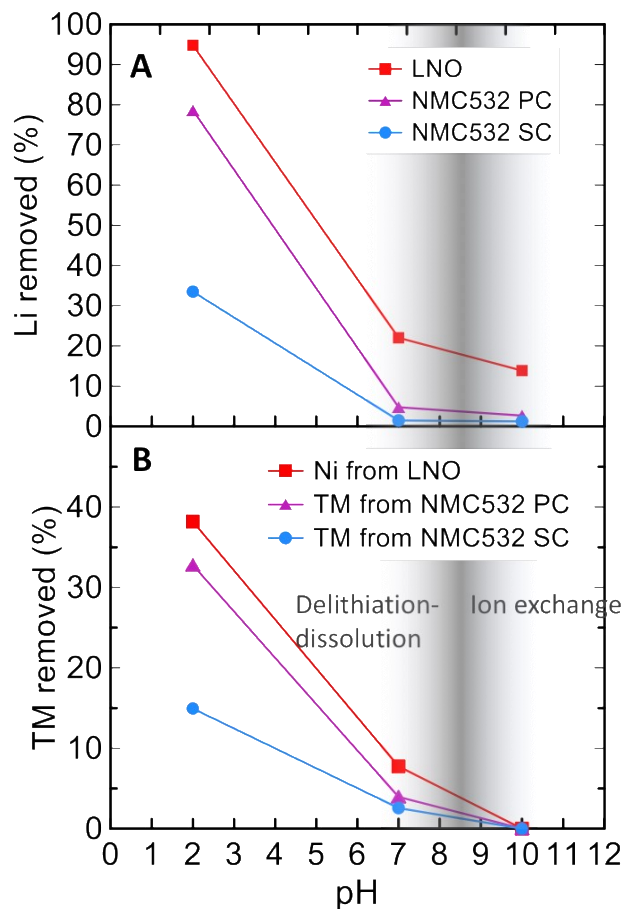
Figure 4.20. percentage of Li removed (A) and mole percentage of transition metal atoms removed (B) from LNO, NMC532 PC and NMC532 SC after stirring at constant pH for 24 h.

4.6. Conclusions derived from washing Ni-rich materials

It is irrefutable that Ni-rich materials react with aqueous solution and that the reaction mechanism depends on the pH of the washing solution used. At high pH (neutral and basic pH values), the material undergoes Li^+/H^+ ion exchange. This reaction results in a material that is delithiated and contains H^+ in its lithium layer; in this study, ion exchange has been confirmed to occur during water washing by ICP-OES and TGA-MS. When the washing solution is of low pH (acidic), little to no Li^+/H^+ ion exchange occurs. When the solution

is acidic the material is both delithiated and dissolved during washing. The delithiation-dissolution mechanism was confirmed to occur at low pH values by ICP-OES and TGA-MS as well. Materials that contain higher Ni-content are more prone to Li^+/H^+ ion exchange and to delithiation-dissolution. Materials that have a single crystal morphology are less reactive to aqueous solutions than materials of polycrystalline structure.

SEM images of the materials after water and acid washing show that the reaction of this materials with aqueous solutions alter their particles' surface in ways that are not seen during conventional delithiation when charging a Li-ion cell. The delithiation-dissolution regime causes material loss and creates gaps between the primary particles of polycrystalline materials which decreases the conductivity of the materials.

The pH at which the cross-over between regimes occurs is around 8.5 as shown in Figure 4.20. This figure is a useful, albeit rough, guide to develop washing procedure for Ni-rich materials. Figure 4.20 shows that, depending on the Ni-content and the morphology of the material, more basic solutions are preferable to minimize Li^+/H^+ ion exchange and material dissolution. Moreover, if a large volume of washing solution per LTMO mass is used during washing, the pH of the solution will rise less and the risks of Li delithiation and TM dissolution is higher.

CHAPTER 5. Impurity growth and effects of washing core-shell materials

The results presented in this chapter were collected by visiting undergraduate student from the Birla Institute of Technology and Science Pilani, Divya Rathore. The following study would not have been possible without Divya's hard work and effort.

Ni-rich materials have higher surface reactivity than Co-rich or Mn-rich materials. As was shown by the Ni-rich material washing study in Chapter 4, the higher the Ni-content is in a positive electrode material, the more reactive the material becomes to aqueous solutions. Moreover, Ni-rich materials make high capacity positive electrodes forcing Li-ion cell manufacturers to compromise capacity for surface stability. To maximize capacity and minimize impurity growth and surface reactivity, core-shell materials with Ni-rich cores and Ni-poor shells could provide an optimized positive electrode material design. In this chapter, the effectiveness of core-shell materials to reduce surface reactivity was tested.

The two core-shell materials (CS) at the center of this study are CS LNO:NiMn8020 17:1 and CS LNO:NiMn8020 16:2. This nomenclature identifies the composition of the core, here $LiNiO_2$ (LNO), to the composition of the shell, here $LiNi_{0.8}Mn_{0.2}O_2$ (NiMn8020), and gives the diameter of the core in μm to the contribution of the shell to the diameter in μm. The thickness of the shells of the two CS materials are 0.5 μm and 1.0 μm. A 0.5 μm thick shell will add 1.0 μm to the diameter and a 1.0 μm shell will add 2.0 μm to the diameter, hence the labels 17:1 and 16:2 respectively. This way, it is quick to see that the total diameter of both materials is 18 μm. For simplicity, these CS materials will be referred to as CS 17:1 and CS 16:2. The CS materials were stirred in water to study their reactivity

during washing. They were also exposed to humid air to observe the rate of impurity growth on their Mn-rich surface under extreme atmospheric conditions. In order to draw meaningful conclusions, uniform particles of LNO, NiMn8020 and commercially used NMC811 were exposed to the same conditions as the CS materials to compare performance. Table 2.2 lists details about the materials used in this study.

5.1. Washing CS materials in water

Acid-base titration analysis

After washing the CS materials and their comparative materials with distilled deaerated water, the collected washing solutions were analyzed by acid-base titration. Figure 5.1 shows the titration curves for the materials for washing periods up to 6 h. The titration curves indicate that the same Li^+/H^+ ion exchange mechanism which produces LiOH is occurring when CS materials are exposed to water. This reaction mechanism is described and validated in Chapter 4 for layered LTMO materials with compositionally uniform particles exposed to water. The amount of LiOH generated from LNO shown in Figure 5.1 A is the highest amongst the tested materials as should have been expected. CS 17:1 produces less LiOH than LNO, which has the same composition as its core, but produces more LiOH than NiMn8020, which has the same composition as its shell as shown in Figure 5.1 B. The titration curves for CS 16:2 material in Figure 5.1 C show that a thicker Mn-rich curve further decreases the rate of Li^+/H^+ ion exchange. It must be noted that the overall Ni-content of CS17:1 (97.23%) is higher than that of CS 16:2 (93.5%).

When comparing the titration curves for NMC811 and NiMn8020, shown in Figure 5.1 D and Figure 5.1 E respectively, the effect of Mn and Co content can be seen. These two materials both have transition metal layers containing 80% Ni, but NiMn8020 contains 20% Mn while NMC811 only contains 10% Mn. The presence of Co at a 10% level in NMC811 does not seem to give NMC811 an advantage in terms of minimizing reactivity with water. Increasing the Mn-content to 20%, as in the case of NiMn8020, reduces Li^+/H^+ ion exchange making this material the most resilient to water exposure amongst these five tested materials.
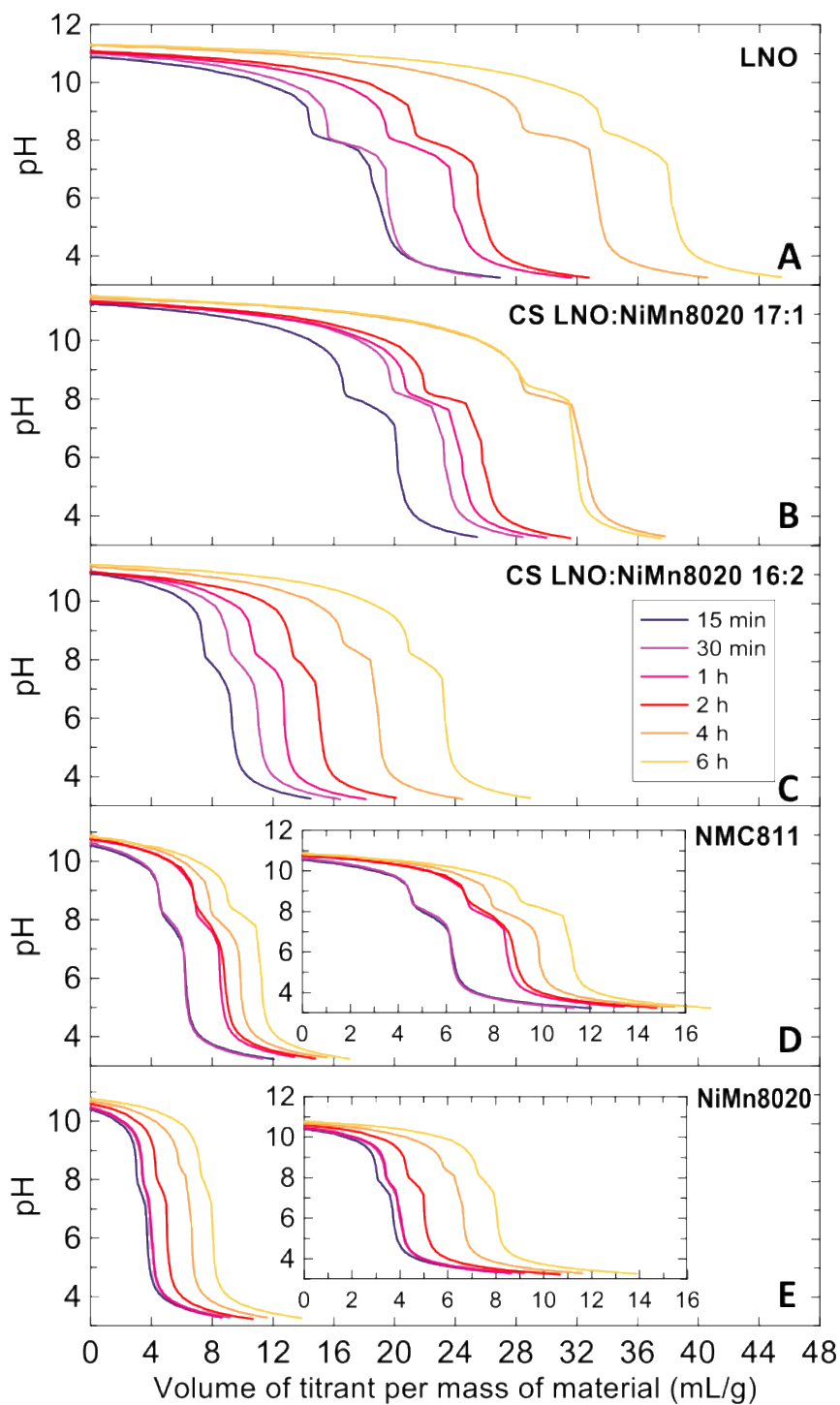
Figure 5.1. Titration curves for LNO (A), core-shell material 17:1 (B), core-shell material 16:2 (C), NMC811 (D) and NiMn8020 (E) with 0.5 g of cathode material powder in 100 mL of deaerated distilled water with 0.05 M HCl as titrant.

From the titration data shown in Figure 5.1, the percentages of Li removed from the materials and found in solution were calculated as per Equation [4.2]. Figure 5.2 shows these calculated percentages and shows that the Li loss from LNO and CS 17:1 are comparable. After 6 h of stirring in water LNO loses around 18% of its Li content and CS 17:1 loses around 16%. It is only with CS 16:2, where the shell thickness is doubled, that a significant improvement in Li loss was observed at about 11% after 6 h. The Li loss for both NMC811 and NiMn8020 is below 6%. However, NiMn8020 shows more stability in water when compared to NMC811.
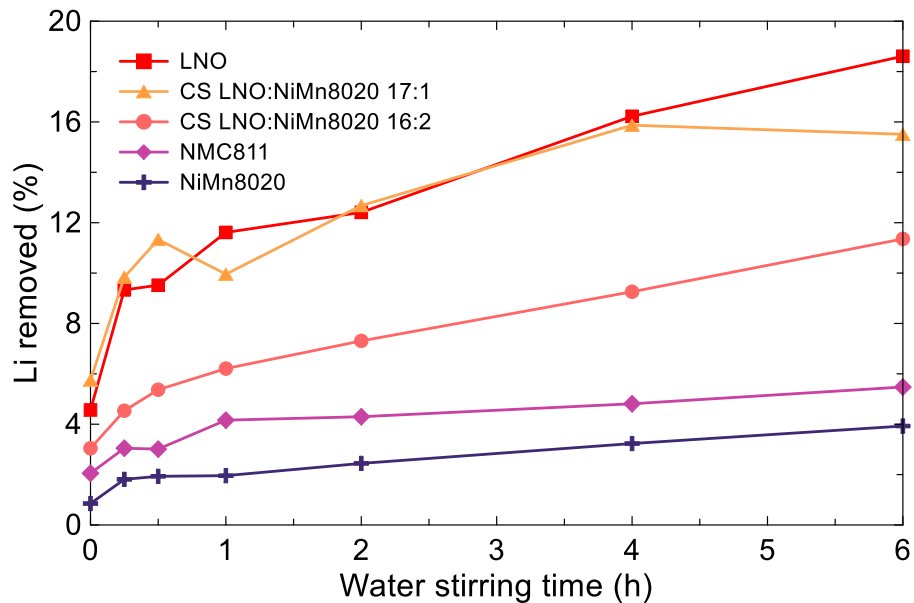
Figure 5.2. Percentage of original Li content in the core-shell materials and the comparative materials found in the solution after stirring in water calculated from the pH increase of the solution using Equation [4.2].

TGA-MS analysis

The thermal decomposition of the two studied CS materials, CS 17:1 and CS 16:2 was compared to that of bare LNO with materials in their pristine state, after stirring in water

for 15 min, 30 min and 1 h. Figure 5.3 shows a two-step decomposition between 150ºC and 350ºC for the washed materials. This two-step mass loss is similar to the one observed for uniform layered LTMOs washed in water and is expected to correspond to water evolution and oxygen evolution in that order. This is due to the presence of H^+ as a consequence of Li^+/H^+ ion exchange. Figure 5.3 also shows that much of the Li^+/H^+ ion exchange process is carried within the first 15 min of washing, after which the rate of ion exchange slows considerably. The advantage of a thicker Mn-rich shell is seen again in these TGA results, as CS 16:2 proves to contain less H^+ in its crystal lattice than CS 17:1.
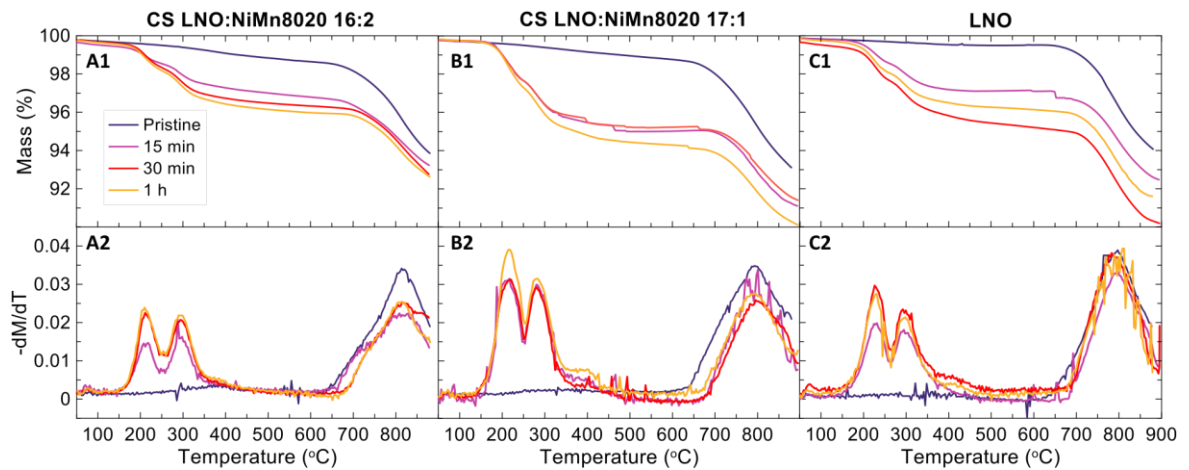
Figure 5.3. TGA data for CS 16:2 (A), CS 17:1 (B) and LNO (C) after stirring in water for different time periods showing remaining mass percentage of the samples heated to 900°C (1), and the inverse derivative of the mass percentage profile with respect to temperature (2).

Figure 5.4 identifies the gases released during the thermal decomposition of the samples washed after 15 min. It is confirmed that the first step in mass loss between 150ºC and 350ºC corresponds to water and oxygen release due to the intercalation of H^+ in the materials as per Equation [4.4]. The mass loss beginning at 650ºC that is seen in Figure 5.3

and Figure 5.4 is due to oxygen evolution. This mass loss corresponds to the decomposition of the delithiated materials as they transform to the rocksalt phase.

CO_2 evolution can also be noticed during the thermal decomposition of the materials particularly in the case of CS 17:1 as shown in Figure 5.4 B3. The evolution of CO_2 implies the presence of carbonate and/or bicarbonate species on the surface of the material. The samples analysed in Figure 5.4 were only washed for 15 min and it is possible that there were remaining impurities on the surface of the particles.
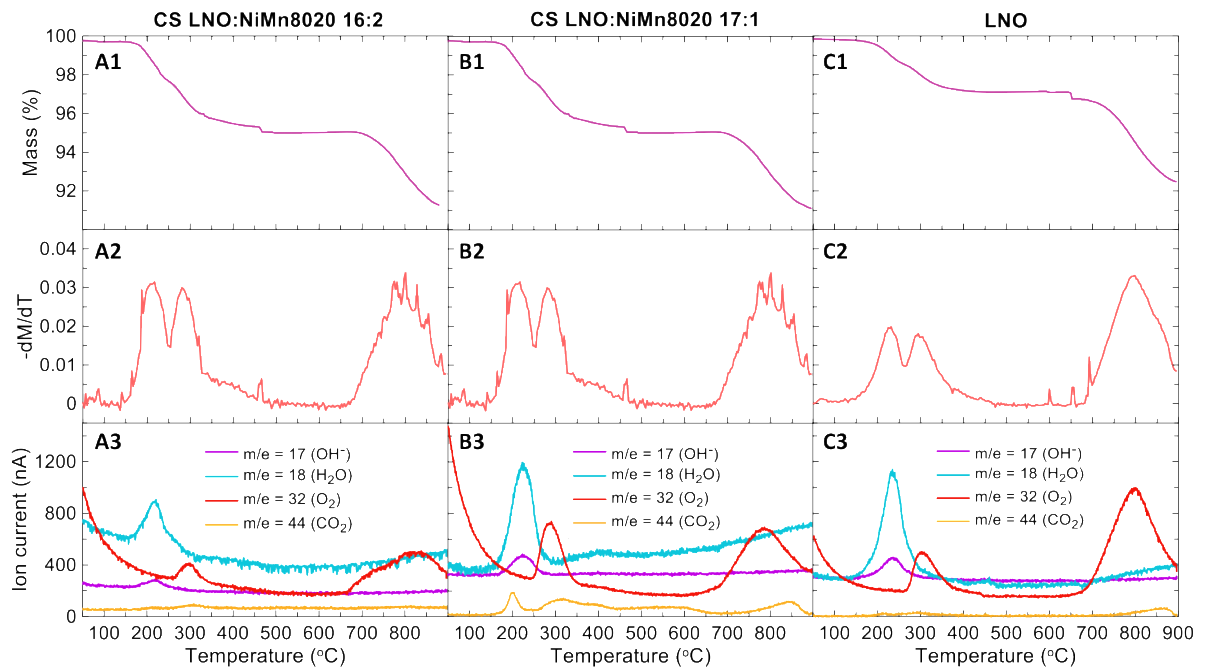
Figure 5.4. TGA-MS data CS16:2 (A), CS17:1 (B) and LNO (C) after stirring in water for 15 min showing remaining mass percentage of the samples heated to 900°C (1), the inverse derivative of the mass percentage profile with respect to temperature (2) and the mass spectroscopy ion current signal for 4 selected masses as indicated (3).

90

From these results it is clear that the Li^+/H^+ ion exchange continues to occur even in CS materials with Mn-rich shells. The extent of ion exchange and consequent Li loss is improved in the studied CS materials as opposed to Ni-rich uniform materials, but this improvement depends on the thickness of the Mn-rich shell. CS 16:2 shows that with a 1 µm thick shell, Li^+/H^+ ion exchange was reduced during water washing more efficiently than with a 0. 5 µm thick shell.

5.2. Exposure of CS materials to humid air

To study the surface impurity growth of CS materials with Ni-rich cores and Mn-rich shells, samples of each of the studied materials were exposed to humid air with a relative humidity (RH) of 99% and at a constant temperature 22ºC. To obtain distinguishable signals during the analysis of these materials, air exposure tests had to be carried for considerably longer durations. Figure 5.5 shows the TGA results for the thermal decomposition of the two studied CS materials compared to that of bare LNO. The Li^+/H^+ ion exchange process which occurs during water washing is expected to be observed for layered LTMOs exposed to humid air. At a RH of 99%, the material's surface is bound to come in contact with water molecules that would then react with Li at the surface of the particles. This explains the two-step mass loss in the 150ºC and 350ºC. Li^+/H^+ ion exchange produces LiOH at the surface of the material, but it is not the only source of LiOH; the presence of residual Li from material synthesis is believed to result in surface Li_2O which also reacts with water to form LiOH on the material's surface.

Furthermore, mass loss in the 350ºC to 500ºC range, which was not observed in water washed samples, is observed in the materials after air exposure as shown in Figure 5.5. This additional mass loss seems to also occur in two-steps as can be most clearly seen in Figure 5.5 C2. The transformation of the delithiated material to the rocksalt phase remains expected at high temperature. It is important to remember that these materials are not washed and are likely to contain Li_2CO_3 as well as $LiHCO_3$ in addition to the LiOH produced during Li^+/H^+ ion exchange. The humidity chamber where the samples were placed was closed with a vacuum greased seal, but CO_2 exposure occurred because the chamber had to be opened to remove sample from time to time. Consequently, reactions with CO_2 would lead to the growth of carbonate and bicarbonate species on the surface. The thermal decomposition of Li_2CO_3 occurs at temperatures above 700ºC and could contribute to the mass loss seen at high temperature.

Figure 5.5 shows similar mass losses for CS 16:2, CS 17:1 and LNO after 16 days, but the mass loss for CS 16:2 is significantly less than that of CS 17:1 and LNO after the first 8 days of exposure to moisture. The TGA results in Figure 5.5 A1 show that CS 16:2 displayed the highest air stability amongst the tested materials. This implies that the Mn-rich shell has somewhat shielded the Ni-rich core of the CS 16:2 particles from the high humidity conditions. TGA results in Figure 5.5 B1 also shows that CS 17:1 is slightly more resilient than bare LNO in terms of surface stability.
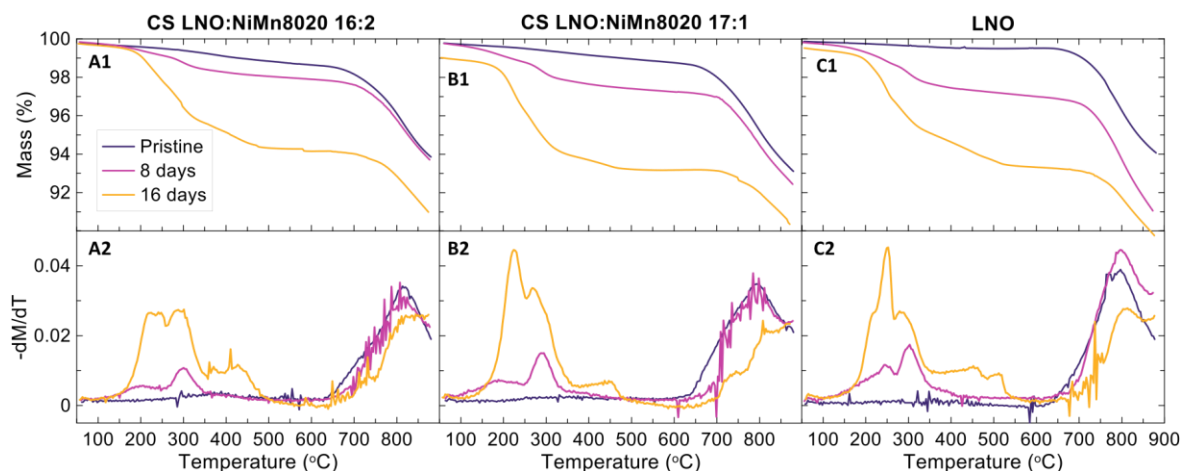
Figure 5.5. TGA data for CS 16:2 (A), CS 17:1 (B) and LNO (C) after exposure to humid air for different time periods showing remaining mass percentage of the samples heated to 900°C (1), and the inverse derivative of the mass percentage profile with respect to temperature (2).

Figure 5.6 identifies the evolved gases corresponding to the mass loss observed during the thermal decomposition of the materials after 16 days of humid air exposure. Li^+/H^+ is confirmed by the water and oxygen gas releases corresponding to the two-step mass loss beginning around 150°C. The mass loss between 350°C and 500°C is accompanied by an evolution of H_2O and CO_2. This suggests that it could possibly be due to the decomposition of $LiHCO_3$ present on the surface of the materials. Equation [5.1] shows the decomposition reaction of $LiHCO_3$. This decomposition reaction produces H_2O and CO_2 gas and leaves additional Li_2CO_3 on the surface of the particles.

$$2LiHCO_{3(s)} \longrightarrow Li_2CO_{3(s)} + CO_{2(g)} + H_2O_{(g)} \qquad [\ 5.1\ ]$$
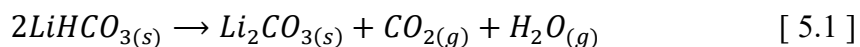
Mass loss at higher temperature corresponds to the release of oxygen which occurs during the transformation of the material to the rocksalt phase. There is also an evolution of CO_2

that occurs at temperatures above 750ºC. This is likely due to the decomposition of the Li$_2$CO$_3$ present initially on the surface and the Li$_2$CO$_3$ left behind from the decomposition of LiHCO$_3$.
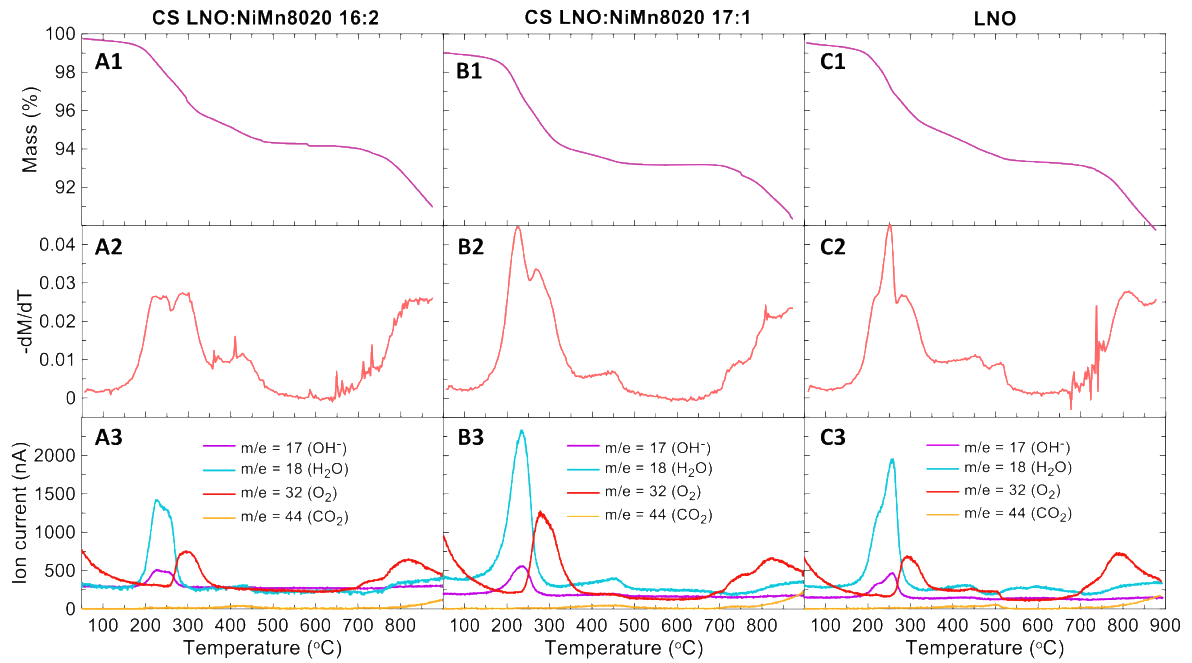
Figure 5.6. TGA-MS data for CS 16:2 (A), CS 17:1 (B) and LNO (C) after exposure to humid air for 16 days showing remaining mass percentage of the samples heated to 900°C (1), the inverse derivative of the mass percentage profile with respect to temperature (2) and the mass spectroscopy ion current signal for 4 selected masses as indicated (3).

It has been suggested by Sicklinger *et al.* that basic transition metal hydroxides and carbonates form on the surface of positive electrode active materials during exposure to moisture.[82] This suggestion was made to explain the evolution of CO$_2$ and H$_2$O at low temperatures (125ºC and 625ºC) since it cannot be attributed to the decomposition of lithium compounds. To verify the presence or lack of transition metal hydroxides and carbonates at the surface of the materials, their TGA-MS signature was compared to the observed signature of samples of the transition metal compounds in question suggested to

94

be present on the positive electrode particles. Figure 5.7. shows the comparison between the CO_2 and H_2O evolution profile for Li compounds and basic transition metal to the CO_2 and H_2O evolution curves observed from the washed and moisture exposed positive electrode materials. As expected, Figure 5.7 A and Figures 5.7 C show that Li_2O does not thermally decompose at temperatures below 900°C, except for some H_2O evolution that is likely due to residual LiOH, and Li_2CO_3 only decomposes at temperatures above 725°C. Figure 5.7 C also shows that the evolution of H_2O between 150°C to 300°C is not due to LiOH. Most importantly, Figures 5.7 B and Figures 5.7 D do not confirm the presence of transition metal hydroxides and carbonates on the washed or moisture exposed materials. It is worth noting, that the use of reference TGA-MS profiles must be done with caution as LiOH and Li_2CO_3 react with $Ni(OH)_2$ at temperatures lower than their decomposition temperatures. Therefore, the reference TGA-MS profiles of LiOH and Li_2CO_3 present on a positive electrode material and those of pure LiOH and Li_2CO_3 samples will differ.
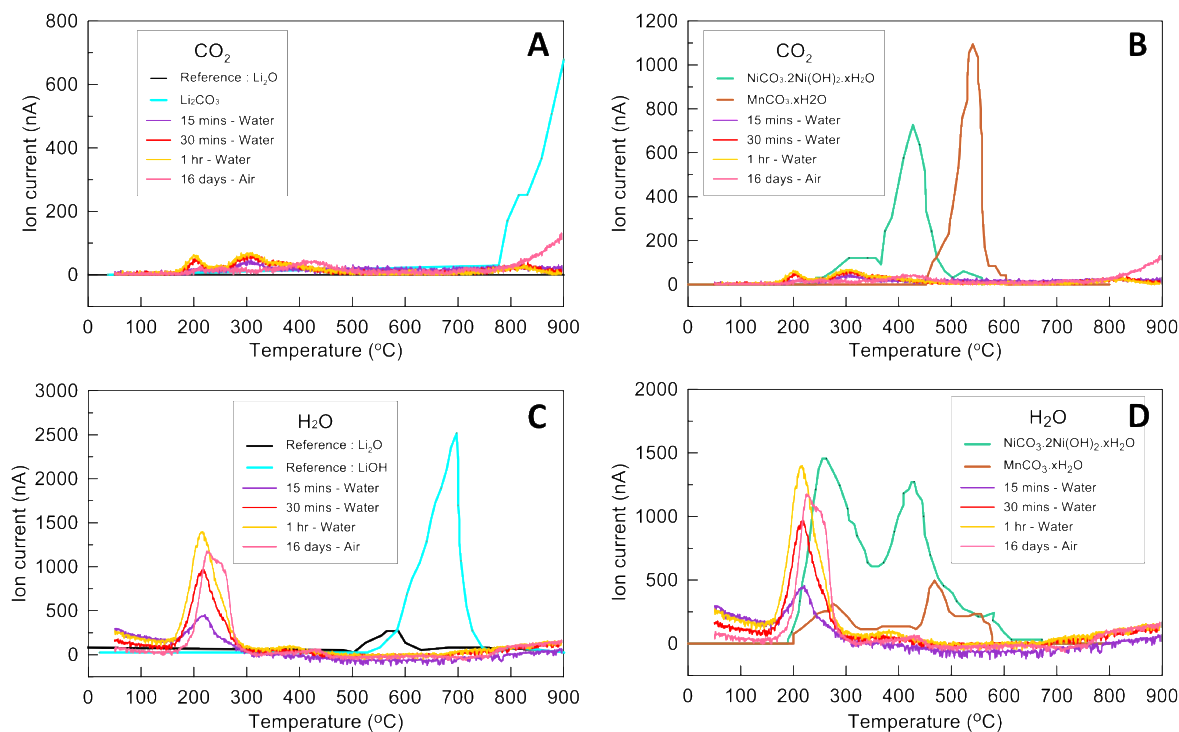
Figure 5.7. Reference TGA-MS signals for CO2 evolution during the thermal decomposition of Li_2O, Li_2CO_3 (A) hydrated $NiCO_3 \cdot 2Ni(OH)_2$ and hydrated $MnCO_3$ (B). Reference MS signals for H2O evolution during the thermal decomposition of Li_2O, $LiOH$ (C) hydrated $NiCO_3 \cdot 2Ni(OH)_2$ and hydrated $MnCO_3$ (D).

5.3. Conclusions derived about impurity growth and washing of core-shell materials

The reaction of CS materials with water follows the same Li^+/H^+ ion exchange reaction as uniform LTMO materials do. The reactivity of the material is known to be strongly correlated to the Ni-content of the material. For this reason, CS materials composed of a Ni-rich core shielded by a Ni-poor shell have been studied as a possible solution to the design of Ni-rich materials for high-capacity positive electrodes with improved surface stability.

96

The correlation between Ni-content and water reactivity has remained true despite the non-uniform distribution of the Ni in the particles. When the Ni-content is equal, the concentration of Mn in the material showed evidence of improved stability as seen from the titration curves of NMC811 and NiMn8020 (see Figure 5.1). This reaffirms that Mn-rich shells are best for improved surface stability.

The two studied CS materials had Mn-rich shells and Ni-rich cores of equal composition but differing shell thicknesses. The 0.5 μm thick shell on CS 17:1 did not show significant improvement in terms of diminished reactivity to water when compared to bare LNO. However, when the Mn-rich shell was 1 μm in thickness, reduction in Li^+/H^+ ion exchange was observed. When Ni-rich LTMOs were exposed to air, the material reacted with water molecules by the Li^+/H^+ ion exchange reaction which produced LiOH. Additionally, carbonate and bicarbonate species also formed on the surface of the material due to the presence of CO_2. CS 16:2 has shown to be considerably more resilient to the detriments of humid air especially during the first 8 days of exposure when compared to bare LNO or even CS 17:1.

TGA-MS analysis has also shown that the extent of Li^+/H^+ ion exchange that occurred in LNO after 8 days of exposure at a 99% RH is comparable to the Li^+/H^+ ion exchange which occurred in LNO after merely 15 min of washing with water; this emphasizes the impact of the washing process employed in industry on Ni-rich materials. Fortunately, CS materials appear to be a promising material design for high-capacity, high-stability positive electrode materials.

CHAPTER 6. Conclusion

6.1. Summary of important results

The washing of Ni-rich positive electrode active materials with an aqueous solution is currently a common and necessary process for Li-ion cell manufacturers to ensure that the surface of the materials does not contain a level of contaminants that would be detrimental to cell performance. The propensity for the growth of Li impurity species, most commonly LiOH, Li_2CO_3 and/or $LiHCO_3$, on the surface of the positive electrode materials is due to the reaction of the materials with H_2O and CO_2 during exposure to ambient air. These impurities reduce cell cycle life, capacity and safety.

However, while washing the materials of their impurities, the moisture-sensitive positive electrode materials react with the aqueous washing solution. In this work it has been shown that the reaction between Ni-rich LTMOs and aqueous solutions is dependent on the pH of the solution:

1. At high pH, Li^+/H^+ ion exchange occurs where the Li ions intercalated in the material migrate out of the crystal structure and H^+ present in the solution migrates inwards to fill the Li^+ vacant sites. In this regime, little to no material dissolution occurs while the resultant LTMO material becomes delithiated and contains H^+. This mechanism was confirmed by ICP-OES analysis which showed that only trace levels of transition metal ions were found in solution after washing the LTMO. Additionally, TGA-MS analysis

showed the evolution of H_2O from the thermal decomposition washed material due to the presence of H^+ in the material.

2. At low pH, delithiation and dissolution occur where part of the material is delithiated while part is dissolved. This mechanism was confirmed by ICP-OES analysis which showed considerable concentrations of transition metals found in solution after washing. The delithiation-dissolution reaction has a signature 2:1 Li to TM ratio which was also observed from ICP-OES results. The TGA-MS analysis showed little to no presence of H^+ in the material. Moreover, the XRD analysis of the materials after washing showed an agreement between the expected changes in the lattice constants of materials and the delithiation state predicted by the delithiation-dissolution mechanism. A noteworthy conclusion from the XRD analysis is that the delithiation was shown to occur throughout the bulk of the material and not just at the surface and subsurface regions of the particles as was evidence by the single phase observed from XRD. It was also noticed by SEM analysis that when exposed to washing solutions of low pH, the positive electrode polycrystalline materials develop large gaps between their primary particles.

The extent of the reaction in both regimes is correlated to the Ni-content of the material; a higher Ni-content results in a higher rate of reaction with aqueous solution. It was also observed that single-crystal materials show less reactivity than their polycrystalline counterparts. To study the cross-over pH between the two regimes, constant-pH washing tests were carried out. The results suggest that the cross-over pH value is higher than 7 but lower than 10. However, the precise cross-over pH depends on the Ni-content of the material and its morphology.

The ratio of solution volume to LTMO mass used during washing also has important impact on the reaction rate. When a large amount of solution is used relative to the material the pH will remain lower, and at low pH, more delithiation and more dissolution is more likely to occur.

A promising positive electrode active material design with high Ni-content and better air stability is the core-shell particle design with a Ni concentration-gradient throughout the particle. The CS materials studied in this work have Ni-rich cores (16 to 17 µm in diameter) and Mn-rich shells (1.0 to 0.5 µm in thickness). The reactivity of the CS materials was tested in water and in humid air. When CS materials are washed in aqueous solution, they react in the same way as uniform LTMO particles. Li^+/H^+ ion exchange occurs between the material and water, but the Mn rich surface of the tested CS materials results in a slight increase of resilience to ion exchange. The surface stability of the material is further increased with increased shell thickness.

Humid air exposure experiments allow for the analysis of the impurity species. Due to moisture in the air, the CS materials came in contact with water causing Li^+/H^+ ion exchange. This produced LiOH species at the surface of the material in addition to any existing LiOH due to residual Li from synthesis. LiOH then reacts with CO_2 in air to form lithium carbonate and possibly lithium bicarbonate as suggested by TGA-MS results. No transition metal hydroxides or transition metal carbonates were detected on the CS materials exposed to air.

A thicker Mn-rich shell signifies a lower content of Ni which would reduce the capacity of the positive electrode material, but also the CS material with the thicker shell showed more resilience to surface impurity growth particularly during the 8 first days of exposure to moisture. The implementation of CS material designs and the improvement of positive electrode washing procedures are two complementary solutions to the commercialization of high Ni content cells with excellent electrochemical properties.

6.2. Future work

The work presented in this thesis aimed to provide insight about the fundamental changes that occur to Ni-rich positive electrode materials when washing with aqueous solutions. With this better understanding of the materials' reaction, further studies can be carried out to expanded on this knowledge. Furthermore, this can allow to develop more effective ways of avoiding surface contamination and/or avoiding material degradation during washing. Possible works, which would complement and add value to this study, are outlined in this section.

6.2.1. Study of surface reactivity of other positive electrode materials

In addition to the materials studied in this work, there exists countless Ni-rich positive materials of different elemental composition whose surface reactivity is worth examining. $LiNi_xMn_{1-x}O_2$ materials where x is 0.8, 0.85, 0.90 or 0.95 are all available materials that should be studied to observe the Ni to Mn ratio that is optimal for both high capacity and high air stability. Following similar water and air exposure procedures as the ones used in

this work, the optimal percentage of Mn substituents in the crystal structure can be determined. Additional studies of the reactivity of other positive electrode materials of different crystallographic structure, such as olivine LFP, would provide further understanding of impurity growth and metal dissolution in positive electrode materials. LFP is a promising safe and cost-effective positive electrode material. However the degradation of LFP in ambient atmosphere has been observed and humidity is thought to be responsible for the deintercalation of Li and the formation of an amorphous phase at the surface of the material. Olivine LFP has an OCV of 3.45 V vs. Li^+/Li and suffers of poor air stability and Li loss in ambient atmosphere. Ambient air exposure of LFP results in both Li deintercalation and partial oxidation of LFP; however, this degradation mechanism in air remains debatable. Understanding the reactivity of LFP to air is crucial as this material is synthesized in the form of nanopowder and has high surface area, and thus, a high rate of reaction to air.[83, 84]

6.2.2. Study of the electrochemical performance of washed materials

Testing the electrochemical performance of the materials after washing with different solutions of different pH would allow to further affirm the conclusions drawn from this study. Yokoyama et al. suggest that washing positive electrode materials should be carried at pH values between 11 and 13.[57] Others have suggested alcohol washing of positive electrode materials as an alternative to water washing.[61] Comparing the impact of these washing techniques on the electrochemical performance of the materials would provide further guidance towards developing better washing practices. Impedance and capacity

measurement as well as cyclability and storage tests would provide results that are indicative of the effectiveness of the washing procedure used.

6.2.3. Development of core-shell materials and coating for high air stability

Other CS material compositions and concentration-gradients should be studied as CS materials are a promising category of materials with the potential to stabilize Ni-rich material particles. Other metals besides Mn, such as Al for instance, can also be incorporated in the material to further increase the air stability of the material. Although improvement in air stability of CS materials containing Co have been reported,[85] there remains countless Co-free CS materials of different compositions and different shell parameters to be tested. Additionally, coating positive electrode particles could reduce the surface reactivity of the materials. There exist many material coating techniques such as wet coating methods and atomic layer deposition, etc. Among these techniques, mechanofusion is an effective dry processing method for forming robust, dense coatings on positive electrode particles. LNO particles mechanofusion-coated with alumina have shown improved cycling performance compared to uncoated LNO.[86] Mechanofusion coating could provide another approach to particle surface modification that would improve both the electrochemical performance of the material and reduce air and/or water reactivity.

6.2.4. Study of thermal stability and safety

The study of thermal stability of Ni-rich material is critical for the commercialization of materials with higher Ni-content, particularly for the application of EV where safety is of utmost importance. The thermal stability of a positive electrode material is also closely

related to surface reactivity and, just like air stability, it is reduced with increased Ni-content. Accelerated rate calorimetry analysis of positive electrode materials (of uniform composition and of CS composition) would provide further insight into the thermal stability and the safety of these materials.

6.2.5. Study of microcracking and metal dissolution in positive electrodes

This work has provided insight about the degradation of Ni-rich LTMOs and their surface reactivity. Microcracking is a common failure mechanism observed in Ni-rich materials, known to aggravate capacity fade and deserves further studies. SEM analysis of the studied polycrystalline LTMOs after acid washing identified large gaps between their primary particles (See Figure 4.6 and Figure 4.7). These gaps resemble the microcracks seen in Ni-rich electrodes after cycling by Watanabe et al.[87] Figure 6.1 A shows cross-sectional SEM images of NCA electrodes after cycling at equal current (400 mA) and at two different temperatures reported by Watanabe et al. It is clear from the SEM images that the microcracking is more severe when the electrode is cycled at high temperature (60ºC) as opposed to lower temperature (25ºC). Figure 6.1 B shows the correlation between the extent of electrode microcracking and the capacity fade of the Li-ion cell where the prominently cracked electrode saw rapid capacity loss with cycling. Interestingly, Figure 6.1 C shows no changes in the XRD profiles of the electrode materials which signifies no expansion or changes in the crystal structure. This does not eliminate the possibility of material delithiation-dissolution which would cause both microcracks and capacity loss as was seen by acid washing experiments in this study. The positive electrode material microcracks were not the focus of this work but understanding and preventing the

formation of microcracks is an important challenge for making high performance Ni-rich

electrodes.
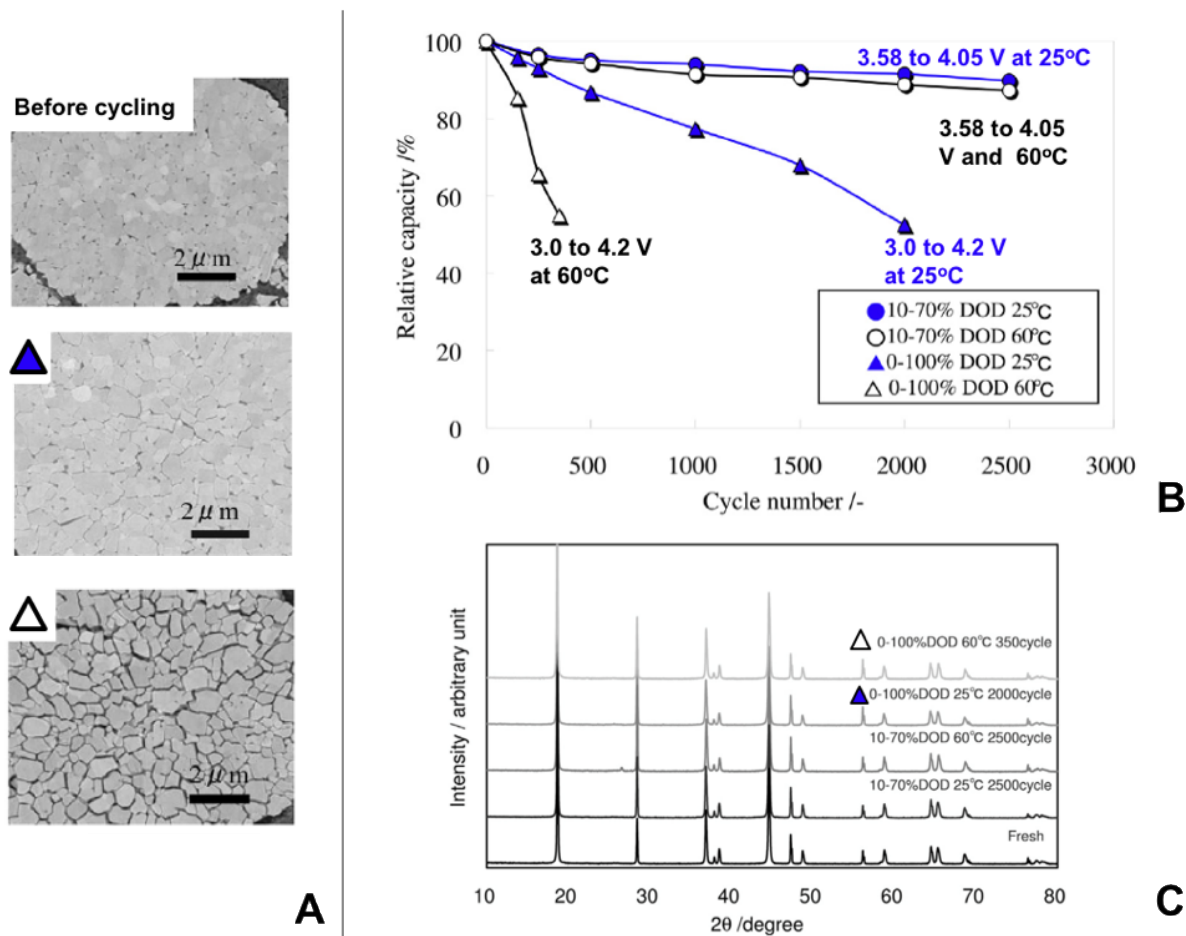
Figure 6.1* – adapted from reference.[87] Results from Watanabe's cycling experiments of NCA /graphite cells cycled at two different temperatures. Cross-sectional SEM images illustrating microcracks and pores in the NCA electrodes (A) Cycling performance of the cells at a current rate of 1C (400 mA) (B) and XRD profiles of the NCA electrodes (C). The SEM image labelled by "Δ" in Figure 17A corresponds to a cross-section of an electrode particle after 60°C testing. The microcracks in Figure 17A Δ are very similar to those shown in Figures 5C and 6C.

Metal dissolution, which was observed to be prominent in Ni-rich materials exposed to H^+, is a mechanism which is known to occur in Li-ion cells and to cause reduced cell lifetime and increase safety risks. As was mentioned in section 2.3, the hydrolysis of $LiPF_6$ salt by trace amounts of water found in the cell produces HF acid in the electrolyte. This corrosive acid can then react with the LTMO in the positive electrode which will produce more water and create a positive feedback loop of salt hydrolysis and HF formation. This mechanism would also exacerbate the widening of any microcracks found on the particles' surface similarly to crevice corrosion. This is an important mechanism to study as it not only causes considerable loss of electrochemically active material, but it also results in dissolved metals in solution that could migrate to and deposit on the negative electrode. This might induce Li metal dendrite growth on the deposited transition metals which can lead to electric shorts and the destruction of the cell. Therefore, there is interest in the study of electrolyte additives capable of scavenging HF to reduce the corrosion of the positive electrode.

Further studies of the propensity of Ni-rich positive electrode materials to impurity growth in air, metal dissolution in electrolyte and microcrack formation would be valuable additions to this study. The design of positive electrodes with an inexpensive and abundant transition metal such as Ni as opposed to Co while providing excellent electrochemical properties would allow for the fabrication of affordable, safe and high-performance Li-ion batteries.

Appendix A. ICP-EOS data and error analysis

Careful sample preparation prior to ICP-OES measurements was crucial to ensure that the concentrations of the elements measured were within the detection limits of the instrument. For samples where the concentration of the element to be measured exceeded the detection limit of the instrument, a dilution with a solution of 2% nitric acid was carried. The error on the element's measured concentration in ppm depended on three factors:

1. Error due to sample preparation: dilutions, when needed, were carried with as much accuracy as possible. However inevitable error due to the volume measurements will affect the concentration of the sample. The error due to the pipette that was used to measure the samples and the 2% nitric acid solution volumes was considered in the reported data.

2. Error due to the concentration of the element relative to the lower detection limit (LDL): When the concentration of the element measured is much higher than the LDL of the instrument, the yielded concentration data are more accurate. For the error to be as low as 2%, the concentration of the element must be at least 100 times larger than the LDL concentration. If the concentration is only 5 times larger than the LDL, the error on the measured concentration becomes 10%. Table A.1 shows the LDL for all elements measured in this work.

Table A.1. List of elements measured and their lower detection limit in ppb when using a radially-viewed plasma

Element	Lower detection limit (ppb)
Li	0.3
Ni	5.0
Mn	0.4
Co	1.0
Al	3.0

3. Regular standard deviation: the ICP-OES measured the concentration for each element in each sample three separate times. The mean and the regular standard deviation (RSD) of the data set is calculated and used for all analysis that followed.

The concentration measurement obtained from ICP-OES, along with its uncertainty, was then used to quantify the amount (in mol) of each element in solution. The error due to the volume measurement of the washing solution used and the mass of material washed was also considered to assess the overall uncertainty on this analytical process.

Appendix B. XRD Least squares refinement

LNO washed in water

Table B.1. Agreement between measured and calculated diffraction angles used to calculate lattice constants for LNO washed in water for different durations

LNO washed in water **[15 min]**					
h k l	2θ observed (°)	2θ corrected (°)	2θ calculated (°)	Delta 2θ (°)	Calculated d-spacing (Å)
0 0 3	18.706	18.742	18.748	-0.006	4.733
1 0 1	36.609	36.643	36.642	0.001	2.4505
0 0 6	37.957	37.991	37.991	0.001	2.3665
1 0 -2	38.273	38.307	38.305	0.002	2.3478
1 0 4	44.403	44.436	44.431	0.005	2.0373
1 0 -5	48.583	48.616	48.615	0.001	1.8713
1 0 -8	64.401	64.432	64.432	-0.001	1.4449
1 1 0	64.827	64.858	64.862	-0.004	1.4363
Calculated lattice constants (Å)					
a_h	2.8727	+- 0.0001			
c_h	14.1991	+- 0.0008			
LNO washed in water **[30 min]**					
h k l	2θ observed (°)	2θ corrected (°)	2θ calculated (°)	Delta 2θ (°)	Calculated d-spacing (Å)
0 0 3	18.811	18.75	18.752	-0.002	4.732
1 0 1	36.704	36.645	36.645	0.001	2.4503
0 0 6	38.058	37.999	38	-0.001	2.366
1 0 -2	38.363	38.305	38.308	-0.004	2.3476
1 0 4	44.503	44.446	44.437	0.009	2.037
1 0 -5	48.678	48.622	48.622	0	1.871
1 0 -8	64.496	64.444	64.445	-0.001	1.4446
1 1 0	64.917	64.865	64.867	-0.002	1.4362
Calculated lattice constants (Å)					
a_h	2.8725	+- 0.0001			
c_h	14.1959	+- 0.0009			

LNO washed in water [1 h]

h k l	2θ observed (°)	2θ corrected (°)	2θ calculated (°)	Delta 2θ (°)	Calculated d-spacing (Å)
0 0 3	18.731	18.744	18.748	-0.004	4.7329
1 0 1	36.639	36.652	36.649	0.003	2.45
0 0 6	37.982	37.995	37.992	0.003	2.3664
1 0 -2	38.298	38.31	38.311	-0.001	2.3474
1 0 4	44.428	44.44	44.437	0.003	2.037
1 0 -5	48.608	48.62	48.62	-0.001	1.8711
1 0 -8	64.426	64.437	64.438	-0.001	1.4447
1 1 0	64.862	64.873	64.875	-0.002	1.4361

Calculated lattice constants (Å)		
a_h	2.8722	+- 0.0001
c_h	14.1986	+- 0.0006

LNO washed in water [4 h]

h k l	2θ observed (°)	2θ corrected (°)	2θ calculated (°)	Delta 2θ (°)	Calculated d-spacing (Å)
0 0 3	18.716	18.726	18.735	-0.01	4.7361
1 0 1	36.654	36.664	36.654	0.01	2.4497
0 0 6	37.957	37.967	37.965	0.002	2.3681
1 0 -2	38.303	38.312	38.314	-0.002	2.3473
1 0 4	44.428	44.437	44.432	0.005	2.0372
1 0 -5	48.603	48.612	48.61	0.002	1.8715
1 0 -8	64.401	64.409	64.41	0	1.4453
1 1 0	64.872	64.881	64.887	-0.007	1.4358

Calculated lattice constants (Å)		
a_h	2.8717	+- 0.0002
c_h	14.2084	+- 0.0014

LNO washed in water [6 h]

h k l	2θ observed (°)	2θ corrected (°)	2θ calculated (°)	Delta 2θ (°)	Calculated d-spacing (Å)
0 0 3	18.776	18.72	18.726	-0.006	4.7384
1 0 1	36.739	36.685	36.679	0.006	2.4481
0 0 6	38.003	37.949	37.946	0.003	2.3692
1 0 -2	38.398	38.345	38.337	0.007	2.3459
1 0 4	44.498	44.445	44.447	-0.001	2.0366
1 0 -5	48.663	48.611	48.62	-0.009	1.8711
1 0 -8	64.456	64.408	64.404	0.004	1.4454
1 1 0	64.983	64.935	64.939	-0.004	1.4348

Calculated lattice constants (Å)		
a_h	2.8696	+- 0.0002
c_h	14.2151	+- 0.0014

LNO washed in water [24 h]					
h k l	2θ observed (°)	2θ corrected (°)	2θ calculated (°)	Delta 2θ (°)	Calculated d-spacing (Å)
0 0 3	18.701	18.699	18.713	-0.014	4.7416
1 0 1	36.689	36.687	36.681	0.007	2.448
0 0 6	37.942	37.94	37.919	0.021	2.3708
1 0 -2	38.338	38.336	38.337	0	2.346
1 0 4	44.438	44.436	44.438	-0.002	2.037
1 0 -5	48.603	48.601	48.607	-0.005	1.8716
1 0 -8	64.366	64.364	64.373	-0.009	1.4461
1 1 0	64.947	64.946	64.943	0.003	1.4347
Calculated lattice constants (Å)					
a_h	2.8695	+- 0.0003			
c_h	14.2248	+- 0.0025			

LNO washed in 0.05 M of HCl solution

Table B.2. Agreement between measured and calculated diffraction angles used to calculate lattice constants for LNO washed in acid for different durations

NMC532 PC washed in acid [15 min]					
h k l	2θ observed (°)	2θ corrected (°)	2θ calculated (°)	Delta 2θ (°)	Calculated d-spacing (Å)
0 0 3	18.721	18.74	18.741	-0.001	4.7347
1 0 1	36.659	36.677	36.674	0.003	2.4484
0 0 6	37.957	37.975	37.977	-0.002	2.3673
1 0 -2	38.313	38.331	38.334	-0.003	2.3461
1 0 4	44.438	44.455	44.453	0.002	2.0363
1 0 -5	48.618	48.635	48.632	0.003	1.8707
1 0 -8	64.421	64.437	64.437	0	1.4448
1 1 0	64.907	64.923	64.926	-0.002	1.4351
Calculated lattice constants (Å)					
a_h	2.8702	+- 0.0001			
c_h	14.2041	+- 0.0006			

NMC532 PC washed in acid [30 min]

h k l	2θ observed (°)	2θ corrected (°)	2θ calculated (°)	Delta 2θ (°)	Calculated d-spacing (Å)
0 0 3	18.786	18.715	18.72	-0.005	4.7399
1 0 1	36.765	36.696	36.696	0.001	2.447
0 0 6	38.008	37.94	37.934	0.006	2.37
1 0 -2	38.419	38.351	38.352	-0.001	2.345
1 0 4	44.523	44.457	44.456	0.001	2.0362
1 0 -5	48.693	48.628	48.626	0.002	1.8709
1 0 -8	64.456	64.396	64.4	-0.004	1.4455
1 1 0	65.033	64.972	64.972	0.001	1.4342

Calculated lattice constants (Å)		
a_h	2.8683	+- 0.0001
c_h	14.2197	+- 0.0008

NMC532 PC washed in acid [1 h]

h k l	2θ observed (°)	2θ corrected (°)	2θ calculated (°)	Delta 2θ (°)	Calculated d-spacing (Å)
0 0 3	18.701	18.692	18.695	-0.003	4.7463
1 0 1	36.755	36.746	36.744	0.001	2.4439
0 0 6	37.892	37.883	37.881	0.003	2.3731
1 0 -2	38.403	38.395	38.394	0	2.3426
1 0 4	44.488	44.48	44.478	0.001	2.0352
1 0 -5	48.643	48.635	48.636	-0.001	1.8705
1 0 -8	64.376	64.368	64.369	-0.001	1.4461
1 1 0	65.078	65.07	65.071	-0.001	1.4322

Calculated lattice constants (Å)		
a_h	2.8645	+- 0.0001
c_h	14.2388	+- 0.0004

NMC532 PC washed in acid [4 h]

h k l	2θ observed (°)	2θ corrected (°)	2θ calculated (°)	Delta 2θ (°)	Calculated d-spacing (Å)
0 0 1	18.616	18.616	18.592	0.024	4.7686
2 0 -1	36.504	36.504	36.519	-0.015	2.4584
1 1 0	37.145	37.145	37.145	0	2.4184
0 0 2	37.707	37.707	37.696	0.01	2.3843
2 0 0	38.388	38.388	38.364	0.024	2.3443
1 1 -1	38.654	38.654	38.666	-0.012	2.3267
2 0 -2	44.042	44.042	44.039	0.003	2.0545
1 1 1	44.859	44.859	44.843	0.016	2.0195
2 0 1	48.698	48.698	48.69	0.009	1.8686
1 1 -3	64.206	64.206	64.209	-0.004	1.4493
2 0 2	64.391	64.391	64.417	-0.025	1.4452

Calculated lattice constants (Å)		
a_m	4.9819	+- 0.0008
b_m	2.8229	+- 0.
c_m	5.0669	+- 0.0006

NMC532 PC washed in acid [6 h]					
h k l	2θ observed (°)	2θ corrected (°)	2θ calculated (°)	Delta 2θ (°)	Calculated d-spacing (Å)
0 0 1	18.601	18.601	18.535	0.066	4.7831
2 0 -1	36.88	36.88	36.842	0.037	2.4376
1 1 0	37.316	37.316	37.245	0.071	2.4122
0 0 2	37.597	37.597	37.578	0.018	2.3915
1 1 -1	38.814	38.814	38.796	0.018	2.3192
2 0 -2	44.308	44.308	44.352	-0.045	2.0407
1 1 2	58.823	58.823	58.788	0.034	1.5694
2 0 2	64.196	64.196	64.307	-0.111	1.4474
3 1 -1	65.574	65.574	65.587	-0.013	1.4222

Calculated lattice constants (Å)		
a_m	4.9420	+- 0.0027
b_m	2.8184	+- 0.
c_m	5.0683	+- 0.0024

NMC532 PC washed in water

Table B.3. Agreement between measured and calculated diffraction angles used to calculate lattice constants for NMC532 PC washed in water for different durations

NMC532 PC washed in water [15 min]					
h k l	2θ observed (°)	2θ corrected (°)	2θ calculated (°)	Delta 2θ (°)	Calculated d-spacing (Å)
0 0 3	18.717	18.701	18.708	-0.007	4.743
1 0 1	36.713	36.697	36.694	0.003	2.4471
0 0 6	37.919	37.903	37.908	-0.004	2.3715
1 0 -2	38.364	38.348	38.348	0	2.3453
1 0 4	44.476	44.46	44.445	0.015	2.0367
1 0 -8	64.383	64.369	64.368	0.001	1.4462
1 1 0	64.976	64.962	64.97	-0.008	1.4342

Calculated lattice constants (Å)		
a_h	2.8684	+- 0.0003
c_h	14.2291	+- 0.0019

NMC532 PC washed in water **[30 min]**					
h k l	2θ observed (°)	2θ corrected (°)	2θ calculated (°)	Delta 2θ (°)	Calculated d-spacing (Å)
0 0 3	18.643	18.687	18.701	-0.014	4.7446
1 0 1	36.659	36.702	36.698	0.003	2.4468
0 0 6	37.863	37.905	37.894	0.011	2.3723
1 0 -2	38.313	38.356	38.351	0.004	2.3451
1 0 4	44.408	44.449	44.444	0.005	2.0367
1 0 -8	64.312	64.35	64.355	-0.005	1.4464
1 1 0	64.937	64.975	64.979	-0.004	1.434
Calculated lattice constants (Å)					
a_h	2.8680	+- 0.0003			
c_h	14.2338	+- 0.0020			

NMC532 PC washed in water **[1 h]**					
h k l	2θ observed (°)	2θ corrected (°)	2θ calculated (°)	Delta 2θ (°)	Calculated d-spacing (Å)
0 0 3	18.803	18.689	18.7	-0.01	4.7451
1 0 1	36.801	36.692	36.682	0.011	2.4479
0 0 6	37.996	37.887	37.891	-0.004	2.3725
1 0 -2	38.441	38.332	38.335	-0.003	2.3461
1 0 4	44.55	44.443	44.428	0.015	2.0374
1 0 -8	64.439	64.342	64.339	0.002	1.4467
1 1 0	65.032	64.935	64.946	-0.011	1.4347
Calculated lattice constants (Å)					
a_h	2.8694	+- 0.0003			
c_h	14.2352	+- 0.0024			

NMC532 PC washed in water **[4 h]**					
h k l	2θ observed (°)	2θ corrected (°)	2θ calculated (°)	Delta 2θ (°)	Calculated d-spacing (Å)
0 0 3	18.714	18.705	18.709	-0.004	4.7427
1 0 1	36.707	36.698	36.695	0.003	2.447
0 0 6	37.913	37.904	37.91	-0.006	2.3713
1 0 -2	38.361	38.352	38.35	0.002	2.3452
1 0 4	44.464	44.455	44.447	0.008	2.0366
1 0 -8	64.383	64.375	64.372	0.003	1.4461
1 1 0	64.973	64.965	64.972	-0.007	1.4342
Calculated lattice constants (Å)					
a_h	2.8683	+- 0.0002			
c_h	14.2281	+- 0.0014			

NMC532 PC washed in water **[6 h]**					
h k l	2θ observed (°)	2θ corrected (°)	2θ calculated (°)	Delta 2θ (°)	Calculated d-spacing (Å)
0 0 3	18.658	18.696	18.705	-0.009	4.7438
1 0 1	36.662	36.698	36.695	0.004	2.4471
0 0 6	37.869	37.905	37.901	0.003	2.3719
1 0 -2	38.313	38.349	38.348	0.001	2.3453
1 0 4	44.416	44.452	44.443	0.008	2.0367
1 0 -8	64.327	64.359	64.361	-0.002	1.4463
1 1 0	64.934	64.966	64.972	-0.005	1.4342

Calculated lattice constants (Å)		
a_h	2.8683	+- 0.0002
c_h	14.2313	+- 0.0014

NMC532 PC washed in water **[24 h]**					
h k l	2θ observed (°)	2θ corrected (°)	2θ calculated (°)	Delta 2θ (°)	Calculated d-spacing (Å)
0 0 3	18.791	18.691	18.703	-0.012	4.7442
1 0 1	36.796	36.699	36.691	0.008	2.4473
0 0 6	37.999	37.903	37.898	0.005	2.3721
1 0 -2	38.444	38.348	38.345	0.003	2.3455
1 0 4	44.538	44.444	44.439	0.005	2.0369
1 0 -8	64.439	64.353	64.354	-0.001	1.4464
1 1 0	65.044	64.958	64.965	-0.007	1.4343

Calculated lattice constants (Å)		
a_h	2.8686	+- 0.0002
c_h	14.2326	+- 0.0017

NMC532 PC washed in 0.05 M of HCl solution

Table B.4. Agreement between measured and calculated diffraction angles used to calculate lattice constants for NMC532 PC washed in acid for different durations

NMC532 PC washed in acid **[15 min]**					
h k l	2θ observed (°)	2θ corrected (°)	2θ calculated (°)	Delta 2θ (°)	Calculated d-spacing (Å)
0 0 3	18.652	18.677	18.684	-0.007	4.7489
1 0 1	36.707	36.73	36.73	0.001	2.4448
0 0 6	37.842	37.866	37.859	0.007	2.3745
1 0 -2	38.358	38.381	38.378	0.003	2.3435
1 0 4	44.437	44.46	44.457	0.003	2.0361
1 0 -5	48.587	48.61	48.612	-0.002	1.8714
1 0 -8	64.309	64.33	64.333	-0.003	1.4469
1 1 0	65.02	65.041	65.043	-0.001	1.4328

Calculated lattice constants (Å)		
a_h	2.8656	+- 0.0001
c_h	14.2468	+- 0.0010

NMC532 PC washed in acid **[30 min]**					
h k l	2θ observed (°)	2θ corrected (°)	2θ calculated (°)	Delta 2θ (°)	Calculated d-spacing (Å)
0 0 3	18.771	18.667	18.672	-0.005	4.7521
1 0 1	36.855	36.755	36.751	0.004	2.4435
0 0 6	37.937	37.837	37.832	0.005	2.3761
1 0 -2	38.497	38.398	38.397	0.001	2.3424
1 0 4	44.562	44.464	44.466	-0.002	2.0358
1 0 -5	48.708	48.613	48.615	-0.002	1.8713
1 0 -8	64.404	64.315	64.316	-0.001	1.4472
1 1 0	65.174	65.086	65.086	-0.001	1.4319

Calculated lattice constants (Å)		
a_h	2.8638	+- 0.0001
c_h	14.2564	+- 0.0008

NMC532 PC washed in acid **[1 h]**					
h k l	2θ observed (°)	2θ corrected (°)	2θ calculated (°)	Delta 2θ (°)	Calculated d-spacing (Å)
0 0 3	18.652	18.631	18.647	-0.015	4.7584
1 0 1	36.813	36.793	36.795	-0.002	2.4406
0 0 6	37.818	37.798	37.781	0.018	2.3792
1 0 -2	38.458	38.439	38.435	0.003	2.3402
1 0 4	44.502	44.483	44.485	-0.002	2.0349
1 0 -5	48.652	48.633	48.622	0.011	1.871
1 0 -8	64.288	64.27	64.284	-0.013	1.4479
1 1 0	65.195	65.177	65.177	0	1.4301

Calculated lattice constants (Å)		
a_h	2.8603	+- 0.0004
c_h	14.2752	+- 0.0026

NMC532 PC washed in acid **[4 h]**					
h k l	2θ observed (°)	2θ corrected (°)	2θ calculated (°)	Delta 2θ (°)	Calculated d-spacing (Å)
0 0 3	18.507	18.51	18.508	0.001	4.7936
1 0 1	37.024	37.027	37.021	0.005	2.4262
0 0 6	37.477	37.48	37.492	-0.012	2.3968
1 0 -2	38.627	38.63	38.63	0.001	2.3288
1 0 4	44.579	44.582	44.574	0.008	2.0311
1 0 -5	48.64	48.643	48.647	-0.004	1.8701
1 0 -8	64.098	64.101	64.092	0.009	1.4517
1 1 0	65.631	65.633	65.641	-0.008	1.4212

Calculated lattice constants (Å)		
a_h	2.8423	+- 0.0002
c_h	14.3809	+- 0.0018

NMC532 PC washed in acid [6 h]

h k l	2θ observed (°)	2θ corrected (°)	2θ calculated (°)	Delta 2θ (°)	Calculated d-spacing (Å)
0 0 3	18.56	18.459	18.466	-0.007	4.8045
1 0 1	37.181	37.084	37.082	0.001	2.4224
0 0 6	37.501	37.404	37.404	0	2.4023
1 0 -2	38.785	38.688	38.681	0.006	2.3258
1 0 4	44.692	44.597	44.595	0.002	2.0302
1 0 -5	48.744	48.651	48.648	0.003	1.8701
1 0 -8	64.116	64.029	64.029	0	1.453
1 1 0	65.847	65.761	65.767	-0.006	1.4187

Calculated lattice constants (Å)		
a_h	2.8423	+- 0.0002
c_h	14.3809	+- 0.0018

NMC532 SC washed in water

Table B.5. Agreement between measured and calculated diffraction angles used to calculate lattice constants for NMC532 SC washed in water for different durations

NMC532 SC washed in water [15 min]

h k l	2θ observed (°)	2θ corrected (°)	2θ calculated (°)	Delta 2θ (°)	Calculated d-spacing (Å)
0 0 3	18.677	18.714	18.716	-0.002	4.7409
1 0 1	36.657	36.692	36.689	0.003	2.4474
0 0 6	37.9	37.935	37.925	0.01	2.3705
1 0 -2	38.306	38.341	38.345	-0.004	2.3455
1 0 4	44.405	44.44	44.447	-0.007	2.0366
1 0 -5	48.58	48.614	48.616	-0.002	1.8712
1 0 -8	64.349	64.381	64.385	-0.004	1.4458
1 1 0	64.932	64.964	64.958	0.005	1.4344

Calculated lattice constants (Å)		
a_h	2.8689	+- 0.0002
c_h	14.2228	+- 0.0013

NMC532 SC washed in water [30 min]					
h k l	2θ observed (°)	2θ corrected (°)	2θ calculated (°)	Delta 2θ (°)	Calculated d-spacing (Å)
0 0 3	18.755	18.706	18.707	-0.002	4.7431
1 0 1	36.734	36.687	36.684	0.003	2.4478
0 0 6	37.952	37.905	37.907	-0.002	2.3716
1 0 -2	38.388	38.341	38.338	0.002	2.3459
1 0 4	44.483	44.437	44.436	0.001	2.0371
1 0 -5	48.645	48.599	48.602	-0.003	1.8717
1 0 -8	64.405	64.363	64.36	0.003	1.4463
1 1 0	64.988	64.946	64.95	-0.003	1.4346

Calculated lattice constants (Å)		
a_h	2.8692	+- 0.0001
c_h	14.2293	+- 0.0007

NMC532 SC washed in water [1 h]					
h k l	2θ observed (°)	2θ corrected (°)	2θ calculated (°)	Delta 2θ (°)	Calculated d-spacing (Å)
0 0 3	18.733	18.718	18.716	0.001	4.7409
1 0 1	36.704	36.689	36.69	0	2.4474
0 0 6	37.947	37.933	37.926	0.007	2.3704
1 0 -2	38.357	38.343	38.346	-0.003	2.3454
1 0 4	44.457	44.443	44.448	-0.005	2.0365
1 0 -5	48.627	48.613	48.617	-0.004	1.8712
1 0 -8	64.397	64.384	64.386	-0.003	1.4458
1 1 0	64.979	64.967	64.96	0.006	1.4344

Calculated lattice constants (Å)		
a_h	2.8688	+- 0.0001
c_h	14.2226	+- 0.0011

NMC532 SC washed in water [4 h]					
h k l	2θ observed (°)	2θ corrected (°)	2θ calculated (°)	Delta 2θ (°)	Calculated d-spacing (Å)
0 0 3	18.69	18.704	18.711	-0.007	4.7422
1 0 1	36.682	36.696	36.688	0.008	2.4475
0 0 6	37.908	37.922	37.914	0.008	2.3711
1 0 -2	38.327	38.341	38.343	-0.002	2.3456
1 0 4	44.427	44.44	44.442	-0.002	2.0368
1 0 -5	48.593	48.606	48.609	-0.004	1.8715
1 0 -8	64.358	64.37	64.372	-0.002	1.4461
1 1 0	64.945	64.957	64.958	0	1.4344

Calculated lattice constants (Å)		
a_h	2.8689	+- 0.0002
c_h	14.2267	+- 0.0012

NMC532 SC washed in water **[6 h]**					
h k l	2θ observed (°)	2θ corrected (°)	2θ calculated (°)	Delta 2θ (°)	Calculated d-spacing (Å)
0 0 3	18.793	18.717	18.713	0.004	4.7417
1 0 1	36.752	36.678	36.684	-0.006	2.4478
0 0 6	37.999	37.926	37.919	0.007	2.3708
1 0 -2	38.409	38.336	38.339	-0.003	2.3458
1 0 4	44.509	44.438	44.441	-0.003	2.0369
1 0 -5	48.675	48.604	48.609	-0.004	1.8715
1 0 -8	64.436	64.37	64.375	-0.004	1.446
1 1 0	65.023	64.958	64.949	0.009	1.4346
Calculated lattice constants (Å)					
a_h	2.8692	+- 0.0002			
c_h	14.2250	+- 0.0013			
NMC532 SC washed in water **[24 h]**					
h k l	2θ observed (°)	2θ corrected (°)	2θ calculated (°)	Delta 2θ (°)	Calculated d-spacing (Å)
0 0 3	18.655	18.705	18.708	-0.003	4.743
1 0 1	36.652	36.7	36.695	0.006	2.4471
0 0 6	37.857	37.905	37.908	-0.003	2.3715
1 0 -2	38.306	38.354	38.349	0.005	2.3452
1 0 4	44.401	44.448	44.446	0.002	2.0366
1 0 -5	48.558	48.604	48.612	-0.007	1.8714
1 0 -8	64.332	64.375	64.369	0.006	1.4461
1 1 0	64.923	64.966	64.971	-0.005	1.4342
Calculated lattice constants (Å)					
a_h	2.8684	+- 0.0002			
c_h	14.2289	+- 0.0012			

NMC532 SC washed in 0.05 M of HCl solution

Table B.6. Agreement between measured and calculated diffraction angles used to calculate lattice constants for NMC532 SC washed in acid for different durations

NMC532 SC washed in acid [15 min]					
h k l	2θ observed (°)	2θ corrected (°)	2θ calculated (°)	Delta 2θ (°)	Calculated d-spacing (Å)
0 0 3	18.707	18.705	18.712	-0.007	4.742
1 0 1	36.695	36.693	36.692	0.001	2.4472
0 0 6	37.93	37.928	37.916	0.012	2.371
1 0 -2	38.344	38.342	38.347	-0.005	2.3453
1 0 4	44.453	44.451	44.447	0.004	2.0366
1 0 -5	48.614	48.612	48.614	-0.001	1.8713
1 0 -8	64.371	64.369	64.376	-0.008	1.446
1 1 0	64.971	64.969	64.966	0.003	1.4343
Calculated lattice constants (Å)					
a_h	2.8686	+- 0.0002			
c_h	14.2261	+- 0.0015			
NMC532 SC washed in acid [30 min]					
h k l	2θ observed (°)	2θ corrected (°)	2θ calculated (°)	Delta 2θ (°)	Calculated d-spacing (Å)
0 0 3	18.802	18.699	18.702	-0.003	4.7444
1 0 1	36.79	36.692	36.689	0.003	2.4474
0 0 6	37.999	37.901	37.896	0.005	2.3722
1 0 -2	38.444	38.346	38.342	0.003	2.3456
1 0 4	44.531	44.434	44.437	-0.002	2.037
1 0 -5	48.688	48.593	48.6	-0.007	1.8718
1 0 -8	64.44	64.352	64.351	0.001	1.4465
1 1 0	65.049	64.961	64.96	0.001	1.4344
Calculated lattice constants (Å)					
a_h	2.8688	+- 0.0001			
c_h	14.2332	+- 0.0009			

NMC532 SC washed in acid [1 h]

h k l	2θ observed (°)	2θ corrected (°)	2θ calculated (°)	Delta 2θ (°)	Calculated d-spacing (Å)
0 0 3	18.746	18.698	18.702	-0.004	4.7445
1 0 1	36.739	36.692	36.695	-0.003	2.4471
0 0 6	37.947	37.901	37.895	0.006	2.3723
1 0 -2	38.401	38.354	38.348	0.006	2.3453
1 0 4	44.483	44.438	44.441	-0.003	2.0368
1 0 -5	48.649	48.604	48.604	0	1.8717
1 0 -8	64.392	64.351	64.353	-0.003	1.4464
1 1 0	65.014	64.973	64.972	0.001	1.4342

Calculated lattice constants (Å)

a_h	2.8683	+- 0.0001
c_h	14.2336	+- 0.0010

NMC532 SC washed in acid [4 h]

h k l	2θ observed (°)	2θ corrected (°)	2θ calculated (°)	Delta 2θ (°)	Calculated d-spacing (Å)
0 0 3	18.686	18.65	18.657	-0.007	4.7557
1 0 1	36.803	36.769	36.767	0.002	2.4424
0 0 6	37.848	37.814	37.803	0.012	2.3779
1 0 -2	38.448	38.414	38.41	0.004	2.3416
1 0 4	44.5	44.467	44.469	-0.002	2.0356
1 0 -5	48.636	48.603	48.612	-0.008	1.8714
1 0 -8	64.319	64.289	64.291	-0.003	1.4477
1 1 0	65.152	65.122	65.12	0.002	1.4313

Calculated lattice constants (Å)

a_h	2.8625	+- 0.0002
c_h	14.2671	+- 0.0015

NMC532 SC washed in acid [6 h]

h k l	2θ observed (°)	2θ corrected (°)	2θ calculated (°)	Delta 2θ (°)	Calculated d-spacing (Å)
0 0 3	18.573	18.475	18.481	-0.005	4.8008
1 0 1	37.149	37.055	37.053	0.002	2.4242
0 0 6	37.542	37.448	37.434	0.013	2.4004
1 0 -2	38.742	38.648	38.655	-0.007	2.3273
1 0 4	44.673	44.581	44.58	0.001	2.0308
1 0 -5	48.731	48.64	48.641	0	1.8704
1 0 -8	64.12	64.036	64.045	-0.008	1.4527
1 1 0	65.795	65.712	65.707	0.005	1.4199

Calculated lattice constants (Å)

a_h	2.8398	+- 0.0002
c_h	14.4024	+- 0.0017

Appendix C. Permission

ELSEVIER LICENSE
TERMS AND CONDITIONS

Jul 29, 2020

This Agreement between Ines Hamam ("You") and Elsevier ("Elsevier") consists of your license details and the terms and conditions provided by Elsevier and Copyright Clearance Center.

License Number	4878491304092
License date	Jul 29, 2020
Licensed Content Publisher	Elsevier
Licensed Content Publication	Journal of Power Sources
Licensed Content Title	Capacity fading of LiAl y Ni1−x−y Co x O2 cathode for lithium-ion batteries during accelerated calendar and cycle life tests (effect of depth of discharge in charge–discharge cycling on the suppression of the micro-crack generation of LiAl y Ni1−x−y Co x O2 particle)
Licensed Content Author	Shoichiro Watanabe,Masahiro Kinoshita,Takashi Hosokawa,Kenichi Morigaki,Kensuke Nakura
Licensed Content Date	Aug 15, 2014
Licensed Content Volume	260
Licensed Content Issue	n/a
Licensed Content Pages	7
Start Page	50
End Page	56
Type of Use	reuse in a thesis/dissertation
Portion	figures/tables/illustrations
Number of figures/tables/illustrations	3
Format	both print and electronic
Are you the author of this Elsevier article?	No
Will you be translating?	No
Title	Study of the surface reactivity of Ni-rich positive electrode materials for Li-ion cells
Institution name	Dalhousie University
Expected presentation date	Aug 2020
Portions	Fig. 1, Fig. 4, Fig. 5
Requestor Location	Ines Hamam 348 Glencairn Dr. Moncton, NB E1G 1Y4 Canada Attn: Ines Hamam
Publisher Tax ID	GB 494 6272 12

REFERENCES

1. World Meteorological Organization, *WMO statement on the status of the global climate in 2019*, Geneva, Switzerland (2020).at <http://www.wmo.int/pages/mediacentre/press_releases/documents/WMO_1108_EN_web_000.pdf>

2. IPCC, *Global warming of 1.5 ° C*, (2019).at <www.environmentalgraphiti.org>

3. D. Larcher and J. M. Tarascon, *Nat. Chem.* 7, 19 (2015).

4. International Energy Agency, *World Energy Outlook 2018*, (2018).doi:10.1787/weo-2018-2-en

5. A. Opitz, P. Badami, L. Shen, K. Vignarooban, and A. M. Kannan, *Study energy storage Syst. Environ. challenges Batter.* 69, 192 (2019).

6. J.-M. Tarascon and M. Armand, *Nature* 414, 359 (2001).

7. N. Nitta, F. Wu, J. T. Lee, and G. Yushin, *Mater. Today* 18, 252 (2015).

8. D. R. Lide, *Handbook of Chemistry and Physics*, (2003).doi:10.1136/oem.53.7.504

9. G. E. Blomgren, *J. Electrochem. Soc.* 164, A5019 (2017).

10. Vehicle Warrantyat <https://www.tesla.com/en_CA/support/vehicle-warranty>

11. J. E. Harlow, X. Ma, J. Li, E. Logan, Y. Liu, N. Zhang, L. Ma, S. L. Glazier, M. M. E. Cormier, M. Genovese, S. Buteau, A. Cameron, J. E. Stark, and J. R. Dahn, *J. Electrochem. Soc.* 166, A3031 (2019).

12. M. S. Whittingham, *Chem. Rev.* 104, 4271 (2004).

13. J. R. Dahn and G. M. Ehrlich, Linden's Handbook of Batteries, Fifth Edition, Edited by K. W. Beard, McGraw-Hill, pp. 755–825.

14. C. J. Weber, S. Geiger, S. Falusi, and M. Roth, *AIP Conf. Proc.* 1597, 66 (2014).

15. J. B. Goodenough and K. S. Park, *J. Am. Chem. Soc.* 135, 1167 (2013).

16. W. Choi, H. C. Shin, J. M. Kim, J. Y. Choi, and W. S. Yoon, *J. Electrochem. Sci. Technol.* 11, 1 (2020).

17. J. Betz, G. Bieker, P. Meister, T. Placke, M. Winter, and R. Schmuch, *Adv. Energy Mater.* 9, 1 (2019).

18. P. He, H. Yu, D. Li, and H. Zhou, *J. Mater. Chem.* 22, 3680 (2012).

19. K. Zaghib, A. Mauger, J. B. Goodenough, and C. M. Julien, Design and Properties of LiFePO4 Nano-materials for High-Power Applications, in *Nanotechnology for Lithium-Ion Batteries*, Edited by Y. Abu-Lebdeh and I. Davidson, Boston, MA, Springer US (2013), pp. 179–220.doi:10.1007/978-1-4614-4605-7_8

20. A. Manthiram, *Nat. Commun.* 11, 1 (2020).

21. Commodity and Metal Pricesat <http://www.infomine.com/investment/metal-prices/>

22. B. K. Sovacool, *Extr. Ind. Soc.* 6, 915 (2019).

23. C. Banza Lubaba Nkulu, L. Casas, V. Haufroid, T. De Putter, N. D. Saenen, T. Kayembe-Kitenge, P. Musa Obadia, D. Kyanika Wa Mukoma, J. M. Lunda Ilunga, T. S. Nawrot, O. Luboya Numbi, E. Smolders, and B. Nemery, *Nat. Sustain.* 1, 495 (2018).

24. G. Berckmans, M. Messagie, J. Smekens, N. Omar, L. Vanhaverbeke, and J. Van Mierlo, *Energies* 10 (2017).

25. Ni

26. H. Li, A. Liu, N. Zhang, Y. Wang, S. Yin, H. Wu, and J. R. Dahn, *Chem. Mater.* 31, 7574 (2019).

27. J. H. Kim, S. J. Kim, T. Yuk, J. Kim, C. S. Yoon, and Y. K. Sun, *ACS Energy Lett.* 3, 3002 (2018).

28. B. Y. R. D. Shannon, M. H, N. H. Baur, O. H. Gibbs, M. Eu, and V. Cu, (1976).

29. G. Sun, X. Yin, W. Yang, A. Song, C. Jia, W. Yang, Q. Du, Z. Ma, and G. Shao, *Phys. Chem. Chem. Phys.* 19, 29886 (2017).

30. M. Bianchini, M. Roca-Ayats, P. Hartmann, T. Brezesinski, and J. Janek, *Angew. Chemie - Int. Ed.* 58, 10434 (2019).

31. W. Li, H. Y. Asl, Q. Xie, and A. Manthiram, *J. Am. Chem. Soc.* 141, 5097 (2019).

32. S. Hwang, W. Chang, S. M. Kim, D. Su, D. H. Kim, J. Y. Lee, K. Y. Chung, and E. A. Stach, *Chem. Mater.* 26, 1084 (2014).

33. Z. Jiang, H. Gu, J. Zhang, C. Cao, X. Xie, K. Wang, and B. Xia, *Ionics (Kiel).* (2020).doi:10.1007/s11581-020-03646-x

34. M. Guilmard, L. Croguennec, and C. Delmas, *Chem. Mater.* 15, 4484 (2003).

35. L. Wu, K. W. Nam, X. Wang, Y. Zhou, J. C. Zheng, X. Q. Yang, and Y. Zhu, *Chem. Mater.* 23, 3953 (2011).

36. H. Arai, S. Okada, Y. Sakurai, and J. I. Yamaki, *Solid State Ionics* 109, 295 (1998).

37. A. Rougier, I. Saadoune, P. Gravereau, P. Willmann, and C. Delmas, *Solid State Ionics* 90, 83 (1996).

38. H. Li, M. Cormier, N. Zhang, J. Inglis, J. Li, and J. R. Dahn, *J. Electrochem. Soc.* 166, A429 (2019).

39. D. D. MacNeil, Z. Lu, Z. Chen, and J. R. Dahn, *J. Power Sources* 108, 8 (2002).

40. T. Ohzuku, A. Ueda, and M. Kouguchi, *Dimens. Contemp. Ger. Arts Lett.* 142, 4033 (1995).

41. W. Li, J. R. Dahn, and J. H. Root, *Mater. Res. Soc. Symp. - Proc.* 369, 69 (1995).

42. J. N. Reimers and J. R. Dahn, *J. Electrochem. Soc.* 139, 2091 (1992).

43. J. R. Dahn, U. von Sacken, M. W. Juzkow, and H. Al-Janaby, *J. Electrochem. Soc.* 138, 2207 (1991).

44. K. Matsumoto, R. Kuzuo, K. Takeya, and A. Yamanaka, *J. Power Sources* 81–82, 558 (1999).

45. N. V. Faenza, L. Bruce, Z. W. Lebens-Higgins, I. Plitz, N. Pereira, L. F. J. Piper, and G. G. Amatucci, *J. Electrochem. Soc.* 164, A3727 (2017).

46. K. Shizuka, C. Kiyohara, K. Shima, and Y. Takeda, *J. Power Sources* 166, 233 (2007).

47. D. P. Abraham, R. D. Twesten, M. Balasubramanian, I. Petrov, J. McBreen, and K. Amine, *Electrochem. commun.* 4, 620 (2002).

48. D. P. Abraham, R. D. Twesten, M. Balasubramanian, J. Kropf, D. Fischer, J. McBreen, I. Petrov, and K. Amine, *J. Electrochem. Soc.* 150, A1450 (2003).

49. H. S. Liu, Z. R. Zhang, Z. L. Gong, and Y. Yang, *Electrochem. Solid-State Lett.* 7 (2004).

50. H. Liu, Y. Yang, and J. Zhang, *J. Power Sources* 162, 644 (2006).

51. R. Robert, C. Bunzli, E. J. Berg, and P. Novák, *Chem. Mater.* 27, 526 (2015).

52. S. E. Renfrew and B. D. McCloskey, *J. Am. Chem. Soc.* 139, 17853 (2017).

53. N. Mahne, S. E. Renfrew, B. D. McCloskey, and S. A. Freunberger, *Angew. Chemie - Int. Ed.* 57, 5529 (2018).

54. H. J. Noh, S. Youn, C. S. Yoon, and Y. K. Sun, *J. Power Sources* 233, 121 (2013).

55. J. H. Jo, C. H. Jo, H. Yashiro, S. J. Kim, and S. T. Myung, *J. Power Sources* 313, 1 (2016).

56. D. Pritzl, T. Teufl, A. T. S. Freiberg, B. Strehle, J. Sicklinger, H. Sommer, P. Hartmann, and H. A. Gasteiger, *J. Electrochem. Soc.* 166, 4056 (2019).

57. J. Yokoyama, Y. Furuichi, T. Nakayama, T. Komukai, K. Mori, and M. Yamauchi, Positive Electrode Active Material for Non-Aqueous Electrolyte Secondary Battery and Method for Producing Same, and Non-Aqueous Electrolyte Secondary Battery Manufactured Using Said Positive Electrode Active Material, US 2017/0054147 A1 (2017).

58. J. A. Dean, *Lange's Handbook Of Chemistry, 15th ed.*, (1999).

59. Z. F. Yow, Y. L. Oh, W. Gu, R. P. Rao, and S. Adams, *Solid State Ionics* 292, 122 (2016).

60. I. A. Shkrob, J. A. Gilbert, P. J. Phillips, R. Klie, R. T. Haasch, J. Bareño, and D. P. Abraham, *J. Electrochem. Soc.* 164, A1489 (2017).

61. X. Zheng, X. Li, Z. Wang, H. Guo, Z. Huang, G. Yan, and D. Wang, *Electrochim. Acta* 191, 832 (2016).

62. B. C. Park, H. J. Bang, K. Amine, E. Jung, and Y. K. Sun, *J. Power Sources* 174, 658 (2007).

63. P. Hou, H. Zhang, Z. Zi, L. Zhang, and X. Xu, *J. Mater. Chem. A* 5, 4254 (2017).

64. Y. K. Sun, S. T. Myung, B. C. Park, and K. Amine, *Chem. Mater.* 18, 5159 (2006).

65. M. N. Obrovac and V. L. Chevrier, *Chem. Rev.* 114, 11444 (2014).

66. M. T. McDowell, S. W. Lee, W. D. Nix, and Y. Cui, *Adv. Mater.* 25, 4966 (2013).

67.   L. Y. Beaulieu, K. W. Eberman, R. L. Turner, L. J. Krause, and J. R. Dahna, *Electrochem. Solid-State Lett.* 4, 7 (2001).

68.   K. Xu, *Chem. Rev.* 104, 4303 (2004).

69.   J. Li, H. Li, X. Ma, W. Stone, S. Glazier, E. Logan, E. M. Tonita, K. L. Gering, and J. R. Dahn, *J. Electrochem. Soc.* 165, A1027 (2018).

70.   E. R. Logan, D. S. Hall, M. M. E. Cormier, T. Taskovic, M. Bauer, I. Hamam, H. Hebecker, L. Molino, and J. R. Dahn, *J. Phys. Chem. C* 124, 12269 (2020).

71.   M. Moshkovich, M. Cojocaru, H. E. Gottlieb, and D. Aurbach, *J. Electroanal. Chem.* 497, 84 (2001).

72.   M. Stich, M. Göttlinger, M. Kurniawan, U. Schmidt, and A. Bund, *J. Phys. Chem. C* 122, 8836 (2018).

73.   Y. Bi, T. Wang, M. Liu, R. Du, W. Yang, Z. Liu, Z. Peng, Y. Liu, D. Wang, and X. Sun, *RSC Adv.* 6, 19233 (2016).

74.   W. Li, *J. Electrochem. Soc.* 167, 090514 (2020).

75.   D. Aurbach, B. Markovsky, A. Rodkin, E. Levi, Y. S. Cohen, H. J. Kim, and M. Schmidt, *Electrochim. Acta* 47, 4291 (2002).

76.   W. Li, B. Song, and A. Manthiram, *Chem. Soc. Rev.* 46, 3006 (2017).

77.   S. Yamada, M. Fujiwara, and M. Kanda, *J. Power Sources* 54, 209 (1995).

78.   J. C. Hunter, *J. Solid State Chem.* 39, 142 (1981).

79.   F. Schipper, E. M. Erickson, C. Erk, J.-Y. Shin, F. F. Chesneau, and D. Aurbach, *J. Electrochem. Soc.* 164, A6220 (2017).

80.   H. Li, N. Zhang, J. Li, and J. R. Dahn, *J. Electrochem. Soc.* 165, A2985 (2018).

81.   R. Weber, C. R. Fell, J. R. Dahn, and S. Hy, *J. Electrochem. Soc.* 164, A2992 (2017).

82.   J. Sicklinger, M. Metzger, H. Beyer, D. Pritzl, and H. A. Gasteiger, *J. Electrochem. Soc.* 166, A2322 (2019).

83.   M. Cuisinier, J. F. Martin, N. Dupré, R. Kanno, and D. Guyomard, *J. Mater. Chem.* 21, 18575 (2011).

84.   L. X. Yuan, Z. H. Wang, W. X. Zhang, X. L. Hu, J. T. Chen, Y. H. Huang, and J. B. Goodenough, *Energy Environ. Sci.* 4, 269 (2011).

85. J. L. Shi, R. Qi, X. D. Zhang, P. F. Wang, W. G. Fu, Y. X. Yin, J. Xu, L. J. Wan, and Y. G. Guo, *ACS Appl. Mater. Interfaces* 9, 42829 (2017).

86. C. Geng, A. Liu, and J. R. Dahn, *J. Electrochem. Soc.* 0 (2020).doi:10.1021/acs.chemmater.0c01728

87. S. Watanabe, M. Kinoshita, T. Hosokawa, K. Morigaki, and K. Nakura, *J. Power Sources* 260, 50 (2014).